Selective Nanoporous Sorbents for Gas Based Separations: Ion Exchanged Silicoaluminophosphates and Titanosilicates

by

Milton E. Rivera-Ramos

A thesis submitted in partial fulfillment of the requirements for the degree of

DOCTOR OF PHILOSOPHY
in
CHEMICAL ENGINEERING

UNIVERSITY OF PUERTO RICO
MAYAGÜEZ CAMPUS
2009

Approved by:

_____	_____
Arturo J. Hernández-Maldonado, PhD President, Graduate Committee	Date
_____	_____
Carlos Rinaldi, PhD Member, Graduate Committee	Date
_____	_____
Jaime Benítez, PhD Member, Graduate Committee	Date
_____	_____
David Suleiman, PhD Member, Graduate Committee	Date
_____	_____
Gustavo López, PhD Representative of Graduate Studies	Date
_____	_____
David Suleiman, PhD Chairperson of the Department	Date

Selective Nanoporous Sorbents for Gas Based Separations: Ion Exchanged Silicoaluminophosphates and Titanosilicates

by: Milton E. Rivera-Ramos
Submitted to the Department of Chemical Engineering
on May 5, 2009, in partial fulfillment of the
requirements for the degree of
Doctor of Philosophy

Abstract

Two specific sorbents were targeted in this research work: silicoaluminosphosphates (SAPOs) and titanium silicates. For the former, Na^{+}-SAPO-34 sorbents were ion-exchanged with several cations (Ag^{+}, Mg^{2+}, Ca^{2+}, Sr^{2+}, Ti^{3+}, and Ce^{3+}) to study their effect on the adsorption of similar size light gases. Adsorption isotherms for the functionalized M^{n+}-SAPO-34 materials displayed a non-linear behavior and, in many cases, did not follow the typical pore-filling mechanism. The surface interactions were analyzed according to electrostatic and non-specific contributions. Divalent cations were found to interact more with the sorbate when compared to the other charged species. Due to strong ion-quadrupole interactions, all the sorbent materials exhibited higher affinity for CO_2 over the other gases tested (i.e., CH_4, H_2, N_2 and O_2). Mathematical modeling to estimate binary component adsorption performance during Vacuum Pressure Swing Adsorption (VPSA) corroborated that Sr^{2+}-SAPO-34 sorbents are a suitable option for CO_2 removal from CH_4 mixtures, especially at low concentrations. In addition, these materials were subject of a diffusive transport study to elucidate the effect of particle size distribution on the estimates of diffusion time constants. A gamma particle size distribution was found to suitably describe the SAPO-34 characteristic dimensions.

Many soft titanium silicates display sorption selectivity towards specific gases based on size exclusion principles. However, selectivity comes at the expense of sorption ultimate capacity, which decreases considerably due to the lack of pore volume. Here we present a novel titanium silicate polymorph (named UPRM-4d), which was synthesized by means of a structure-directing agent (SDA) to increase the working pore volume, and still exhibits the structural flexibility of Zorite based titanium silicates. The SDA was successfully removed from the as-synthesized sample by ion-exchange techniques to expose the pore volume. Afterwards, the UPRM-4d sorbent displayed selectivity towards CO_2 and adsorbed almost twice the amount when compared to a commercial sorbent titanium silicate material known as ETS-4. Other UPRM-4 variants were studied as well, and their synthesis and characterization are presented here.

Thesis Supervisor: Dr. Arturo J. Hernández-Maldonado

Solventes Nanoporosos Selectivos para Separaciones Gaseosas: Silicoaluminofosfatos Intercambiados Iónicamente y Titanosilicatos

por: Milton E. Rivera-Ramos
Sometida al Departamento de Ingeniería Química
el 5 de mayo de 2009, en cumplimiento parcial de los
requerimientos para el grado de
Doctor en Filosofía

Resumen

Dos tipos de sorbentes fueron estudiados en este trabajo investigativo: silicoaluminosfosfatos (SAPOs) y titanosilicatos. El primero de ellos, Na^{+}-SAPO-34 fue intercambiado iónicamente con varios cationes (Ag^{+}, Mg^{2+}, Ca^{2+}, Sr^{2+}, Ti^{3+}, y Ce^{3+}) para estudiar el efecto en la adsorción de gases de tamaños similares. Isotermas de adsorción para los materiales funcionalizados M^{n+}-SAPO-34 muestran un comportamiento no-lineal y en muchos casos no siguen le mecanismo típico de llenado de poro. Las interacciones de la superficie fueron analizadas de acuerdo a las contribuciones electroestáticas y las no-específicas. Se encontró que los cationes divalentes interaccionan más fuerte con los sorbatos en comparación con las otras especies estudiadas. Debido a la fuerte interacción de quadrupolo, todos los sorbentes exhibieron mayor afinidad para CO_2 sobre los otros gases (i.e., CH_4, H_2, N_2 y O_2). Modelamiento matemático para estudiar el comportamiento de una mezcla binaria durante un proceso de adsorción con regeneración al vacío demostró que Sr^{2+}-SAPO-34 es por mucho el mejor sorbente para la remoción de CO_2 de una mezcla con CH_4, especialmente a bajas concentraciones. En adición, estos materiales fueron sometidos al estudio del transporte difusivo para determinar el efecto de la distribución de tamaño de partícula en la estimación de las constantes de tiempo de difusión. Se encontró que una distribución de tamaño de partícula gamma es la que mejor describe las características dimensionales de SAPO-34.

Diferentes titanosilicatos presentan selectividad de adsorción hacia gases específicos basados en el principio de exclusión de tamaño. Sin embargo, esta selectividad afecta la capacidad de adsorción, ya que la misma decrece debido a la falta de volumen de poro. En este trabajo se presenta un novedoso titanosilicato polimorfo (nombrado como UPRM-4d), el cual fue sintetizado utilizando un agente director de estructura para aumentar el volumen de poro disponible, manteniendo la flexibilidad estructural del titanosilicato Zorita. El agente director fue removido exitosamente del material según sintetizado por técnicas de intercambio iónico para exponer el volumen de poro. Luego del tratamiento, UPRM-4d presentó selectividad hacia CO_2 y adsorbió casi el doble comparado con el sorbente comercial conocido como ETS-4. Otras variantes de UPRM-4 fueron también estudiadas.

Consejero de Tésis: Dr. Arturo J. Hernández-Maldonado

Este trabajo es dedicado a mi esposa y a mis hijos,

Eunice Mercado Feliciano,

Adrián E. Rivera Mercado

y

a mi bebe

Por siempre apoyarme en todas mis decisiones, por confiar en mí y por darme todo su amor y cariño. Espero nunca defraudarlos y poder darles lo que por estos pasados años no he podido. Fue un camino largo pero yo se que con la ayuda del Señor podremos continuar hacia una nueva etapa de nuestras vidas.

Los amo de aquí al infinito y más allá…

Acknowledgements

I wish to sincerely acknowledge my advisor Dr. Arturo J. Hernández because this investigation would not have been the same without his direction and scientific vision. I want to express gratitude as well for the support that I received from Dr. Carlos Rinaldi during the discussions regarding diffusion and transport models.

During the development of my graduate studies many other persons collaborated directly and indirectly with my research. Without their support it would have been difficult for me to finish my work. I want to particularly thank my first lab partner and friend in INQU, Daphne S. Belén, who gave me all her cooperation during the first years of my PhD studies. Also I want to say thanks to my dear friend, Sindia Rivera, for the motivation and support during a critical stage in my investigation. I am also very grateful for all the pleasant moments that I shared with my NSSAL lab mates and INQU friends. I wish to acknowledge the help of my REU students, Kendall Williamson and Mark Michelman, during the titanium silicates related experiments and the help received from Mr. Angel Zapata, who assisted with the equipment and utilities setup.

In addition, I would like to show gratitude to Dr. María Martínez Research Group for kindly providing access to the hydrogen adsorption isotherms. Dr. Brian Toby from the Advanced Photon Source at the Argonne National Laboratory is also acknowledged for performing the Synchrotron testing. Finally, I want to express grateful to Dr. Rigiang Fu from the National High Magnetic Field Laboratory for performing the NMR analyses.

The initial stage of this work was supported by the National Science Foundation/ Puerto Rico EPSCoR Program (grant EPS-0223152). I also wish to acknowledge the financial support from the UPRM Chemical Engineering Department, the Puerto Rico EPSCoR Institute for Functional Nanomaterials, the NASA Puerto Rico Space Grant Consortium and the NSF UPRM CREST program (grant HRD-0833112). Support from the Sloan Foundation is also gratefully acknowledged.

Contents

List of Figures

List of Tables

Chapter 1

Introduction

1.1 Nanoporous Zeolitic Materials

About 40 naturally occurring zeolites have been identified during the past 200 years. The most common are Analcime, Chabazite, Clinoptilolite, Erionite, Ferrierite, Heulandite, Laumontite, Mordenite, and Phillipsite. To date, more than 150 zeolites have been synthesized; the most common are zeolites type -A, -X, -Y, and ZMS-5. Natural and synthetic zeolites are used commercially because of their unique adsorption, ion-exchange, molecular sieve, and catalytic properties.[1] This family of nanoporous materials contributes to a cleaner, safer environment in a great number of ways. Their applications have been motivated by environmental concerns where they perform a significant role in reducing toxic waste and energy consumption.

There is great interest today in the development of zeolitic nanoporous materials with specific framework topologies based on templated hydrothermal paths to reach specific adsorption characteristics.[2-6] The possibility of adsorbing certain molecules while excluding others has opened up a wide range of molecular sieving applications (Figure 1-1). Sometimes it is simply a matter of the size and shape of pores controlling access into the material porous framework.[7] In other cases, different types of molecules enter the material, but some diffuse through the channels faster than others. This is ideal for

adsorption applications such as separation of mixtures of molecules with similar kinetic sizes. Traditional examples would be the nitrogen/methane (N_2/CH_4) and carbon dioxide/ methane (CO_2/CH_4) pair mixtures. A methane molecule (σ = 3.8Å) is larger than a carbon dioxide molecule by 0.5Å, and only 0.16Å larger when compared with nitrogen. Due to the difficulty level of separations such as these one, it is imperative to completely understand the equilibrium and kinetic effects showcased by the nanoporous sorbent before and after functionalization. These include specific (i.e. dispersion) and non-specific (i.e. dipole moment) surface interactions and framework topology, just to mention a few.

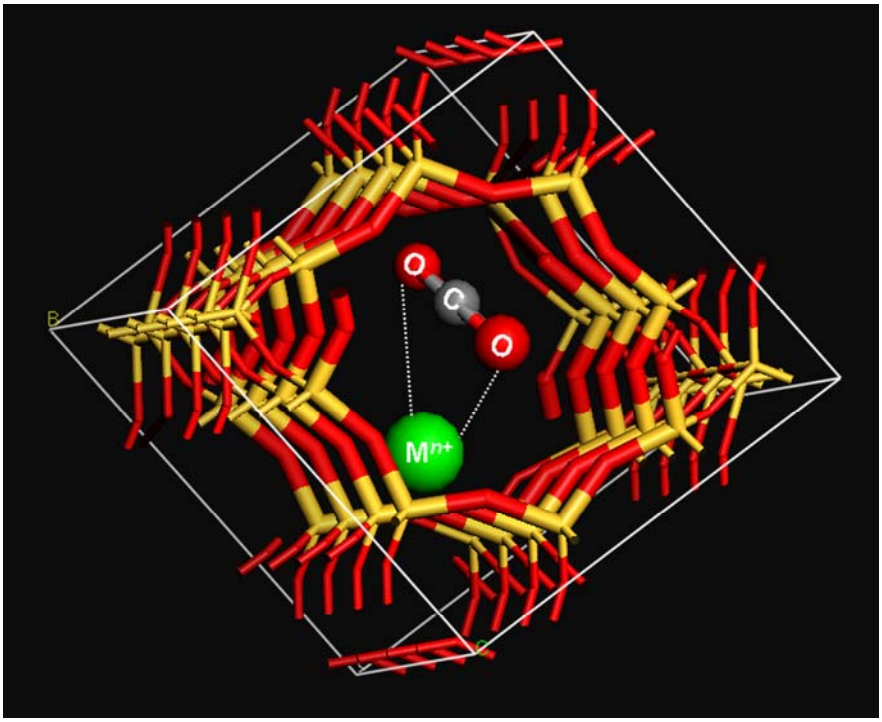

Figure 1-1. Schematic representation of the adsorption of CO_2 on the surface of M^{n+}-SAPO-34 pore channels.

1.2 Background and Motivation

A number of nanoporous materials have already shown potential for gas separation due to their small pore sizes and their narrow pore-size distribution.[8] As shown in the literature, many studies have tried to address the N_2/CH_4 separation problem by using porous materials, such as 4A zeolite and carbon molecular sieves (CMS). A process using 4A was developed by Habgood (1958), but it was limited to low temperatures (194 to 273 K) and high methane feed content (≥ 90% methane).[9] Ackley and Yang (1990) used CMS adsorbents for separation of N_2/CH_4 mixtures by pressure swing adsorption processes. However, they concluded that the potential for CMS to achieve a desired pipeline quality (90% methane) was also limited.[10]

Zeolite Clinoptilolite was also considered for this separation. The adsorption characteristics of Clinoptilolite in the unmodified and ion-exchanged form have been thoroughly investigated.[11] Frankiewicz and Donnelly (1983) studied calcium-exchanged Clinoptilolites for N_2/CH_4 separation, but the resulting product was also below pipeline quality.[12] Equilibrium isotherms for N_2 on various ion-exchanged Clinoptilolite were also reported by Ackley and Yang (1991).[13] Jayaraman et al. (2004) found that the capacity of purified Clinoptilolite for nitrogen adsorption is almost doubled at 5 atm[14] while mixed-exchange Clinoptilolites showed a wide range of adsorption characteristics.[15]

Another porous material tested for separation of light gases, including natural gas, was a soft titanium silicate known as ETS-4. During the last decade many groups have studied this Zorite-like titanosilicate molecular sieve, which has adjustable pores for size-

selective adsorption of small molecules.[16-19] For example, the effective pore size of strontium exchanged ETS-4 decreases as the dehydration temperature is increased, allowing this material to be used for the separation of mixtures of molecules with similar sizes in the 4.0 to 3.0 Å range such as N_2/CH_4, Ar/O_2, and N_2/O_2 pairs. The observed equilibrium adsorption uptake, however, indicates that the material has low capacity even at pressures around 1 atm (~0.30 mmol/g for N_2).[14, 16] This is due to the absence of cages in ETS-4 materials, which would significantly increase pore volume and, therefore, sorption capacity. To include such framework volume characteristics while preserving small pore dimensions, it is often necessary to employ templated synthesis routes. Such is the case of many novel zeolitic formulations.[20, 21]

1.3 Overview of the Thesis

The principal objective of this work is the development of selective nanoporous sorbents for gas based separation. Two different strategies were defined, the first one being the modification of a zeolitic framework, the silicoaluminophosphate SAPO-34, and the second one consisting in the bottom-up synthesis of new titanium silicate materials based on a known Zorite-like variant.

Chapter 2 presents the development of ion-exchanged M^{n+}-SAPO-34 materials for similar-size molecular pair adsorption (N_2/CH_4) at temperatures and pressures that approach ambient conditions. We have exchanged the extraframework cations of Na^+-SAPO-34 with monovalent, divalent, and trivalent cations in order to understand the effect of these species in the adsorption capacity of nitrogen and methane. This part of the

work was published by our research group in the Industrial and Engineering Chemical Research Journal in 2007.[22]

Chapter 3 focuses on the study of ion-exchanged M^{n+}-SAPO-34 materials for the adsorption of CO_2. The results are compared with adsorption data for nitrogen and methane presented in Chapter 2. Hydrogen and oxygen adsorption tests were also performed in the most promising samples. The potential of such sorbents for carbon CO_2/CH_4 separation via batch vacuum pressure swing adsorption (VPSA) was also evaluate by numerical analysis. The work presented in this chapter was published in 2008. [23]

In Chapter 4, we discuss the development of a modified cubic transport model that includes the dependence on size polydispersity. Particle size measurements were fitted to Gaussian, lognormal, and gamma distributions to obtain a particle size distribution function that best describes the studied materials. In order to obtain accurate values for the diffusion time constant, it was necessary to consider the crystal shape, crystal size, and most importantly, the particle size distribution.

Chapter 5 focuses on the bottom-up synthesis of a new family of titanium silicate (TS) nanostructured sorbent materials with flexible characteristics involving templated synthesis. In addition to preparing these novel materials, the effectiveness of template removal was also studied, which is important in order to maximize the adsorption volume while still maintaining the crystallinity of the structure.

Among the several compositional variants of the new TS developed in our lab, UPRM-4d showed what appears to be a functional flexible high capacity titanium silicate framework based on a known Zorite-like recipe employing a templated synthesis method. The post-detemplated material potential as a CO_2 selective sorbent is also discussed in Chapter 6, including a direct comparison with in-house prepared Sr-ETS-4.

Finally, the more relevant contributions of the thesis are presented in Chapter 7. Complementary data and additional experiments are included in the Appendix.

1.4 References

[1] Virta, R. L., Zeolites. In *U.S. Geological Survey Minerals Yearbook*, 2001.

[2] Yang, R. T., *Gas Separation by Adsorption Processes*. Butterworth: Boston, MA, 1987. Reprinted by Imperial College Press: London, 1997.

[3] Yang, R. T., *Adsorbents: Fundamentals and Applications*. Wiley-Interscience: New Jersey, 2003.

[4] Ruthven, D. M., Past Progress and Future Challenges in Adsorption Research. *Ind. Eng. Chem. Res.* **2000,** *39*, (7), 2127-2131.

[5] Dabrowski, A., Adsorption - From Theory to Practice. *Adv. Colloid Interface Sci.* **2001,** *93*, (1-3), 135-224.

[6] Szostak, R., *Molecular Sieves: Principles of Synthesis and Identification*. Van Nostrand Reinhold: New York, 1989.

[7] Breck, D. W., *Zeolite Molecular Sieves*. Wiley: New York, 1973.

[8] Poshusta, J. C.; Tuan, V. A.; Pape, E. A.; Noble, R. D.; Falconer, J. L., Separation of Light Gas Mixtures Using SAPO-34 Membranes. *AIChE J.* **2000,** *46*, (4), 779-789.

[9] Habgood, H. W., The Kinetics of Molecular Sieve Action: Sorption of Nitrogen-Methane Mixtures by Linde Molecular Sieve 4A. *Can. J. Chem.* **1958,** *36*, 1384.

[10] Ackley, M. W.; Yang, R. T., Kinetic Separation by Pressure Swing Adsorption: Method of Characteristics Model. *AIChE J.* **1990,** *36*, (8), 1229-1238.

[11] Falamaki, C.; Mohammadi, A.; Sohrabi, M., N_2 and O_2 Adsorption Properties of an Iranian Clinoptilolite-Rich Tuff in the Original and Pre-Exchanged Forms. *Colloid. Surf. A* **2004,** *246*, (1-3), 31-37.

[12] Frankiewicz, T. C.; Donnelly, R. G., Methane/Nitrogen Gas Separation over the Zeolite Clinoptilolite by the Selective Adsorption of Nitrogen. *ACS Symp. Ser.* **1983,** *223*, 213-233.

[13] Ackley, M. W.; Yang, R. T., Adsorption Characteristics of High-Exchange Clinoptilolites. *Ind. Eng. Chem. Res.* **1991,** *30*, (12), 2523-2530.

[14] Jayaraman, A.; Hernandez-Maldonado, A. J.; Yang, R. T.; Chinn, D.; Munson, C. L.; Mohr, D. H., Clinoptilolites for Nitrogen/Methane Separation. *Chem. Eng. Sci.* **2004,** *59*, (12), 2407-2417.

[15] Jayaraman, A.; Yang, R. T., Tailored Clinoptilolites for Nitrogen/Methane Separation. *Ind. Eng. Chem. Res.* **2005,** *44*, (14), 5184 -5192.

[16] Kuznicki, S. M.; Bell, V. A.; Jacubinas, R. M.; Nair, S.; Braunbarth, C. M.; Hillhouse, H. W.; Tsapatsis, M., ETS-4 Pore Contraction: The Molecular Gate Effect. *Abstr. Pap. ACS* **2001,** *221*, U726-U726.

[17] Mintova, S.; Valtchev, V.; Angelova, S.; Konstantinov, L., Kinetic Investigation of the Effect of Na, K, Li and Ca on the Crystallization of Titanium Silicate ETS-4. *Zeolites* **1997,** *18*, (4), 269-273.

[18] Philippou, A.; Anderson, M. W., Structural Investigation of ETS-4. *Zeolites* **1996,** *16*, (2-3), 98-107.

[19] Braunbarth, C.; Hillhouse, H. W.; Tsapatsis, M.; Burton, A.; Lobo, R. F.; Jacubinas, R. M.; Kuznicki, S. M., Structure of Strontium Ion-Exchanged ETS-4 Microporous Molecular Sieves. *Chem. Mater.* **2000,** *12*, (7), 1857-1865.

[20] Hernandez-Maldonado, A. J.; Yang, R. T.; Chinn, D.; Munson, C. L., Partially Calcined Gismondine Type Silicoaluminophosphate SAPO-43: Isopropylamine Elimination and Separation of Carbon Dioxide, Hydrogen Sulfide, and Water. *Langmuir* **2003,** *19*, (6), 2193-2200.

[21] Hartmann, M.; Kevan, L., Transition-Metal Ions in Aluminophosphate and Silicoaluminophosphate Molecular Sieves: Location, Interaction with Adsorbates and Catalytic Properties. *Chem Rev* **1999,** *99*, (3), 635-663.

[22] Rivera-Ramos, M. E.; Hernandez-Maldonado, A. J., Adsorption of N_2 and CH_4 by Ion-Exchanged Silicoaluminophosphate Nanoporous Sorbents: Interaction with Monovalent, Divalent and Trivalent Cations. *Ind. Eng. Chem. Res.* **2007,** *46*, 4991-5002.

[23] Rivera-Ramos, M. E.; Ruiz-Mercado, G. J.; Hernández-Maldonado, A. J., Separation of CO_2 from Light Gas Mixtures using Ion-Exchanged Silicoaluminophosphate Nanoporous Sorbents. *Ind. Eng. Chem. Res.* **2008,** *47*, 5602-5610.

Chapter 2

Adsorption of N_2 and CH_4 by Ion-Exchanged Silicoaluminophosphate Nanoporous Sorbents: Interaction with Monovalent, Divalent and Trivalent Cations

The present chapter focuses on the development of ion-exchanged M^{n+}-SAPO-34 materials for similar-size molecular pair adsorption at temperatures and pressures that approach ambient conditions. In our study, we have exchanged the extraframework cations of Na^+-SAPO-34 with monovalent, divalent, and trivalent cations, such as Ag^+, Mg^{2+}, Ca^{2+}, Sr^{2+}, Ti^{3+}, and Ce^{3+}, in order to understand the effect of these species on the adsorption capacity of nitrogen and methane. This pair of sorbates has been chosen given the similar general sorption characteristics of both molecules. Although both are non-polar species, there are some aspects to be considered that may account for successful separation.

2.1 Introduction

Silicoaluminophosphates (SAPOs) are crystalline nanoporous (or microporous according to the IUPAC classification for pore diameters) materials formed by silicon, aluminum, phosphorous, and oxygen atoms in tetrahedral coordination.[1-3] The atoms are arranged in an orderly fashion and form frameworks with a variety of geometries. SAPO-34, which is the selected material for this study, has the framework characteristics of natural zeolite Chabazite (CHA) (Figure 2-1). This molecular sieve includes 8-ring apertures (~ 4 Å) that permit access to a 3-D channel and barrel-shaped cage system.[4, 5] Such geometry allows molecules with small kinetic diameters to easily diffuse through the crystal structure. SAPOs also have a framework with a net charge that varies depending upon how the silicon substitution into an aluminophosphate group is achieved. That is, if silicon is substituted for aluminum, phosphorous, or both, the resulting net charge will be +1, -1 or 0, respectively.[6-9] Studies have shown that usually the second and third substitution mechanisms are present during the crystallization process.[6, 7, 10-13] Therefore, the SAPOs framework requires the presence of counterbalance species, such as cations and/or anions. These ions affect the pore size and geometry, causing potential blockage of certain molecules and limiting the diffusion of some species through the structure. In addition, these extraframework species provide effective functionalization of the sorbent surface since they can induce specific sorbate-to-sorbent energy interactions. After specific tailoring, these sorbents could have an extraordinary potential for separation applications involving adsorption of “small” molecules.

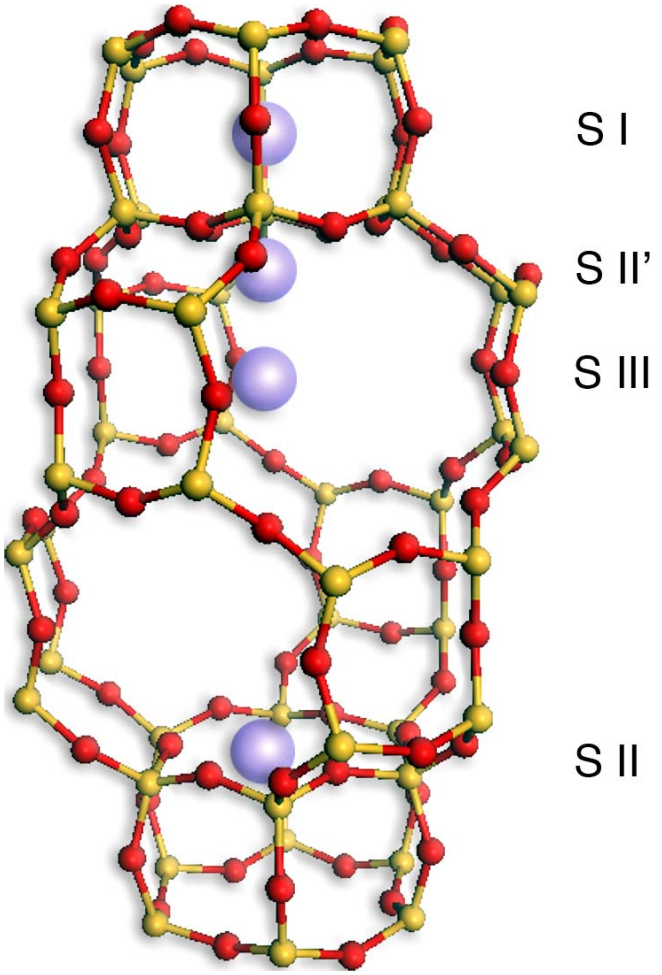

Figure 2-1. Chabazite framework with possible cation positions (blue colored spheres). Tetrahedral atoms (yellow) connected through oxygen bridges (red).

Several cation sites in Chabazite-like materials have been identified (see Figure 2-1).[14, 15] The principal cation positions are in the center of a hexagonal prism (Site I), in the center of the six-ring window (Site II), in the cavity displaced from the six-ring window (Site II'), and near the center of the eight-ring window (Site III). Given the influence of cation sites in adsorption processes, the next sections will occasionally refer to these positions.

2.2 Previous Work

Lok and co-workers (1984) were the first to patent a new family of crystalline nanoporous SAPOs, with a broad range of structure and composition (e.g. SAPO-34).[4, 5] It has been demonstrated since then that a change in the adsorption and catalytic properties of this material can be accomplished by synthesis and post-synthesis modification techniques.[16-18] SAPO-34 materials have attracted much of the attention in catalytic applications due to medium acidic strength properties.[4, 19] For example, this material is used as a catalyst for light olefin synthesis, such as ethylene synthesis from methanol.[20, 21] In 1997 Zhang et al. synthesized for the first time SAPO-34 membranes supported on alumina disks and reported their single gas permeability.[22] Falconer and co-workers (1998) also prepared membranes with H^+-SAPO-34, but deposited as a continuous layer on α-alumina tubular supports to separate CO_2 from CH_4 and other gases.[23] Years later, Falconer and co-workers re-tested these membranes for separation of N_2/CH_4 and determined that the selectivity for N_2 in the mixture was low because of the small difference in kinetic diameter.[24] It should be mentioned that the light gas mixture is not limited by single-file diffusion through the sorbent because the diameter of the SAPO-34 cage (ca. 12-14 Å) is more than the sum of the diameters of N_2 and CH_4, and each cage has six pores. Thus, there also exists the possibility of separating light gas mixtures by differences in diffusivity.[24]

2.3 Experimental Section

2.3.1 Sorbent Synthesis. Na^+-SAPO-34 was prepared by hydrothermal crystallization of saturated gels containing a molecular structure-directing agent (SDA).[2, 20] Reactants used were aluminum isopropoxide (Aldrich), *o*-phosphoric acid (85wt%, Sigma-Aldrich), colloidal silica (30wt% SiO_2 LUDOX AM-30, Sigma-Aldrich), sodium hydroxide (Sigma), tetraethylammonium hydroxide (TEAOH, Fluka), and distilled/deionized water. Two similar batches were prepared using saturated gels each with the following oxide molar composition formula: $0.5(TEA)_2O{:}0.3Na_2O_3{:}1.3Al_2O_3{:}0.6SiO_2{:}P_2O_5{:}60H_2O$. The mixture was heated to 473 K inside a sealed Teflon lined autoclave under autogenous pressure for approximately 8 days. The final product was then filtered and washed with copious amounts of deionized/distilled water. The resulting solid was finally dried at 373 K for 24 hours in a forced convection oven. The TEAOH was removed from the nanoporous material framework by calcination methods using flowing air in a computer-controlled muffle furnace. Using a ramp procedure at a heating rate of 10 K/min, the sample was heated to three consecutive temperature set points: 1 hour at 373 K, 1 hour at 473 K, and finally 15 hours at 773 K. It should be mentioned that better porosity and crystal quality were obtained when the samples were pretreated in vacuum for 24 hours at 673 K.

2.3.2 Preparation of Ion-Exchanged Materials. The Na^+-SAPO-34 samples were functionalized by means of ion-exchange with Mg^{2+}, Ca^{2+}, Sr^{2+}, and Ce^{3+} cations, respectively. The ion-exchanges were performed each in a one step equilibration batch system using a high cation chloride salt/zeolite aqueous solution with an equivalent molar

ratio of 10:1. The exchange was performed under vigorous stirring at 333 K for 24 hours.[25] The Ag^+ ion-exchange was prepared also by conventional ion-exchange using a $AgNO_3$ solution, equivalent ratio (5:1) of Ag^+, at 298 K for 24 hours in a water bath shaker.[26] After the ion-exchange step, samples were filtered and washed with deionized/distilled water and dried at 373 K for 24 hours in a forced convection oven. Due to silver cations photosensitivity,[27, 28] the Ag^+-SAPO-34 samples were protected from direct light exposure. It should be mentioned that the pH values of the ion-exchange solutions were kept between 4.7 and 8.9 to reduce formation of hydrolysis by-products.[29] The Ti^{3+} ion-exchange procedure was similar to that of the Ag^+-SAPO-34 preparation. However, the $TiCl_3$ ion-exchange solution pH was kept at 2.0.

2.3.3 Sorbent Characterization. The materials were characterized by X-ray powder diffraction (XRD), scanning electron microscopy (SEM), and energy-dispersive analysis by X-rays (EDAX). XRD patterns of Na^+-SAPO-34 were obtained using a Siemens B500 DACO-MR unit equipped with a CuK_α target operating at 40 kV and 100 mA with a scanning rate of 0.02 degrees per second. The diffraction patterns were used to corroborate the crystallinity of the synthesized materials. SEM micrographs of Na^+-SAPO-34 were obtained using a JEOL JSM 5410 LV. The images were obtained following standard procedures for poorly conducting samples. Elemental identification of surface features for all the SAPO-34 variants were obtained using a JEOL JSM-6460LV/EDAX instrument. The intensity reading's relative error was approximately ±4.5%.

2.3.4 Adsorption Equilibrium Isotherms and Uptake Rates. Equilibrium isotherm and diffusion adsorption data were obtained using a static volumetric adsorption system (Micromeritics ASAP 2020) outfitted with a turbo molecular drag pump. Adsorbate gases used were N_2 (High Purity Grade, Linde), CH_4 (Ultra High Purity Grade, Praxair), and He (High Purity Grade, Linde). The latter was used as a backfill gas after sorbent activation. The inert gas was later removed via ultra-high vacuum prior to adsorption tests. All SAPO samples were previously treated in vacuum at 648 K to remove water molecules strongly bound inside the structure.[27] The temperature ramp, evacuation rate, and vacuum set used were 10 K/min, 50 mmHg/s, and 20 μmHg, respectively. Equilibrium and uptake runs were performed at temperatures ranging from 273 to 348 K. The temperature was kept constant by means of either a water bath or a heating blanket.

Equilibrium adsorption data for Na^+-SAPO-34 were fitted using the Langmuir equation model (eq 2-1):

$$q = q_{sat}\frac{K_L P}{1 + K_L P} \qquad (2\text{-}1)$$

where P is the partial pressure of the sorbate, K is the affinity constant, q is the adsorbed amount at a pressure P and q_{sat} is the saturated adsorbed amount. A justification for use of this and other isotherm models will be given in the Results and Discussion section of this Chapter.

Equilibrium adsorption data for ion-exchanged M^{n+}-SAPO-34 were fitted using the Sips equation (Langmuir-Freundlich) (eq 2-2).[30] For Langmuir-Freundlich isotherms, the model equation has three adjustable parameters:

$$q = q_{sat} \frac{(K_{LF}P)^{1/n}}{1 + (K_{LF}P)^{1/n}} \qquad (2\text{-}2)$$

where n is the system heterogeneity parameter, which is usually greater than unity. The larger the parameter, the more heterogeneous the system.[30, 31] When $n \rightarrow 1$, the Langmuir model (Eqn. 2) is obtained.

Frequently, kinetic data for the adsorption process are correlated in terms of a diffusion time constant (D/L^2), where D and L are the diffusion constant and characteristic length of diffusion. Diffusion time constants were estimated by fitting fractional uptake data (F) with the theoretical curve derived from a phenomenological model that depends on the crystal geometry.[32] Several phenomenological transport models for different crystal geometries were studied.

2.3.5 Surface Area and Pore-Size Determination. All samples were tested for surface area and pore-size determination. Pore-size distribution (PSD) was obtained by means of methods developed by Horváth and Kawazoe (HK) in 1983.[33, 34] Given the sample's channel-pore dimensions and isotherms shape, it was necessary to use the HK correction developed by Cheng and Yang (CY).[34, 35] The HK-CY model strongly depends on the pores' shape (slit, cylindrical, or spherical) as well as surface potential characteristics such as overlapping that occurs when two surfaces are relatively close to each other (in the molecular size range). The latter is clearly the case observed in SAPO-34 samples.

2.3.6 Isosteric Heat of Adsorption. The isosteric heats of adsorption were calculated using the Clausius-Clapeyron equation (eq 2-3) and pure component equilibrium adsorption data at different temperatures and constant surface loading. The isosteric heat of adsorption is given by:

$$\left(\frac{d\ln P}{d(1/T)}\right)\Bigg|_{q=const} = \frac{\Delta H_{ads}}{R} \qquad (2\text{-}3)$$

where R is the gas constant, P is the equilibrium pressure at a particular coverage q , and T is the absolute temperature.

2.4 Results and Discussion

2.4.1 Sorbent Characterization. Figure 2-2 shows the XRD pattern for Na^+-SAPO-34 samples. The data match well those reported for Na^+-SAPO-34 synthesized with TEAOH[2] and morpholine[36] templates, respectively. A SEM micrograph of Na^+-SAPO-34 (Figure 2-3) showed crystals of several micrometers in size (between 0.5 and 1.5 μm), most of them exhibiting a cubic geometry. These results are in agreement with those obtained by Tan et al. and Simonot-Grange et al. who synthesized Na^+-SAPO-34 materials using triethylamine and TEAOH as templates, respectively.[4, 37] It should be mentioned at this point of the discussion that the observed Na^+-SAPO-34 polydispersity has not been thoroughly described in the literature. As previously considered by Ruthven and co-workers, this phenomenon is known to considerably affect diffusive transport.[32, 38, 39]

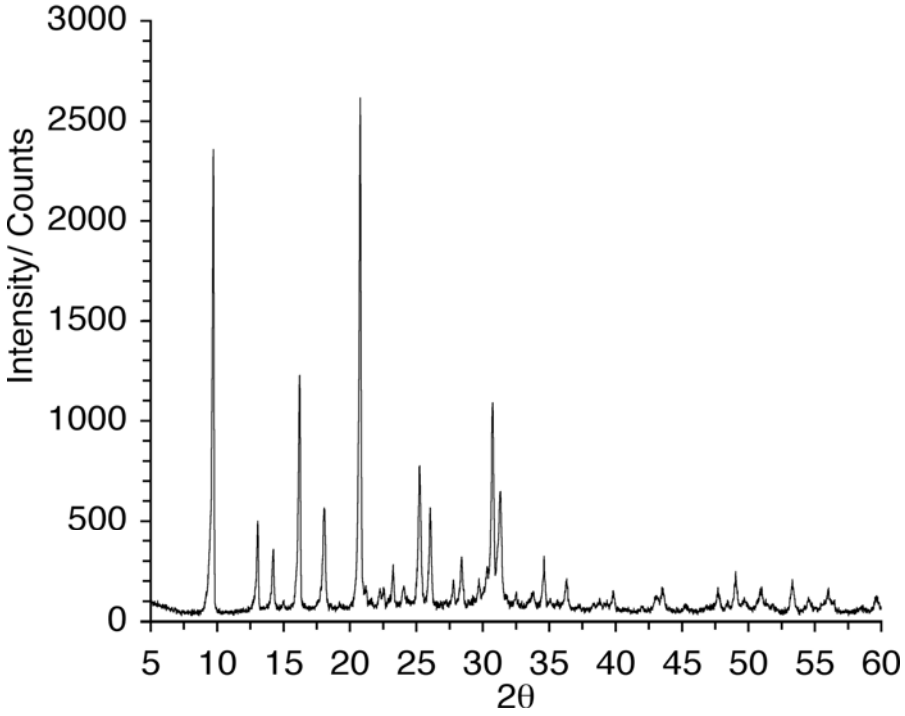

Figure 2-2. Na^+-SAPO-34 X-ray powder diffraction pattern.

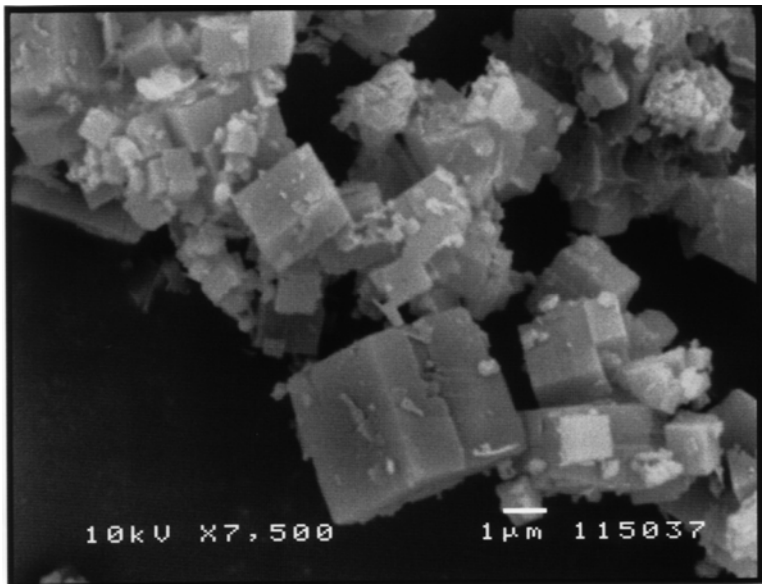

Figure 2-3. SEM micrograph of Na^+-SAPO-34.

Apparent unit cell composition of the materials as determined by EDAX probe microanalysis measurements are presented in Table 2-1. The Na^{+}-SAPO-34 composition is also in good agreement with results found elsewhere.[2, 40, 41] It can be corroborated from the unit cell composition that ion-exchange, although not complete, was achieved to a significant extent for all cases. It is evident from the estimated unit cell formulae for the monovalent (Ag^{+}) and divalent (Mg^{2+}, Ca^{2+}, Sr^{2+}) ion-exchanged M^{n+}-SAPO-34 that changes in Si, Al and P composition were negligible. The minor observed variations were probably due to small deviations in the energy dispersive spectrometer (EDS). However, the Na^{+}-SAPO-34 functionalization with trivalent cations (Ti^{3+}, Ce^{3+}) resulted in additional or considerable framework changes. The observed variation in tetrahedral atom concentration comes mainly from the functionalization stage where the pH of the aqueous solution was < 5. The trivalent cations in the aqueous solution produced a reduction of silica in the framework (see Table 2-1) and, consequently, a reduction in the crystallinity of the material. It is also plausible that the silica reacted with the polyvalent cations and was subsequently removed from the sample during the post-filtration process. The polyvalent cations could result from small hydrolysis reactions.[42-44] XRD analysis for Ce^{3+}-SAPO-34 and Ti^{3+}-SAPO-34 shows broader peaks when compared to those found for Na^{+}-SAPO-34. This observation correlates well with the changes observed in unit cell compositions.

Table 2-1. Estimated Unit Cell Composition for Ion-Exchanged M^{n+}-SAPO-34 Sorbents

	sorbent	unit cell
batch 1	Na^{+}-SAPO-34	$\|Na^{+}_{0.90}\ H^{+}_{5.38}\|\ [Si_{4.30}\ Al_{18.99}\ P_{12.72}\ O_{72}]$
	Ag^{+}-SAPO-34	$\|Na^{+}_{0.34}\ Ag^{+}_{1.20}\ H^{+}_{4.35}\|\ [Si_{4.54}\ Al_{18.67}\ P_{12.78}\ O_{72}]$
	Sr^{2+}-SAPO-34	$\|Na^{+}_{0.31}\ Sr^{2+}_{1.05}\ H^{+}_{2.77}\|\ [Si_{4.34}\ Al_{18.42}\ P_{13.24}\ O_{72}]$
	Ce^{3+}-SAPO-34	$\|Na^{+}_{0.28}\ Ce^{3+}_{1.94}\ OH^{-}_{0.89}\|\ [Si_{3.89}\ Al_{18.66}\ P_{13.45}\ O_{72}]$
	Ti^{3+}-SAPO-34	$\|Na^{+}_{0.57}\ Ti^{3+}_{1.70}\ OH^{-}_{0.83}\|\ [Si_{3.50}\ Al_{18.67}\ P_{13.83}\ O_{72}]$
batch 2	Ca^{2+}-SAPO-34	$\|Na^{+}_{0.27}\ Ca^{2+}_{0.34}\ H^{+}_{3.05}\|\ [Si_{4.70}\ Al_{17.65}\ P_{13.65}\ O_{72}]$
	Mg^{2+}-SAPO-34	$\|Na^{+}_{0.33}\ Mg^{2+}_{0.40}\ H^{+}_{2.88}\|\ [Si_{4.90}\ Al_{17.56}\ P_{13.55}\ O_{72}]$

Nitrogen adsorption isotherms at 77 K (see Figure 2-4) were used to determine the surface area of Na^{+}-SAPO-34 materials via the Langmuir and BET approaches. Contrary to reports found elsewhere,[5, 24] our studies indicate (via a simple statistical analysis) that the former approach better adjusts to porous SAPO sorbents (pore size ~ 4-5 Å) adsorption data. A Langmuir fit is appropriate when pore filling approaches a monolayer completion behavior. In 1996, Kaneko described the process of micropore filling where the initial process has been related with the monolayer adsorption on each micropore wall.[45, 46]

The equilibrium isotherm data was also used to describe Na^{+}-SAPO-34 material's framework channel dimensions using the HK-CY approach corrected for spherical cavities.[34] The results shown in Table 2-2 are in good agreement with the Na^{+}-SAPO-34

framework characteristics reported from crystallographic data.[40] Results for the ion-exchanged M^{n+}-SAPO-34 are also presented in Table 2-2.

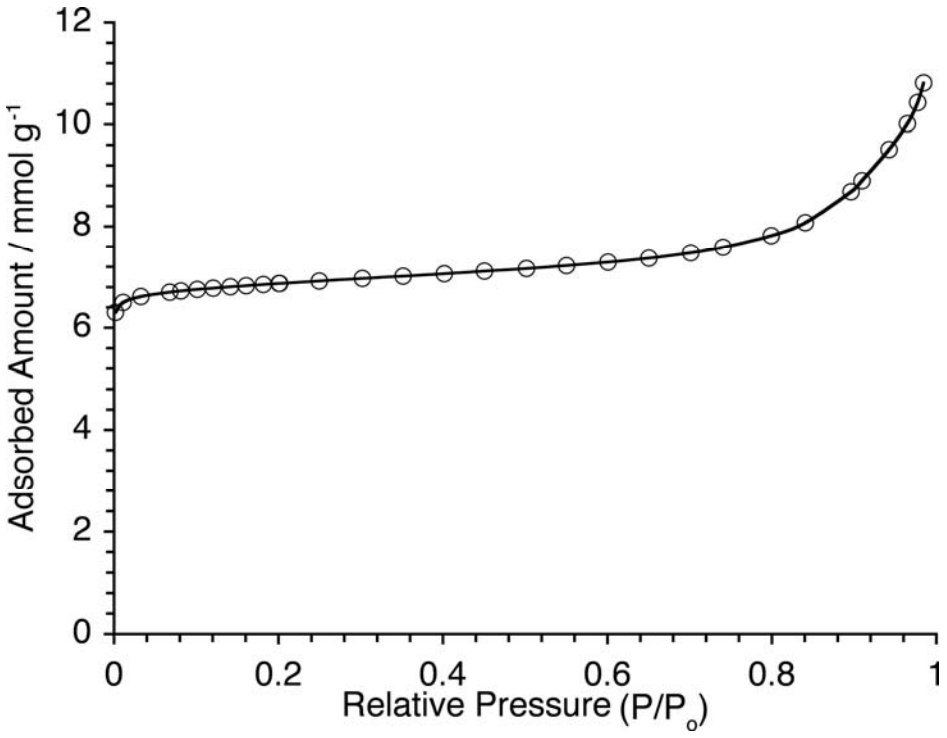

Figure 2-4. Adsorption isotherm of nitrogen on Na^+-SAPO-34 at 77 K.

Table 2-2. Surface Area and Pore Size of Ion-Exchanged M^{n+}-SAPO-34; Data Obtained from Equilibrium Adsorption of Nitrogen at 77 K

Sorbent	Langmuir Surface Area (m^2/g)	BET Surface Area (m^2/g)	Pore Volume HK (cm^3/g)	Pore Size: Median Pore Width-HK (Å)
Na^+-SAPO-34	671	543	0.24	4.37
Ag^+-SAPO-34	522	439	0.19	4.68
Ca^{2+}-SAPO-34	673	543	0.24	4.98
Mg^{2+}-SAPO-34	679	576	0.24	3.69
Sr^{2+}-SAPO-34	695	589	0.25	3.79
Ce^{3+}-SAPO-34	167	137	0.06	---
Ti^{3+}-SAPO-34	383	325	0.14	3.69

--- Not calculated.

2.4.2 Equilibrium Adsorption in Na^+-SAPO-34. Before proceeding with the remainder of the discussion, it is necessary to establish a few relevant points. A combination of textural properties, such as pore volume and pore blocking, and the interactions energies will take an important place in the uptake of the sorbates depending on the cationic species. Since both molecular species (i.e., CH_4 and N_2) are able to enter the porous structure, the selectivity edge will belong to the more symmetric sorbate. That should be the case of methane molecules, which display a spherical symmetry that permits "effortless" self-displacement within uniform pores.

Figure 2-5 shows data for nitrogen and methane equilibrium adsorption in Na^+-SAPO-34 sorbent materials at different temperatures. The low-pressure adsorption isotherms (298-348K) behave linearly, which is ideal for sorbent regeneration since most of the working capacity is recovered at moderate pressure ranges.[6, 47] In general, Na^+-SAPO-34 presented equilibrium selectivity towards methane over nitrogen. A preliminary analysis based on extrapolation of each isothermal data set indicated that the affinity constant and the saturation capacity for nitrogen adsorption decreased with temperature. Conversely, the methane adsorption affinity constant decreased while the saturation capacity increased with temperature. Nevertheless, the saturation capacity should not change with temperature because the maximum number of molecules that can fit in the material pores should not change considerably in a small temperature range.[5] Such parameter is difficult to estimate when the highest pressure is below saturation.[48] The estimated q_{sat} value should be more accurate at lower temperatures because the adsorbed amount is near the saturation capacity when compared to higher temperatures at the same pressure. Such approach would certainly reduce extrapolation errors at higher pressures.

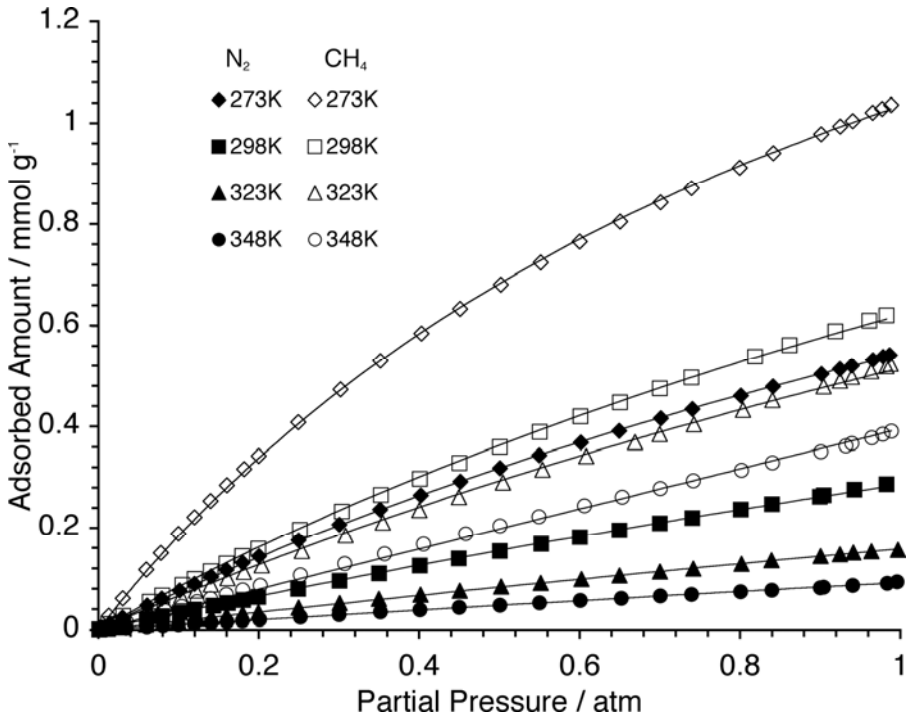

Figure 2-5. Adsorption isotherms of nitrogen and methane on Na^+-SAPO-34 at 273, 298, 323 and 348 K. Solid lines represent Langmuir fits.

The affinity constants for N_2 and CH_4 isotherms were recalculated using a q_{sat} value obtained at 273 K. Using even lower temperatures will result in negligible sorbate-sorbate interactions, which are definitely present at ambient temperature range. The resulting Langmuir parameters for the low-pressure range are listed in Table 2-3. The q_{sat} estimated by the isotherm extrapolation for N_2 and CH_4 are 1.85 and 2.13 mmol/g, respectively. It should be mentioned that the saturation value obtained here for methane matches well with the one obtained by Falconer and co-workers (2.7 mmol CH_4/g) using a similar approach.[5] The recalculated K_L values now follow the expected behavior as a function of temperature. It should be mentioned that a Langmuir isotherm model now

predicts (by extrapolation) a 3.64 wt% N_2 adsorption capacity at 298 K and higher pressure range (~10 atm)**.** The predicted adsorbed capacity is larger than the one offered by many commercially available sorbent materials which evidences the true sorbent potential.[49, 50]

Table 2-3. Langmuir Adsorption Parameters for Nitrogen and Methane on Na^+-SAPO-34 at Different Temperatures

	N_2	CH_4
T (K)	K_L (1/atm)	K_L (1/atm)
273	0.417	0.946
298	0.183	0.412
323	0.094	0.320
348	0.052	0.186

The experimental data also indicate that the isosteric heat of adsorption for Na^+-SAPO-34 is approximately -22.03 kJ/mol for N_2 and -12.18 kJ/mol for CH_4, which correlates to physical and reversible adsorption (Figure 2-6). However, this difference does not correlate with the affinity constants shown in Table 3. To explain this behavior one needs to consider other phenomena that may occur during the uptake process. For instance, the heat released during adsorption, if considerable, could be partially absorbed by the sorbent particles and some will be dissipated to the surroundings. The heat adsorbed by the sorbent increases the particle's temperature, which results in a slow down of the adsorption kinetics. The mass uptake is therefore controlled by the rate of cooling of the material during the adsorption process[31] and this should result in smaller affinity constant values.

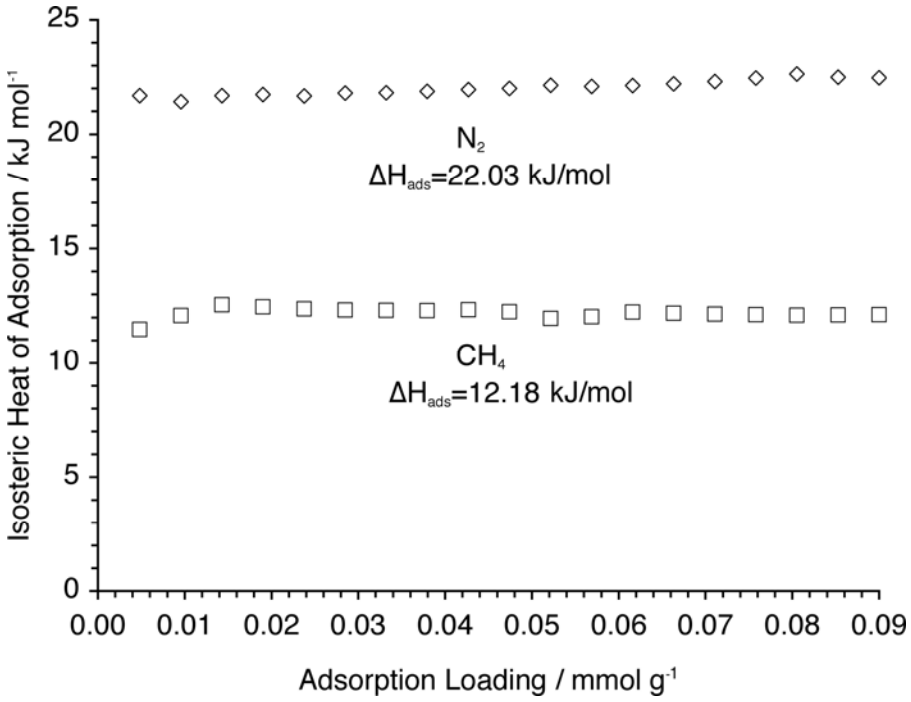

Figure 2-6. Isosteric heat of adsorption for nitrogen and methane on Na^{+}-SAPO-34.

2.4.3 Equilibrium Adsorption in Ion-exchanged M^{n+}-SAPO-34. Adsorption isotherms of ion-exchanged M^{n+}-SAPO-34 materials showed a non-linear behavior and did not follow the Langmuir model (see Figures 2-7 through 2-9). The Sips Equation (Langmuir-Freundlich), however, showed a better data adjustment and was used instead for all the ion-exchanged sorbents studied for consistency.[51-53]

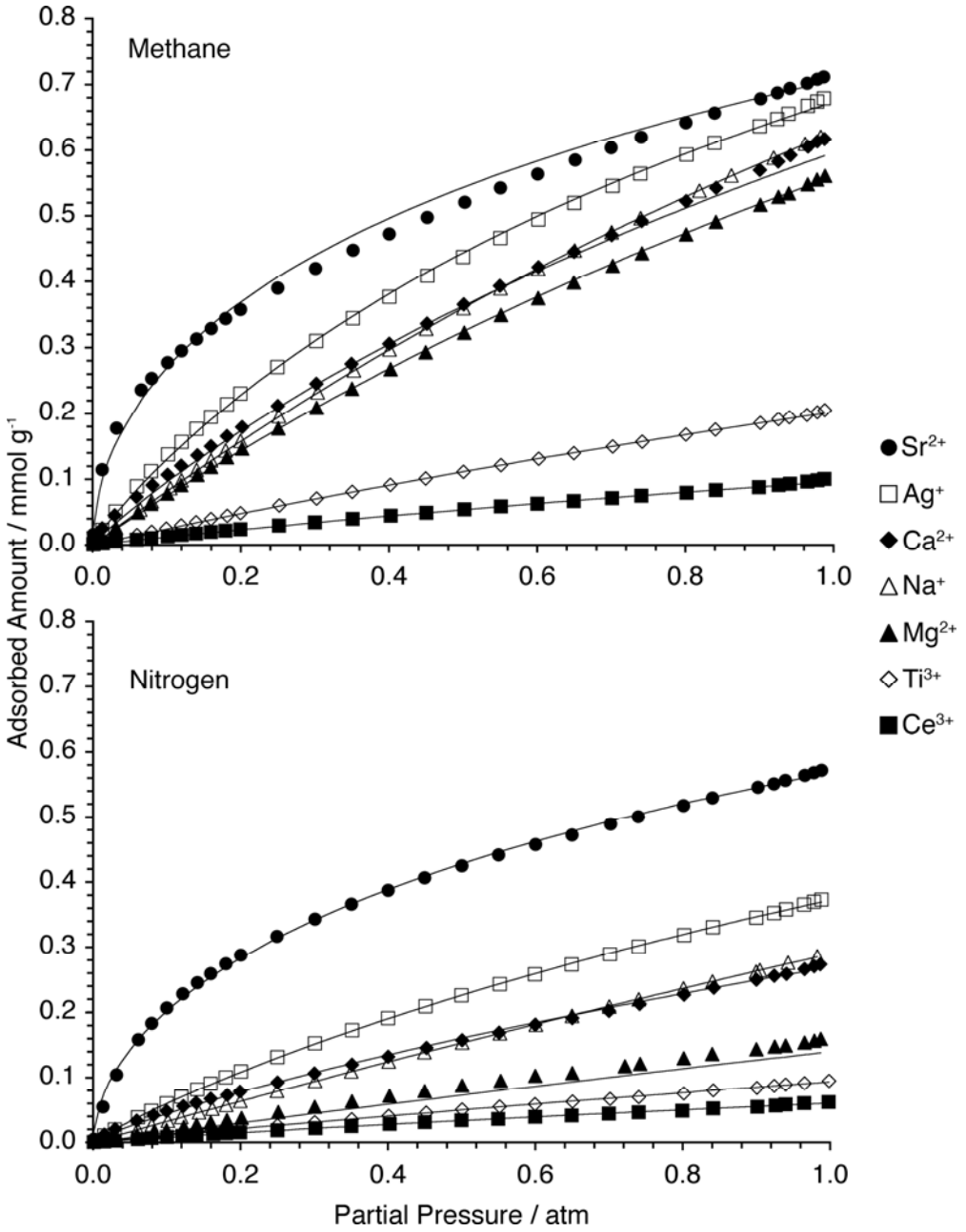

Figure 2-7. Adsorption isotherms of nitrogen and methane on ion-exchanged M^{n+}-SAPO-34 at 298 K. Solid lines represent Langmuir-Freundlich fits

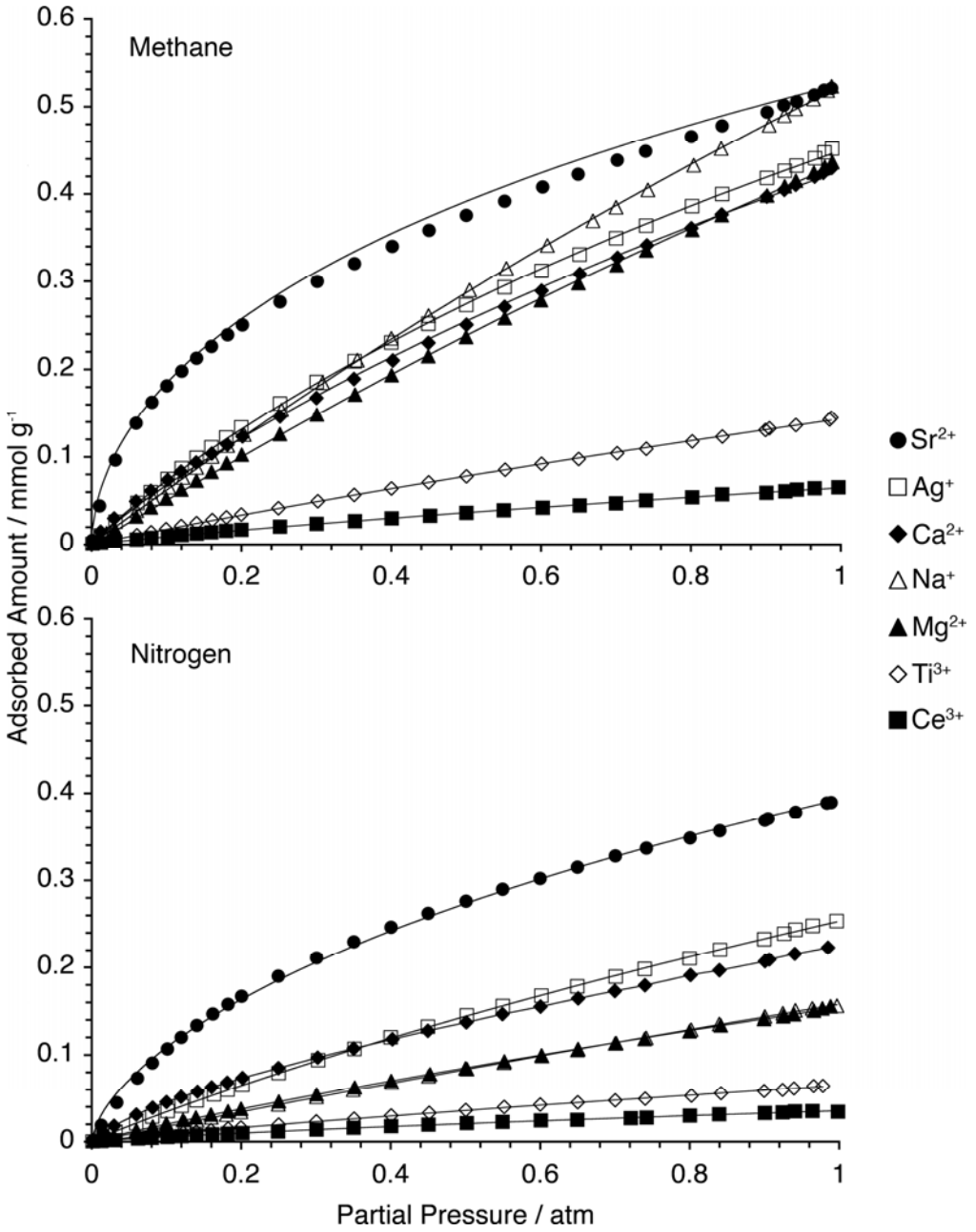

Figure 2-8. Adsorption isotherms of nitrogen and methane on ion-exchanged M^{n+}-SAPO-34 at 323 K. Solid lines represent Langmuir-Freundlich fits.

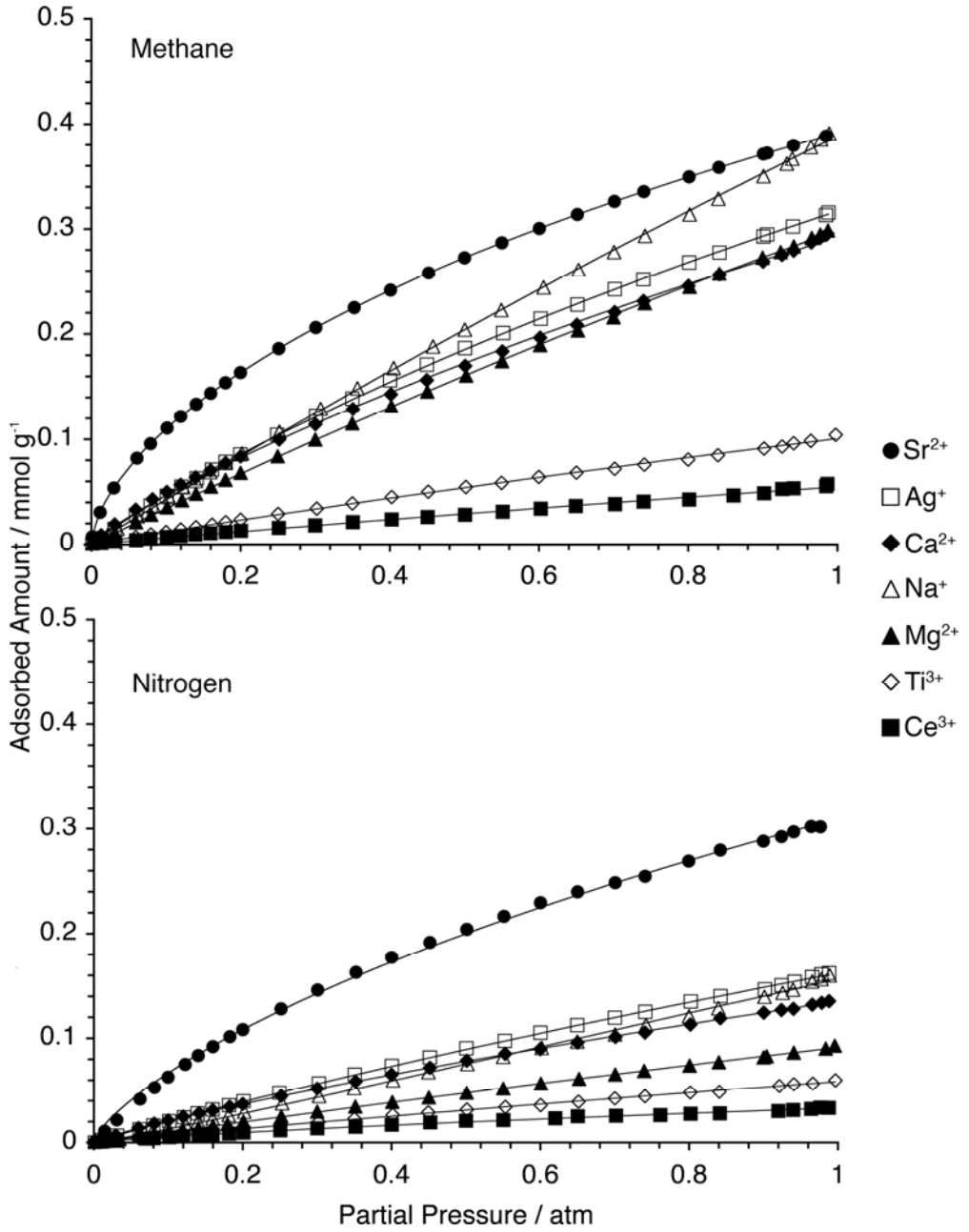

Figure 2-9. Adsorption isotherms of nitrogen and methane on ion-exchanged M^{n+}-SAPO-34 at 348 K. Solid lines represent Langmuir-Freundlich fits.

Table 2-4 shows heterogeneity factor results for these sorbents at different temperatures. In general, the heterogeneity of the system with respect to nitrogen and methane uptake changed as a function of temperature. This should be expected in nanoporous materials frameworks that usually have more sites (i.e., coordination states) available for the charge-balancing cations to occupy. The cations disperse themselves in a way that the free energy of the system results in a minimum. The distribution of many cation species on the sites depends on the temperature of heat-treatment, the nature of the cationic species, and the degree of hydration.[54-59]

Table 2-4. Heterogeneity Factor (*n*) for Ion-Exchanged M^{n+}-SAPO-34 at Different Temperatures

temp. (K)	Ca^{2+} SAPO-34		Mg^{2+} SAPO-34		Sr^{2+} SAPO-34		Ce^{3+} SAPO-34		Ag^{+} SAPO-34		Ti^{3+} SAPO-34	
	N_2	CH_4	N_2	CH_4	N_2	CH_4	N_2	CH_4	N_2	CH_4	N_2	CH_4
298	1.18	1.08	1.06	1.01	1.79	1.89	1.06	1.02	1.10	1.10	1.03	1.01
323	1.33	1.13	1.09	0.98	1.57	1.83	1.20	1.09	1.06	1.10	1.12	1.04
348	1.19	1.17	0.90	1.00	1.37	1.63	1.24	1.01	1.06	1.10	1.05	1.04

2.4.3.a Ag^{+}-SAPO-34. Silver exchanged zeolites showcase interesting color changes upon dehydration or thermal treatment.[27, 28] For the Ag^{+}-SAPO-34 samples reported here, a dark brown color was observed after the thermal degassing stage. Although the sample color depends strongly on the atomic coordination environment, it could be assumed that such color corresponds to a charge-transfer interaction between Ag^{+} and framework oxygen atoms.[28] A similar behavior has been observed in silver(I) oxides.[60]

In terms of sorption characteristics, the Ag^+-SAPO-34 nanoporous material adsorbed more nitrogen and methane when compared to the Na^+-SAPO-34 counterpart (see Figures 2-7 through 2-9). Usually, an increase in cation size of monovalent species results in a decrease in the nitrogen adsorption capacity in some zeolites.[51] However, a weak π-complexation bond can be formed between Ag^+ and nitrogen, increasing the surface interaction.[6] It is plausible that such complex formation is responsible for the resulting adsorbed amount of nitrogen in the silver exchanged sorbent, which was 30% larger when compared to that of the sodium-based material. In addition, the adsorbed amount ratio between Ag^+-SAPO-34 and Na^+-SAPO-34 increased for nitrogen and decreased for methane at higher temperature tests. The surface area of Ag^+-SAPO-34 (522 m^2/g) and the pore volume (0.19 cm^3/g) were lower than those estimated for Na^+-SAPO-34, probably due to the differences in cation radii and relative position of Ag^+ and Na^+. Since silver cations are known to form clusters[27, 28] and the distance between silver atoms in clusters are longer (2.8 Å) than the intrazeolitic Ag-O distance (2.25 Å),[28] perhaps it could be assumed that such moieties occupy sites exposed to SAPO-34 chabazite cages and windows.

Reduction of silver extraframework cations ($Ag^+ \rightarrow Ag^0$) has been observed in Ag-X, Ag-Y and Ag-LSX zeolites.[6, 27, 61] Autoreduction of Ag^+ has been shown to occur by two mechanisms in two defined temperatures regions: in the presence of zeolite water (298-523 K) or by oxygen from the zeolite lattice (400-653 K).[62, 63] The latter mechanism also requires the formation of a few Lewis sites. On the basis of structural studies of Ag-A zeolites, Jacobs and Uytterhoeven suggested the formation of linear charged clusters

(Ag^{+}-Ag^{0}-Ag^{+}) upon thermal dehydration of the zeolite.[62] Later on Gellens et al.[64] and Baker et al.[63] showed the occupancy of sites by linear charged clusters in Ag^{+} exchanged A and Y zeolites using XRD and IR spectroscopy tests. Given the clusters size, these new positively charged species would always require coordination to SAPO-34 sites exposed to cages (i.e., Sites II, II' and/or III). Therefore, even if the auto-reduction mechanism takes place in the ion exchanged Ag^{+}-SAPO-34 sorbent, the resulting species will include Ag^{+} species that will interact with nitrogen molecules.

2.4.3.b Ca^{2+}-SAPO-34. This sorbent does not display considerable changes in surface area after the functionalization step. Furthermore, the adsorbed amounts of nitrogen and methane at 298 K are comparable to those obtained for Na^{+}-SAPO-34 (see Figure 2-7). On the other hand, at higher temperatures, the functionalized sorbent tends to enhance the adsorption of nitrogen when compared also to Na^{+}-SAPO-34 (see Figures 2-8 and 2-9). It was also found that, for all the Ca^{2+}-SAPO-34 equilibrium adsorption tests, the heterogeneity factors (*n*) for nitrogen uptake were greater than those estimated for methane (see Table 2-4). At 323 K, the *n* for nitrogen adsorption was 1.33; at this temperature, Ca^{2+}-SAPO-34 adsorbed 1.45 times more nitrogen at 1 atm than Na^{+}-SAPO-34. For methane, the greatest *n* was 1.18 at 348 K; at this temperature, Ca^{2+}-SAPO-34 adsorbed 0.75 times the methane adsorbed by Na^{+}-SAPO-34.

2.4.3.c Mg^{2+}-SAPO-34. At 298 K, this material adsorbed lesser amounts of nitrogen than Na^{+}-SAPO-34. However, at higher temperatures the adsorption capacity at 1 atm remained constant. This points to a homogeneous surface, with cations perhaps occupying always similar positions. Qualitative evidence of this comes from the

heterogeneity factors (*n*) shown in Table 2-4. For the case of methane adsorption, Mg^{2+}-SAPO-34 always adsorbed less methane when compared to the unmodified material at the same temperatures.

The surface area of this magnesium-exchanged material is similar to that of the base materials, but the pore size was the smaller among the materials studied in this work (3.69 Å). This suggests that Mg^{2+} cations offer some sort of blocking to the pore window affecting the entrance of either methane or nitrogen molecules into the crystal material. Another explanation for the resulting smaller average pore size could be the cation contribution to the interaction or surface potential.

2.4.3.d Sr^{2+}-SAPO-34. The low pressure adsorption isotherms "rectangular" shape observed for Sr^{2+}-SAPO-34 indicates stronger sorbent-sorbate interactions when compared to the other ion-exchanged M^{n+}-SAPO-34 formulations (see Figures 2-7 through 2-9). These isotherms showed a greater uptake at lower pressures for both of the sorbates of nitrogen and methane. At 298 K, Sr^{2+}-SAPO-34 adsorbed 0.57 mmol/g of nitrogen, which is 1.96 times greater than the quantity adsorbed by Na^{+}-SAPO-34. At this temperature, the adsorbed amount of methane was also 1.13 times greater than that adsorbed by the unmodified material. Higher temperature adsorption isotherms for methane demonstrated that Sr^{2+}-SAPO-34 adsorbed the same amount as Na^{+}-SAPO-34 at 1 atm. On the other hand, the ratio of adsorbed nitrogen between Sr^{2+}-SAPO-34 and Na^{+}-SAPO-34 increased at higher temperatures. For the 323 and 348 K isotherms, the ratio of adsorbed nitrogen was 2.49 and 3.24, respectively. From Figure 2-7 it is clear that the nitrogen adsorption capacity increases with increasing divalent cation size.

Sr^{2+}-SAPO-34 also presented the most heterogeneous surface (largest *n* factor) among the studied materials (see Table 2-4). It is therefore plausible to state that the heterogeneity factor increases with an increase in extraframework divalent cation size in exchanged M^{n+}-SAPO-34 nanoporous sorbents.

As stated in the Introduction, pore size monitoring is essential to determine possible size exclusion capabilities. The estimated pore size of Sr^{2+}-SAPO-34 was smaller than the one obtained for Na^{+}-SAPO-34 (see Table 2-2). This also indicates that the Sr^{2+} cations are sitting near window sites (Sites II and II'), producing strong interactions with sorbates located within the relevant perimeter.

2.4.3.e Ce^{3+}-SAPO-34. As discussed before, a small part of the Ce^{3+}-SAPO-34 material crystallinity was lost during ion-exchange. However, the resulting material still presented some interesting characteristics, and this will be discussed shortly.

Adsorption isotherms for Ce^{3+}-SAPO-34 showed what appears to be blockage of pore windows (see Figures 2-7 through 2-9). If part of the surviving crystallinity includes supercages, then such blockage will be attributed to a Ce^{3+} cation (radius =1.03Å) occupying Sites III. The latter will offer the coordination stability required for a trivalent moiety.[65] As expected, the ion-exchanged material also showed a reduction in surface area (167 m^2/g) and pore volume (0.06 cm^3/g). The adsorbed amount of nitrogen and methane at 298 K and 1 atm were 0.06 and 0.10 mmol/g, respectively. These quantities

were much lower for both sorbates when compared to the adsorption performance obtained for the other materials studied.

2.4.3.f Ti^{3+}-SAPO-34. Adsorptions isotherms of Ti^{3+}-SAPO-34 behaved in a similar fashion to those obtained for Ce^{3+}-SAPO-34 (see Figures 2-7 through 2-9). Ti^{3+} are trivalent cations (radius: 0.67Å) whose preferential occupancy should be exposed sites (see Figure 2-1). This cationic radius is smaller than the one reported for the Ce^{3+} species, so pore window blockage of SAPO-34 channels should be less, and this is evident in the nitrogen and methane adsorption behavior, respectively. It should be mentioned that the estimated surface area of the titanium exchanged material (383 m^2/g) and the pore volume (0.14 cm^3/g) were greater than those found for the Ce^{3+} exchanged material. The titanium exchanged material also showcases a dark color after the degassing stage, which corresponds to the charge-transfer interaction between Ti^{3+} and the framework oxygen atoms.[28]

It should be mentioned that desorption isotherms for all the ion-exchanged sorbents confirmed the reversible sorption properties of these nanoporous materials, which makes them suitable for multiple cycle separation applications (i.e., fully regenerable). Complete sorbate desorption is achieved at ambient conditions under partial pressure swing. Experiments with additional functionalized SAPO-34 variants are presented in Appendixes A through E.

2.4.4 Isosteric Heat of Adsorption (ΔH_{ads}) in Ion-exchanged M^{n+}-SAPO-34. The experimental data indicates that the isosteric heat for each sorbate species varied according to the type of cation exchanged into the M^{n+}-SAPO-34 framework (see Figure 2-10). In general, many of the adsorbents displayed little degree of heterogeneity, which correlates well with the results shown in Table 2-4. In order to establish general trends, Table 2-5 presents the average isosteric heat of adsorption for the tested materials.

Table 2-5. Average Isosteric Heat of Adsorption for Nitrogen and Methane in Ion-Exchanged M^{n+}-SAPO-34 Sorbents

sorbent	N_2 (kJ/mol)	CH_4 (kJ/mol)
Na^{+}-SAPO-34	-22.03	-12.08
Ag^{+}-SAPO-34	-20.08	-3.35
Mg^{2+}-APO-34	-4.23	-14.90
Ca^{2+}-APO-34	-17.60	-19.28
Sr^{2+}-APO-34	-31.89	-35.97
Ce^{3+}-SAPO-34	-10.68	-16.26
Ti^{3+}-SAPO-34	-9.06	-13.56

The isosteric heat for physisorption level interactions can be related to several components. These include dispersion and repulsion energies (nonspecific) and additional components attributed to electrostatic interactions (specific). Nonspecific interactions (ϕ_D and ϕ_R) strongly depend on the polarizability, α. Although the sorbates magnetic susceptibility also affects these interactions, the contribution is not as strong as the one provided by the polarizability.[6] For the nonspecific interaction, the following dependence holds:

Dispersion:

$$\phi_D \propto -\frac{\alpha}{r_o^6} \tag{2-4}$$

Repulsion:

$$\phi_R \propto \frac{\alpha}{2r_o^6} \tag{2-5}$$

where r_0 is the contact distance between the centers of the interacting pair. Although there is a small difference in kinetics diameters between methane and nitrogen, the former has a higher polarizability (25×10^{-25} cm^{-3} for methane and 17.6×10^{-25} cm^{-3} for nitrogen).[66] Therefore, methane should exhibit higher nonspecific surface interactions.

Specific contributions (ϕ_{Ind}, $\phi_{F\mu}$ and ϕ_{FQ}) arise from charges on the solid surface. However, since nitrogen and methane do no have a permanent dipole, $\phi_{F\mu}$=0. For the remaining specific interactions, the following dependence holds:

Induction (Field-induced dipole):

$$\phi_{Ind} \propto \frac{q^2\alpha}{r_o^4} \tag{2-6}$$

Field Gradient-Quadrupole

$$\phi_{FQ} \propto \frac{qQ}{r_o^3} \tag{2-7}$$

where q is the electronic charge of the cation and Q is the quadrupole moment. Although both nitrogen and methane are non-polar, the former showcases a moderate quadrupole moment. This should make a significant contribution to the total interaction potential or heat of adsorption.

Many of the variables shown in equations 2-4 through 2-7 are interrelated or depend strongly on the nature of the sorbent extraframework cations. For instance, an increase in cation radius and charge also results in an increase in polarizability, consequentially affecting nonspecific and induction-based interactions. In addition, an increase of the cation charge results in much larger energies for polyvalent cations when compared to monovalent species. This is seen in Figure 2-10, where each sorbate interaction energy increases as the M^{n+}-SAPO-34 cation size is increased among divalent and trivalent species, respectively. In the case of the field gradient-quadrupole contribution, the effect of the cation charge is not as strong for polyvalent cations what produces a considerably decrease as the cation radii is increased. For adsorption on monovalent cations, the nitrogen quadrupole interaction should dominate.[6] That could be the case of nitrogen adsorption on Na^{+}-SAPO-34 (see Figures 2-5 and 2-6).

Although the interaction potential contributions described above cover the fundamentals behind electrostatic forces, other variables could also affect the heat of adsorption of the system. Such is the orientation of the sorbate molecules inside the sorbent and the number and positions of cations in the unit cell[6, 67] or the oxygen atoms in the sorbent framework that could produce a shielding of cations depending on the cationic radius and position inside the structure. The oxygen atoms surrounding the cation can produce a negative electric field affecting the energy interaction of the cation.

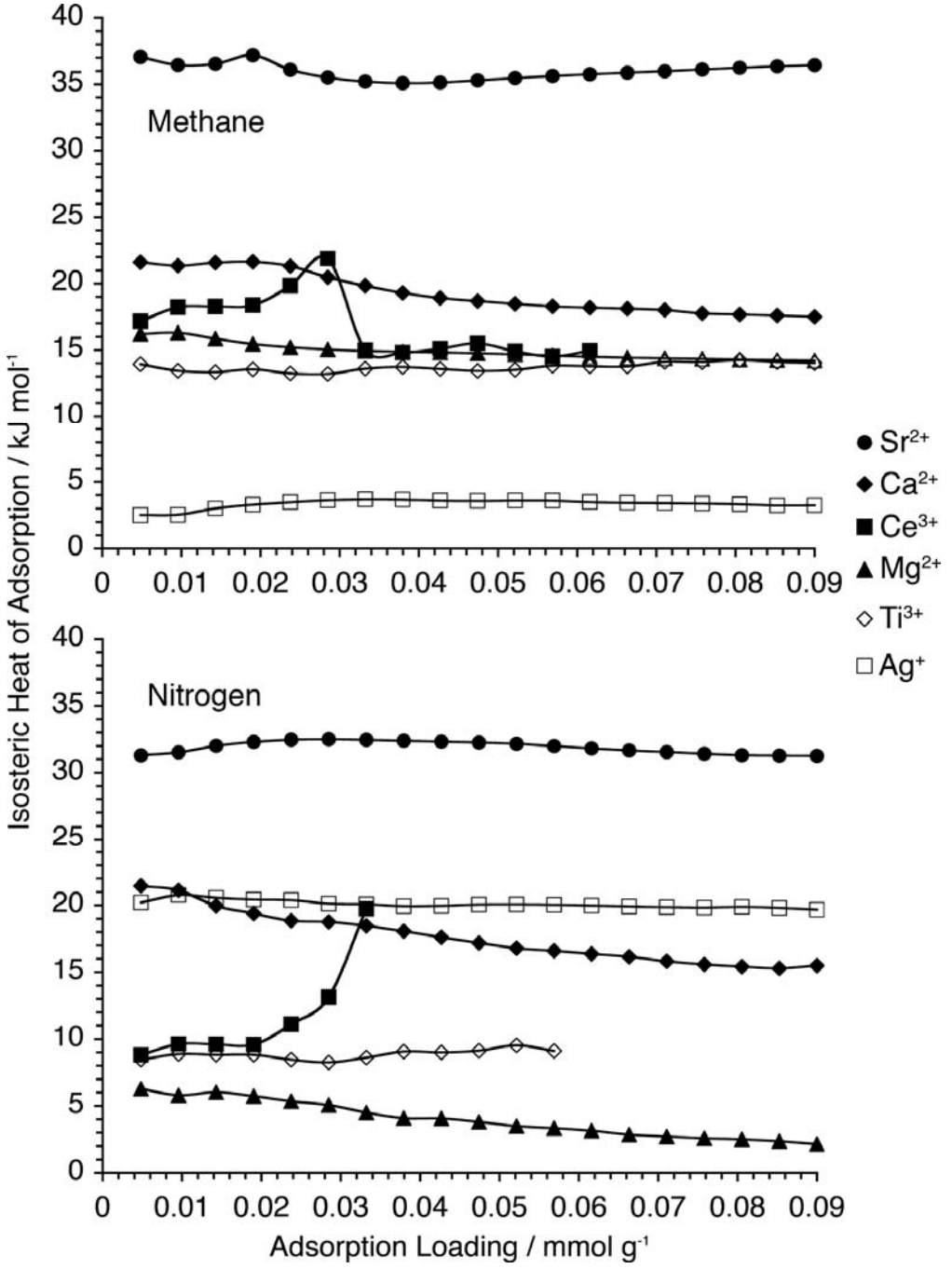

Figure 2-10. Isosteric heat of adsorption for nitrogen and methane on ion-exchanged M^{n+}-SAPO-34.

For the case of trivalent cations, the effect of the oxygen atoms on the sorbate-cation interaction could be neglected due to the plausible cation position in the center of the cage (Site III). The same could not be said about divalent cations, which usually prefer Sites II and II'. Figure 2-10 shows isosteric heats for Ce^{3+}exchanged SAPO-34. The sharp increase in heat observed for each case could be due to interaction between sorbates, which gets stronger due to the reduced space available in the supercages. The size reduction is due to the considerably large size and coordination of the trivalent transition lanthanide metal. The same cannot be said about titanium species and this leads to the conclusion that perhaps these cations are not coordinated at the supercage middle-space. It is possible that the Ti^{3+}cations prefer positions near the eight-ring windows, in a displaced fashion. Hence, the still low sorption capacities observed for this sorbent case (see Figures 2-7 through 2-9).

Among all of the sorbents tested, Ag^{+}-SAPO-34 displayed the largest nitrogen-methane heat of adsorption difference (see Table 2-5). The data also confirms that there are other contributions besides the electrostatic ones, such as weak π-complexation, to the nitrogen total interaction. The isosteric heat as a function of adsorption loading behaves in a similar manner for both sorbates (see Figure 2-10). That is, the initial heat rises to a maximum and then presents a slight drop-off as the loading increases. The observed maximum is probably the result of mutual interactions between the sorbate molecules contained inside the cage structure. In addition, this ion-exchanged material presents a rather homogeneous surface with respect to nitrogen and methane (see Table 2-4) indicating that, adsorption wise, silver cation sites appear to be of only one type.

It should be mentioned that when the pore width size is close to the kinetic diameter of the sorbate, an enhancement of the surface potential is produced resulting in greater interaction energy. This should be kept in mind when describing interactions in small pore size systems such as the one discussed in the present report.

2.4.5 Equilibrium Selectivity Factors. The equilibrium selectivity of nitrogen in relation to methane was defined as[6]

$$S_{N_2/CH_4} = \frac{q_{sat(N_2)} K_{N_2}}{q_{sat(CH_4)} K_{CH_4}} \qquad (2\text{-}8)$$

Table 2-6 shows equilibrium selectivity factors for the sorbents at different temperatures. The selectivity of the system with respect to nitrogen and methane uptake changed as a function of temperature and the nature of the cationic species. In all cases, except for Sr^{2+}-SAPO-34 at 348K, the calculated factor was < 1. After analyses of the adsorption data, the isosteric heat of adsorption and the equilibrium selectivity factor, it became clear that a combination of textural properties and the interaction energy have an important role in the uptake of the sorbates. However, for all cases (including Na^{+}-SAPO-34), the interaction contributions are not sufficiently strong to control the sorbent uptake towards nitrogen in a mixture.[23]

Table 2-6. Equilibrium Selectivity Factors ($S_{N2/CH4}$) for M^{n+}-SAPO-34 Materials at Different Temperatures

	sorbent ID						
temp. (K)	Na^{+} SAPO-34	Ca^{2+} SAPO-34	Mg^{2+} SAPO-34	Sr^{2+} SAPO-34	Ag^{+} SAPO-34	Ce^{3+} SAPO-34	Ti^{3+} SAPO-34
298	0.39	0.29	0.20	0.81	0.41	0.53	0.39
323	0.25	0.28	0.24	0.90	0.50	0.38	0.33
348	0.24	0.37	0.63	1.08	0.47	0.32	0.55

2.4.6 Fractional Uptake Rates and Diffusion Time Constants. It is customary to use solid spherical particles phenomenological models (eq 2-9) to describe transport of guest molecules in small crystals using mean equivalent particle radii,[31, 68, 69]

$$F = \frac{m_t}{m_\infty} = 1 - \frac{6}{\pi^2}\sum_{n=1}^{\infty}\frac{1}{n^2}\exp\left(-n^2\pi^2\frac{Dt}{L^2}\right) \qquad (2\text{-}9)$$

where m_t is the uptake at any time t and m_∞ is the uptake as t approaches infinity. Table 2-7 shows the boundary conditions governing this and other phenomenological transport models. After a thorough analysis of our rate of adsorption data, it was found that the diffusivity coefficient model behavior did not follow the customary phenomenological models for spherical particles (see Figure 2-11).

Table 2-7. Boundaries Conditions Used to Develop the Fractional Uptake Models

	spherical	cubic	slab
symmetry conditions (Neumann type)	z = 0 $\frac{\partial C}{\partial z} = 0$	x = y = z = 0 $\frac{\partial C}{\partial x} = \frac{\partial C}{\partial y} = \frac{\partial C}{\partial z} = 0$	z = 0 $\frac{\partial C}{\partial z} = 0$
equilibrium conditions (Dirichlet type)	z = L $C = C_f = f(P_f)$	x = y = z = L $C = C_f = f(P_f)$	z = L $C = C_f = f(P_f)$
characteristic length (L)	L = R	L = x/2 = y/2 = z/2	L=x/2
initial condition (Dirichlet type)	t = 0 $C = C_i = f(P_i)$	t = 0 $C = C_i = f(P_i)$	t = 0 $C = C_i = f(P_i)$

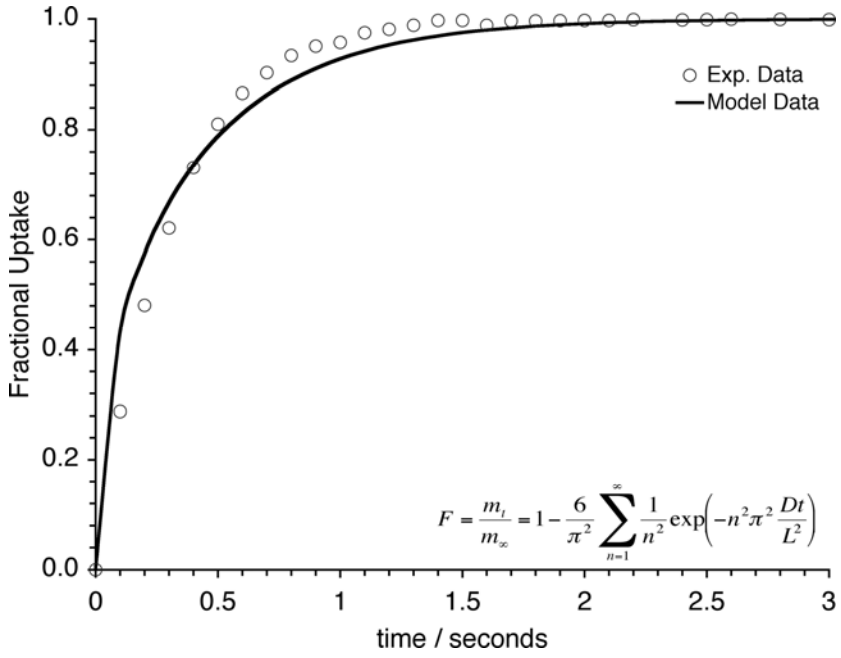

Figure 2-11. Nitrogen uptake on Na^+-SAPO-34 at 298K. The data was fitted using the spherical particles diffusion model.

Considering the evident cubic crystal geometry shown in Figure 2-3, a transport model to predict the diffusivity in crystals with cubic geometry (i.e., SAPOs) should be given by the following equation (see Appendix F for details of the derivation):[32]

$$F = 1 - \frac{8}{\pi^6}\sum_{n=0}^{\infty}\sum_{m=0}^{\infty}\sum_{p=0}^{\infty}\frac{\exp\left\{-4\left[\left(n+\frac{1}{2}\right)^2+\left(m+\frac{1}{2}\right)^2+\left(p+\frac{1}{2}\right)^2\right]\pi^2\frac{Dt}{L^2}\right\}}{\left(n+\frac{1}{2}\right)^2\left(m+\frac{1}{2}\right)^2\left(p+\frac{1}{2}\right)^2} \qquad (2\text{-}10)$$

As shown in Figure 2-12, this model resulted in a better data fit when compared to the spherical particles model counterpart. However, the former was not able to precisely adjust for both short and long time uptake data simultaneously. This could be attributed to diffusion limitations arising from the solid thickness. From Figure 2-3 the mean particle width is ca. 1 μm, which according to the literature is acceptable to diminish

transport resistance.[31, 70] In order to verify this, it was necessary to include a slab shape particles transport model in our analysis (eq 2-11).

$$F = 1 - \frac{2}{\pi^2}\sum_{n=1}^{\infty}\frac{1}{(n-1/2)^2}\exp\left(-(n-1/2)^2\pi^2\frac{Dt}{L^2}\right) \qquad (2\text{-}11)$$

As shown in Figure 2-13 the slab-based model definitely offers a better data adjustment when compared to the other case scenarios. The aforementioned model assumes that the plane where diffusion occurs is semi-infinite, indicating that the sorbate molecules are not occupying all of the crystal volume in the sorbent material. In other words, the crystal center line is empty. This could be the net effect of larger crystals being formed by smaller ones, thus prohibiting sorbate diffusion into all the crystal faces.

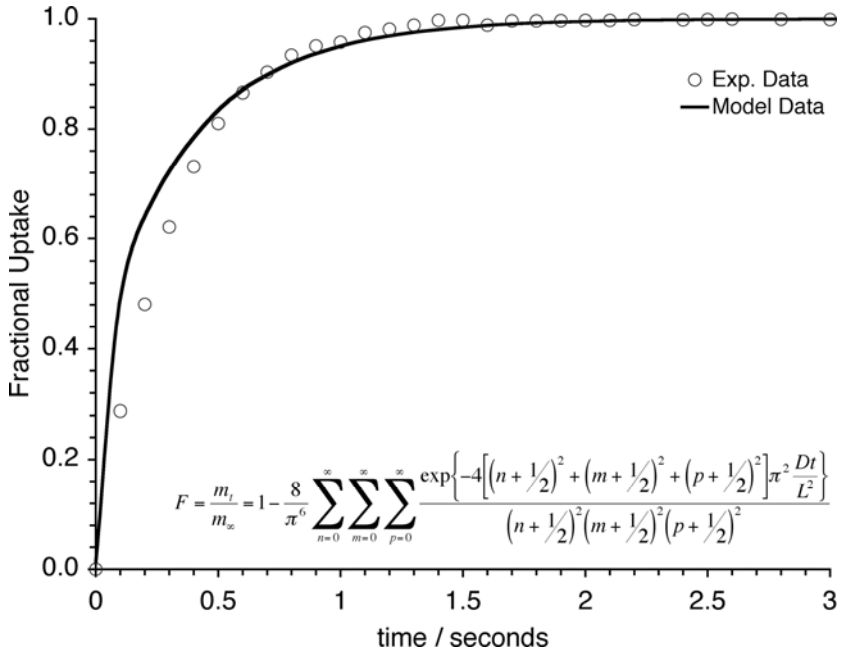

Figure 2-12. Nitrogen uptake on Na^+-SAPO-34 at 298K. The data was fitted using the cubic particles diffusion model.

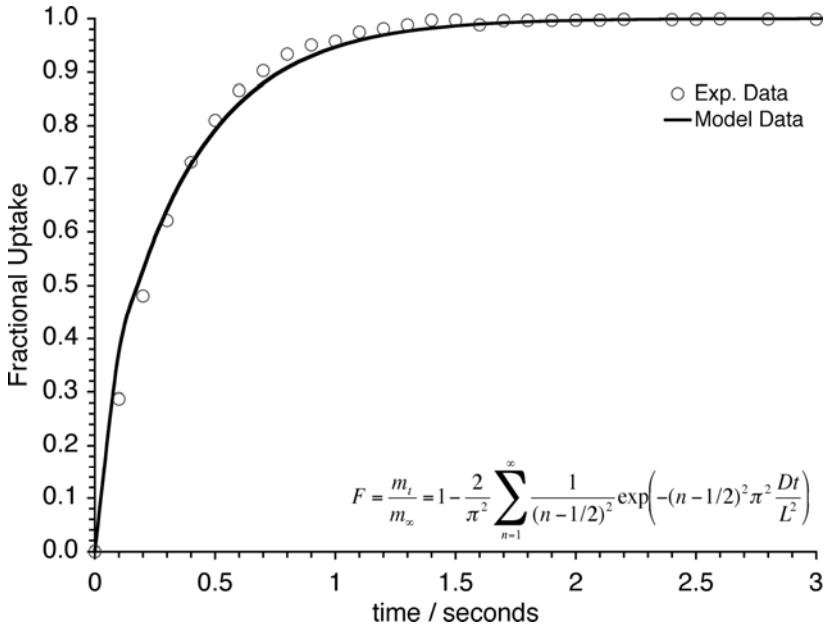

Figure 2-13. Nitrogen uptake on Na^+-SAPO-34 at 298K. The data was fitted using the slab particles diffusion model.

On the basis of the discussion so far, it is evident that assuming a mean equivalent spherical radius is a poor approximation for crystal systems analogous to ours. In order to obtain accurate values for the diffusion time constant, it is necessary to consider the crystal shape, crystal size, and most importantly, the particle size distribution of the material. Our group has been working on a modified cubic transport model (eq 2-10) to include dependence on polydispersity. This will be accomplished by employing a particle size distribution function that best describes the studied materials. Given the complexity and amount of data involved in such analysis, the results will be shown in Chapter 4. For the rest of the present discussion the authors will therefore rely on the slab model results.

Constant loading uptake studies in unmodified and ion-exchanged Na^+-SAPO-34 materials indicate that nitrogen molecules diffuse much faster than methane molecules.

For Na^+-SAPO-34, sorbates reached kinetic equilibrium in < 3 s. Such fast diffusion indicates that the sorption rates are controlled entirely by intracrystal diffusion. Table 2-8 shows diffusion time constants (D/L^2) for nitrogen and methane uptake at constant loading (0.05 mmol/g) and temperature (298 K). For the divalent cation exchanged sorbents, it was observed that diffusion time constants decrease with an increase in cation radius. The Sr^{2+}-SAPO-34 estimated diffusion time constants were the smallest among all the materials studied. This is in accordance with the isosteric heat of adsorption that indicates that this material presented the highest interaction with both sorbates. Table 2-9 shows diffusion time constants (D/L^2) for nitrogen and methane uptake at constant pressure steps (ca. 2 mmHg) and temperature (298 K). These constants have all the same magnitude, indicating that the cations are not completely blocking the pore window due to the few possible sites inside the material structure.

Table 2-8. Diffusion Time Constants at a Constant Loading (Slab Model) for Nitrogen and Methane Uptake in Ion-Exchanged M^{n+}-SAPO-34 at 298 K

		D/L^2 (1/s)	
sorbent	cation radii (Å)	N_2	CH_4
Na^+-SAPO-34	0.97 (Na^+)	1.10	0.47
Ag^+-SAPO-34	1.26 (Ag^+)	0.51	0.30
Mg^{2+}-APO-34	0.66 (Mg^{2+})	0.62	0.46
Ca^{2+}-APO-34	0.99 (Ca^{2+})	0.31	0.21
Sr^{2+}-APO-34	1.12 (Sr^{2+})	0.12	0.10
Ce^{3+}-SAPO-34	1.03 (Ce^{3+})	2.12	2.06
Ti^{3+}-SAPO-34	0.67 (Ti^{3+})	2.08	1.27

Table 2-9. Diffusion Time Constants at Constant Pressure Step

(Slab Model) for Nitrogen and Methane Uptake in Ion-Exchanged M^{n+}-SAPO-34 at 298 K

	D/L^2 (1/s)	
sorbent	N_2	CH_4
Na^+-SAPO-34	0.08	0.11
Ag^+-SAPO-34	0.12	0.14
Mg^{2+}-APO-34	0.12	0.15
Ca^{2+}-APO-34	0.11	0.13
Sr^{2+}-APO-34	0.09	0.11
Ce^{3+}-SAPO-34	0.12	0.13
Ti^{3+}-SAPO-34	0.12	0.16

2.5 Conclusions

Our results indicate that the nature of extraframework cationic species in M^{n+}-SAPO-34 greatly affect the sorbents' performance, particularly the saturation adsorption capacity towards light gases. Isosteric heat of adsorption data has shown that nitrogen molecule interaction with the sorbent increases according to the cationic species as follows: $Mg^{2+}<Ti^{3+}<Ce^{3+}<Ca^{2+}<Ag^{+}<Na^{+}<Sr^{2+}$. In terms of surface heterogeneity, Sr^{2+}-SAPO-34 sorbents behavior shows a considerable deviation from a Langmuir analogous pore filling type adsorption. It is therefore plausible to assume that the observed heterogeneity corresponds to a wide range of adsorption sites types.

Finally, the sorbents uptake data indicate that the particle morphology and, most importantly, polydispersity, play an important role in predicting diffusion coefficients. In general, ion-exchanged M^{n+}-SAPO-34 sorbents are promising for light gas mixture separations and more studies will be definitely needed to understand how to functionalize the sorbents pore windows to tailor them for size exclusion capabilities in the 0.2-0.3 Å range.

2.6 References

[1] Hartmann, M.; Kevan, L., Transition-Metal Ions in Aluminophosphate and Silicoaluminophosphate Molecular Sieves: Location, Interaction with Adsorbates and Catalytic Properties. *Chem. Rev.* **1999,** *99*, (3), 635-663.

[2] Lok, B. M.; Messina, C. A.; Patton, R. L.; Gajek, R. T.; Cannan, T. R.; Flanigen, E. M. Crystalline Silicoaluminophosphates. U.S. Patent 4,440,871, 1984.

[3] Lok, B. M.; Vail, L. D.; Flanigen, E. M. Magnesium-Aluminum-Phosphorus-Silicon-Oxide Molecular Sieve Compositions. U.S. Patent 4,758,419, 1988.

[4] Tan, J.; Liu, Z.; Bao, X.; Liu, X.; Han, X.; He, C.; Zhai, R., Crystallization and Si Incorporation Mechanisms of SAPO-34. *Micropor. Mesopor. Mat.* **2002,** *53*, (1-3), 97-108.

[5] Li, S.; Falconer, J. L.; Noble, R. D., SAPO-34 Membranes for CO2/CH4 Separation. *J. Membr. Sci* **2004,** *241*, 121.

[6] Yang, R. T., *Adsorbents: Fundamentals and Applications*. Wiley: New York, 2003.

[7] Djieugoue, M. A.; Prakash, A. M.; Kevan, L., Electron Spin Resonance and Electron Spin-Echo Modulation Studies of Synthesized NiAPSO-34 Molecular Sieve and Comparison with Ion-Exchanged NiH-SAPO-34 Molecular Sieve. *J. Phys. Chem. B* **1999,** *103*, (5), 804-811.

[8] Ashtekar, S.; Chilukuri, S. V. V.; Chakrabarty, D. K., Small-Pore Molecular-Sieves SAPO-34 and SAPO-44 with Chabazite Structure: A Study of Silicon Incorporation. *J. Phys. Chem.* **1994,** *98*, (18), 4878-4883.

[9] Sastre, G.; Lewis, D. W.; Catlow, C. R. A., Modeling of Silicon Substitution in SAPO-5 and SAPO-34 Molecular Sieves. *J. Phys. Chem. B* **1997,** *101*, (27), 5249-5262.

[10] Djieugoue, M. A.; Prakash, A. M.; Zhu, Z. D.; Kevan, L., Electron Spin Resonance and Electron Spin Echo Modulation Studies of Ion-Exchanged NiH-SAPO-17 and NiH-SAPO-35 Molecular Sieves: Comparison with Ion-Exchanged NiH-SAPO-34 Molecular Sieve. *J. Phys. Chem. B* **1999,** *103*, (34), 7277-7286.

[11] Hartmann, M.; Azuma, N.; Kevan, L., Electron-Spin-Resonance and Electron-Spin Echo Modulation Study of Ni(I) in Silicoaluminophosphate Type-5 - Adsorbate Interactions and Evidence for the Framework Incorporation of Ni(I). *J. Phys. Chem.* **1995,** *99*, (27), 10988-10994.

[12] Hartmann, M.; Azuma, N.; Kevan, L., *In Zeolites: A Refined Tool for Designing Catalytic Sites*. Elsevier: New York, 1995.

[13] Prakash, A. M.; Hartmann, M.; Kevan, L., Synthesis, Electron Paramagnetic Resonance and Electron Spin Echo Modulation Studies on Synthesized NiAPSO-41 Molecular Sieve and Comparison with Ion-Exchanged NiH-SAPO-41 Molecular Sieve. *J. Chem. Soc. Faraday T.* **1997,** *93*, (6), 1233-1241.

[14] Djieugoue, M. A.; Prakash, A. M.; Kevan, L., Electron Spin Resonance and Electron Spin Echo Modulation Studies on Reducibility, Location, and Adsorbate Interactions of N(I) in Ni(II)-Exchanged SAPO-34. *J. Phys. Chem. B* **1998,** *102*, (22), 4386-4391.

[15] Mortier, W. J., *Compilation of Extra-Framework Sites in Zeolites*. Butterworth Scientific Limited: Guildford, U.K., 1982.

[16] Akolekar, D. B.; Bhargava, S. K., NO and CO Adsorption Studies on Transition Metal-Exchanged Silico-Aluminophosphate of Type 34 Catalyst. *Appl. Catal., A* **2000,** *207*, 355-365.

[17] Robinson, S. M.; Arnold, W. D.; Byers, C. H., Mass-Transfer Mechanisms for Zeolite Ion Exchanged in Wastewater Treatment. *AIChE J.* **1994,** *40*, (12), 2045-2054.

[18] Kang, M., Effect of Cobalt Incorporated into the Framework of SAPO-34 (CoAPSO-34s) on NO removal. *J. Mol. Catal. A Chem.* **2000,** *161*, (1-2), 115-123.

[19] Shah, R.; Gale, J. D.; Payne, M. C., The Active Sites of Microporous Solid Acid Catalysts. *Phase Transit.* **1997,** *61*, (1-4), 67.

[20] Szostak, R., *Molecular Sieves: Principles of Synthesis and Identification.* Van Nostrand Reinhold: New York, 1989.

[21] Wilson, S.; Barger, P., The Characteristics of SAPO-34 which Influence the Conversion of Methanol to Light Olefins. *Micropor. Mesopor. Mat.* **1999,** *29*, (1-2), 117-126.

[22] Zhang, L. X.; Jia, M. D.; Min, E. Z., Synthesis of SAPO-34/Ceramic Composite Membranes. *Stud. Surf. Sci. Catal.* **1997,** *105*, (A-C), 2211-2216.

[23] Poshusta, J. C.; Tuan, V. A.; Falconer, J. L.; Noble, R. D., Synthesis and Permeation Properties of SAPO-34 Tubular Membranes. *Ind. Eng. Chem. Res.* **1998,** *37*, (10), 3924-3929.

[24] Poshusta, J. C.; Tuan, V. A.; Pape, E. A.; Noble, R. D.; Falconer, J. L., Separation of Light Gas Mixtures Using SAPO-34 Membranes. *AIChE J.* **2000,** *46*, (4), 779-789.

[25] Barros, M. A. S. D.; Araujo, I. F.; Arroyo, P. A.; Sousa-Aguiar, E. F.; Tavares, C. R. G., Multicomponent Ion Exchange Isotherms in NaX Zeolite. *Lat. Am. Appl. Res.* **2003,** *33*, (3), 339-344.

[26] Ju, W. S.; Matsuoka, M.; Iino, K.; Yamashita, H.; Anpo, M., The Local Structures of Silver(I) Ion Catalysts Anchored within Zeolite Cavities and their Photocatalytic Reactivities for the Elimination of N_2O into N_2 and O_2. *J. Phys. Chem. B* **2004,** *108*, (7), 2128-2133.

[27] Hutson, N. D.; Reisner, B. A.; Yang, R. T.; Toby, B. H., Silver Ion-Exchanged Zeolites Y, X, and Low-Silica X: Observations of Thermally Induced Cation/Cluster Migration and the Resulting Effects on the Equilibrium Adsorption of Nitrogen. *Chem. Mat.* **2000,** *12*, (10), 3020-3031.

[28] Sun, T.; Seff, K., Silver Clusters and Chemistry in Zeolites. *Chem. Rev.* **1994,** *94*, (4), 857.

[29] Baes, C. F.; Mesmer, R. E., *The Hydrolysis of Cations*. R.E. Krieger: Florida, 1986.

[30] Sips, R., On the Structure of a Catalyst Surface. *J. Chem. Phys.* **1948,** *16*, (5), 490-495.

[31] Do, D. D., *Adsorption Analysis: Equilibria and Kinetics*. Imperial College Press: London, 1998.

[32] Ruthven, D. M.; Loughlin, K. F., The Effect of Crystallite Shape and Size Distribution on Diffusion Measurements in Molecular Sieves. *Chem. Eng. Sci.* **1971,** *26*, 577-584.

[33] Horvath, G.; Kawazoe, K., Method for Calculation of Effective Pore Size Distribution in Molecular Sieve Carbon. *J. Chem. Eng. Jpn.* **1983,** *16*, 470.

[34] Rege, S. U.; Yang, R. T., Corrected Horvath-Kawazoe Equations for Pore-Size Distribution. *AIChE J.* **2000,** *46*, (4), 734-750.

[35] Cheng, L. S.; Yang, R. T., Improved Horvath-Kawazoe Equations Including Spherical Pore Models for Calculating Micropore Size Distribution. *Chem. Eng. Sci.* **1994,** *49*, (16), 2599-2609.

[36] Prakash, A. M.; Unnikrishnan, S., Synthesis of SAPO-34 - High-Silicon Incorporation in the Presence of Morpholine as Template. *J. Chem. Soc. Faraday T.* **1994,** *90*, (15), 2291-2296.

[37] Simonot-Grange, M. H.; Waldeck, A.; Barthomeuf, D.; Weber, G., Contribution to the Study of Framework Modification of SAPO-34 and SAPO-37 Upon Water Adsorption by Thermogravimetry. *Thermochim. Acta* **1999,** *329*, (1), 77-82.

[38] Loughlin, K. F.; Derrah, R. I.; Ruthven, D. M., Measurement of Zeolitic Diffusion Coefficients. *Can. J. Chem. Eng.* **1971,** *49*, (1), 66-&.

[39] Ruthven, D. M.; Loughlin, K. F., Effects of Particle Shape and Size Distribution on Transient Solution of Diffusion Equation. *Nat. Phys. Sci.* **1971,** *230*, (11), 69-&.

[40] Lok, B. M.; Messina, C. A.; Lyle Patton, R.; Gajek, R. T.; Cannan, T. R.; Flanigen, E. M., Silicoaluminophosphate Molecular Sieves: Another New Class of Microporous Crystalline Inorganic Solids. *ACS* **1984,** *106*, (20), 6092-9093.

[41] Vomscheid, R.; Briend, M.; Peltre, M. J.; Man, P. P.; Barthomeuf, D., The Role of the Template in Directing the Si Distribution in SAPO Zeolites. *J. Phys. Chem.* **1994,** *98*, (38), 9614-9618.

[42] Zou, H.; Lin, Y. S.; Rane, N.; He, T., Synthesis and Characterization of Nanosized Ceria Powders and High-Concentration Ceria Sols. *Ind. Eng. Chem. Res.* **2004,** *43*, (12), 3019-3025.

[43] Hartmann, M.; Clark, T.; van Eldik, R., Water Exchange Reactions and Hydrolysis of Hydrated Titanium(III) Ions: A Density Functional Theory Study. *J. Phys. Chem. A* **1999,** *103*, (48), 9899-9905.

[44] Yu, J. Q.; Feng, Z. C.; Xu, L.; Li, M. J.; Xin, Q.; Liu, Z. M.; Li, C., Ti-MCM-41 Synthesized from Colloidal Silica and Titanium Trichloride: Synthesis, Characterization, and Catalysis. *Chem. Mat.* **2001,** *13*, (3), 994-998.

[45] Kaneko, K., Micropore Filling Mechanism in Inorganic Sorbents. *Studies in Surface Science and Catalysis* **1996,** *99*, 573-598.

[46] Gil, A., Analysis of the Micropore Structure of Various Microporous Materials from Nitrogen Adsorption at 77K. *Adsorption* **1998,** *4*, 197-206.

[47] Yang, R. T., *Gas Separation by Adsorption Processes*. Imperial College Press: New Jersey, 1997; Vol. 1.

[48] Gardner, T. Q.; Falconer, J. L.; Noble, R. D., Transient Permeation of Butanes Through ZSM-5 and ZSM-11 Zeolite Membranes. *AIChE J.* **2004,** *50*, (11), 2816-2834.

[49] Kuznicki, S. M.; Bell, V. A.; Jacubinas, R. M.; Nair, S.; Braunbarth, C. M.; Hillhouse, H. W.; Tsapatsis, M., ETS-4 Pore Contraction: The Molecular Gate Effect. *Abstr. Pap. ACS* **2001,** *221*, U726-U726.

[50] Kuznicki, S. M. Preparation of Small-Pored Crystalline Titanium Molecular Sieve Zeolites. U.S. Patent 4,938,939, 1990.

[51] Peter, S. A.; Sebastian, J.; Jasra, R. V., Adsorption of Nitrogen, Oxygen, and Argon in Mono-, Di-, and Trivalent Cation-Exchanged Zeolite Mordenite. *Ind. Eng. Chem. Res.* **2005,** *44*, (17), 6856-6864.

[52] Mirajkar, S. P.; Thangaraj, A.; Shiralkar, V. P., Sorption Properties of Titanium Silicate Molecular-Sieves. *J. Phys. Chem.* **1992,** *96*, (7), 3073-3079.

[53] Reddy, K. S. N.; Eapen, M. J.; Soni, H. S.; Shiralkar, V. P., Sorption Properties of Cation-Exchanged Beta-Zeolites. *J. Phys. Chem.* **1992,** *96*, (20), 7923-7928.

[54] Barrer, R. M., *Zeolites and Clay Minerals as Sorbents and Molecular Sieves*. Academic Press: London, 1978.

[55] Vandun, J. J.; Mortier, W. J., Temperature-Dependent Cation Distribution in Zeolites : 1. A Statistical Thermodynamical Model. *J. Phys. Chem.* **1988,** *92*, (23), 6740-6746.

[56] Vandun, J. J.; Dhaeze, K.; Mortier, W. J., Temperature-Dependent Cation Distribution in Zeolites: 2. Dehydrated $Na_{13}HY$, $Na_{23}HY$, $Na_{42}HY$, $Na_{54}HY$, $Ca_{15}HY$, and $Sr_{27}Y$. *J. Phys. Chem.* **1988,** *92*, (23), 6747-6754.

[57] Vandun, J. J.; Mortier, W. J., Influence of the Temperature on the Cation Distribution in Dehydrated and Hydrated SrY Zeolites. *Zeolites* **1987,** *7*, (6), 528-534.

[58] Siegel, H.; Schollner, R.; Vandun, J. J.; Mortier, W. J., Influence of Water and Temperature on Cation Distribution in (Ca_4Na_4)-A Zeolite. *Zeolites* **1987,** *7*, (2), 148-152.

[59] Dendooven, E.; Mortier, W. J.; Uytterhoeven, J. B., Influence of Temperature and Adsorption on the Cation Distribution in Ca-Y Zeolites. *J. Phys. Chem.* **1984,** *88*, (9), 1916-1921.

[60] Butler, I. S.; Harrod, J. F., *Inorganic Chemistry: Principles and Applications*. The Benjamin/Cummings Publishing Company, Inc.: San Francisco, California, 1989.

[61] Hutson, N. D.; Yang, R. T., Structural Effects on Adsorption of Atmospheric Gases in Mixed Li,Ag-X-Zeolite. *AIChE J.* **2000,** *46*, (11), 2305-2317.

[62] Jacobs, P. A.; Uytterhoeven, J. B., Some Unusual Properties of Activated and Reduced AgNaA Zeolites. *J. Chem. Soc. Faraday Trans. 1* **1979,** *75*, 56.

[63] Baker, M. D.; Ozin, G. A.; Godber, J., Far-Infrared Studies of Sllver Atoms, Silver Ions, and Silver Clusters In Zeolites A and Y. *J. Phys. Chem.* **1985,** *89*, 305-311.

[64] Gellens, L. R.; Mortler, W. J.; Schoonheydt, R. A.; Uytterhoeven, J. B., The Nature of the Charged Silver Clusters In Dehydrated Zeolites of Type A. *J. Phys. Chem.* **1981,** *85*, 2783-2788.

[65] Jayaraman, A.; Yang, R. T., Tailored Clinoptilolites for Nitrogen/Methane Separation. *Ind. Eng. Chem. Res.* **2005,** *44*, (14), 5184 -5192.

[66] Jayaraman, A.; Hernandez-Maldonado, A. J.; Yang, R. T.; Chinn, D.; Munson, C. L.; Mohr, D. H., Clinoptilolites for Nitrogen/Methane Separation. *Chem. Eng. Sci.* **2004,** *59*, (12), 2407-2417.

[67] Tielens, F.; Geerlings, P., Adsorption Energy Surfaces in Faujasite Type Zeolites. *Chem. Phys. Lett.* **2002,** *354*, (5-6), 474-482.

[68] Hernandez-Maldonado, A. J.; Yang, R. T.; Chinn, D.; Munson, C. L., Partially Calcined Gismondine Type Silicoaluminophosphate SAPO-43: Isopropylamine Elimination and Separation of Carbon Dioxide, Hydrogen Sulfide, and Water. *Langmuir* **2003,** *19*, (6), 2193-2200.

[69] Ruthven, D. M., *Principles of Adsorption and Adsorption Processes*. Wiley: New York, 1984.

[70] Yucel, H.; Ruthven, D. M., Diffusion in 4A Zeolite. *J. Chem. Soc. Faraday T. 1* **1980,** *76*, 60-70.

Chapter 3

Separation of CO_2 from Light Gas Mixtures using Ion-Exchanged Silicoaluminophosphate Nanoporous Sorbents

The present chapter focuses on the study of ion-exchanged M^{n+}-SAPO-34 materials for the adsorption of CO_2 at temperatures and pressures that approach ambient conditions. The results are compared with adsorption data for nitrogen and methane previously reported in Chapter 2.[1] Hydrogen and oxygen adsorption tests were also performed in the most promising samples. The potential of such sorbents for carbon CO_2/CH_4 separation via batch vacuum pressure swing adsorption (VPSA) numerical simulation was also analyzed.

3.1 Introduction

The selective removal of CO_2 from mixtures of gases is necessary to help addressing environmental and energy related problems. For example, it is well known that the efficient capture of CO_2 from industrial emissions will help to mitigate greenhouse effects.[2] On the energy side, a considerable part of the natural gas reserves in the US (~17%) is treated to remove high CO_2 concentrations, as the pipeline quality for CO_2 concentration is less than 2%.[3, 4] This "contaminant" reduces the energy content of natural gas, causing it to miss the pipeline quality requirement for minimum heating value (970 BTU/ft^3).[5] Amine absorption is the most widely used method today for the removal of CO_2 from CH_4 streams, but this technique is highly complex and therefore costly. Hence, it is necessary to find alternative methods that could achieve such separation in a selective and effective way at ambient conditions. One such alternative is separation via adsorption using nanoporous materials.

3.2 Previous Work

Adsorption processes using microporous and mesoporous (known together as nanoporous) materials are promising methods for the removal of CO_2, avoiding regeneration and corrosion problems resulting from traditional solvent absorption methods. A number of nanoporous materials have already shown potential for this specific gas separation due to their small pore sizes and their narrow pore-size distribution.[6] Many studies have tried to address the CO_2 separation problem by using

microporous materials, such as 5A[7, 8], 13X[9] and Clinoptilolite[10] zeolites, mesoporous silica material SBA-15,[11, 12] and carbon molecular sieves (CMS).[13] For instance, 5A-type zeolites have been used for air purification applications, such as in adsorption devices to remove excess carbon dioxide from breathing air in aerospace vehicles cabins.[8] At a concentration of ca. 900 ppm CO_2, the 5A-zeolite adsorbed approximately 1.5-wt% of the gas. It should be mentioned that there have been also some efforts towards the development of membranes for CO_2 removal. Tsapatsis and co-workers developed a silicalite-1 membrane supported on porous alumina disks that displayed some selectivity towards CO_2.[14] The highly oriented membranes considerably improved the otherwise low selectivity exhibited by silicalite powders.[15] Recently, Falconer and co-workers reported the preparation of Na^+-SAPO-34 membranes via in situ crystallization on α-alumina tubular and porous stainless steel supports. These membranes were used to separate CO_2 from CH_4 and other gases, achieving also good selectivities.[3, 16, 17] Among all of these adsorbent alternatives, SAPO-34 materials hold the most promise and therefore are the center of attention in this chapter.

In Chapter 2 we reported that the nature of extraframework cationic species in M^{n+}-SAPO-34 considerably affects the sorbent performance, particularly the interaction with N_2 and CH_4 gases. For instance, isosteric heat of adsorption data showed that nitrogen molecule interaction with the sorbent increases according to the extraframework species as follows: $Mg^{2+}<Ti^{3+}<Ce^{3+}<Ca^{2+}<Ag^{+}<Na^{+}<Sr^{2+}$.[1]

3.3 Experimental Section

3.3.1 Sorbent Synthesis. Na^+-SAPO-34 was prepared by hydrothermal crystallization of saturated gels containing a molecular structure-directing agent (SDA).[18, 19] Details on the method and procedure were described previously at the experimental section in Chapter 2.

3.3.2 Preparation of Ion-Exchanged Materials. M^{n+}-SAPO-34 samples were prepared by ion-exchanging Na^+-SAPO-34 with Ag^+, Ca^{2+}, Mg^{2+}, Sr^{2+},Ce^{3+} and Ti^{3+} cations, respectively. Details on the methods and procedures could be found elsewhere.[1, 20, 21]

3.3.3 Adsorption Equilibrium Isotherms and Uptake Rates. Equilibrium isotherm and diffusion adsorption data were obtained using two static volumetric adsorption systems (Micromeritics ASAP 2020) outfitted with turbo molecular drag pumps. Adsorbate gases used were H_2 (Ultra High Purity Grade, Linde), O_2 (Ultra High Purity Grade, Linde), CO_2 (Ultra High Purity Grade, Praxair) and He (High Purity Grade, Linde). The latter was used as a backfill gas after the sorbent activation. The inert gas was removed via ultra-high vacuum prior to adsorption tests. All SAPO samples were treated in vacuum at 648 K to remove water molecules strongly bound inside the structure.[22] The temperature ramp, evacuation rate, and vacuum set used were 10 K/min, 50 mmHg/s and 20 μmHg, respectively. Carbon dioxide equilibrium and uptake tests were performed at temperatures ranging from 273 to 348 K and pressures up to 1 atmosphere. Tests for H_2 and O_2 were performed only at 298 K. During the experiments, the temperature was kept constant by means of either a water bath or a heating blanket. The kinetic data obtained via volumetric measurements used to determine the fractional uptakes were corrected by

the equipment dead time (~ 0.3 seconds) to avoid any instability caused by the system. The equipment collection data step was set to 0.1 seconds.

3.3.4 Isothermal VPSA Cycle Numerical Calculations. The isothermal VPSA model used in this study consisted of a simple cyclic batch separation process with consecutive adsorption steps at 1 atm. Test were performed until achieving desired product purity (e.g., 99.9999% CH_4). The pressurization step assumed no mass transfer between the gas and solid phases, which is also known as the "frozen column" state.[23] Inter-crystalline diffusion resistance was also assumed to be negligible when compared to the resistance offered by the micropores of the sorbent.[24] The equilibrium data for multicomponent adsorption was estimated using the extended Langmuir-Freundlich isotherm model, also known as the loading ratio correlation (LRC).[25] The linear driving force (LDF) model was used to describe the mass transfer involved in the various steps of the cycle.[2, 9, 24, 26] Diffusion time constants at zero coverage were estimated by fitting experimental data with the solution of the fractional uptake phenomenological model for spherical particles.[27-29] The diffusion time constant were corrected for concentration dependence using the Cheng and Yang's model,[27, 30] which is used for diffusion in zeolites where the molecules dimensions come close to that of the channel opening. Based on all of the above assumptions, the model equations for the VPSA processes are summarize in Table 3-1. The resulting differential equations were solved using a variable order solver based on the numerical differentiation formulas (NDFs)[31, 32] or by the implicit finite difference using an explicit Runge-Kutta method.[33, 34] The MATLAB algorithm is presented in Appendix G.

Table 3-1. Model Equations for the VPSA Process Simulation

		nomenclature
component mass balance	$\frac{dy_i}{dt} + \frac{RT}{P}\frac{1-\varepsilon_{bed}}{\varepsilon_{bed}}\rho_{particle}\left(\frac{dq_i}{dt} - y_i\sum_{i=1}^{n}\frac{dq_i}{dt}\right)$	D_e = effective diffusivity, m^2/s
overall mass balance	$\frac{1}{P}\frac{dP}{dt} + \frac{RT}{P}\frac{1-\varepsilon_{bed}}{\varepsilon_{bed}}\rho_{particle}\left(\sum_{i=1}^{n}\frac{dq_i}{dt}\right)$	D_o = diffusion time constant at zero coverage, 1/s
multicomponent isotherm	$q_i^* = \frac{q_{sat,i}(K_iP_i)^{1/n_i}}{1+\sum_{j=1}^{n}(K_jP_j)^{1/n_j}}$	D_v = diffusion volume, dimensionless
linear driving force model	$\frac{dq_i}{dt} = 15\frac{D_{e,i}}{R_p^{\,2}}\left(q_i^* - q_i\right)$	i = component index for CO_2 (i=1) and CH_4 (i=2)
diffusion coefficients	$D_e = \frac{\varepsilon_{particle}}{\tau_{particle}}\frac{D_S D_M}{D_S + D_M}$	K = affinity constant, atm^{-1}
	$D_S = \frac{D_o(1-\theta+(\lambda/2)\theta(2-\theta)+(1-\lambda)(\lambda/2)\theta^2}{(1-\theta+\lambda\theta/2)^2}$	m = uptake at any time t, mmol/g
	$D_M = \frac{100T^{1.75}\sqrt{\frac{M_{wCH_4}+M_{wCO_2}}{M_{wCH_4}M_{wCO_2}}}}{P\left(D_{VCH_4}^{\,1/3} + D_{VCO_2}^{\,1/3}\right)^2}$	m_∞ = uptake as t approaches infinity, mmol/g
		n = exchanged cation valence (1, 2 or 3)
		n_h = system heterogeneity parameter
		P = total pressure, atm
		P_i = partial pressure of sorbate i, atm
		q_i = solid-phase concentration, mmol/g
		q_i^* = amount of adsorption of component i in equilibrium state of mixture, mmol/g
		q = adsorbed amount at a pressure P^*, mmol/g
		$q_{sat,i}$ = saturated adsorbed amount, mmol/g
		q_c = electronic charge of the cation, Coulomb
		R_p = particle radius, m
		t = time, s
		T = system temperature, K
		y_i = gas-phase mole fraction of component i
		Greek Letters
		ε_{bed} = bed void fraction
		$\varepsilon_{particle}$ = particle porosity
		λ = blockage parameter
		θ = adsorption loading ($q_i/q_{sat\,i}$)
		$\rho_{particle}$ = particle density, kg/m^3
		$\tau_{particle}$ = particle tortuosity

3.4 Results and Discussion

3.4.1 CO_2 Pure Component Equilibrium Adsorption in M^{n+}-SAPO-34 Sorbents. A combination of textural properties, such as pore volume and pore blocking, and the interactions energies will have considerable influence in the uptake of the sorbates depending on the cationic species. A complete description of the cation species, surface area, pore volume, and unit cell composition of all the studied sorbents after the ion exchange was previously describe in the previous chapter and by Rivera-Ramos and Hernádez-Maldonado.[1] Figures 3-1 and 3-2 show data for carbon dioxide equilibrium adsorption for all the M^{n+}-SAPO-34 sorbent materials at different temperatures (273, 298, 323 and 348 K). All the sorbents displayed the classic physisorption profile, where an increase in temperature results in a decrease in uptake amounts at any given pressure. However, some of the CO_2 adsorption isotherms exhibited a considerable non-linear behavior and, therefore, did not follow the traditional pore-filling mechanism. Different models were evaluated to fit the data (i.e., Sips and Toth). The Sips equation showed better data adjustment and was therefore used for all sorbents cases for consistency.[35-37] Affinity constants for CO_2 isotherms were calculated using a q_{sat} value obtained at 273 K. The advantage of using lower temperatures to estimate this value is appropriate since sorbate-sorbate interactions become negligible. The q_{sat} estimated from the Na^+-SAPO-34 CO_2 isotherm data is 5.26 mmol/g. It should be mentioned that the saturation value obtained here for carbon dioxide matches well with the one obtained by Falconer and co-workers (5.0 mmol/g) using a similar approach.[3]

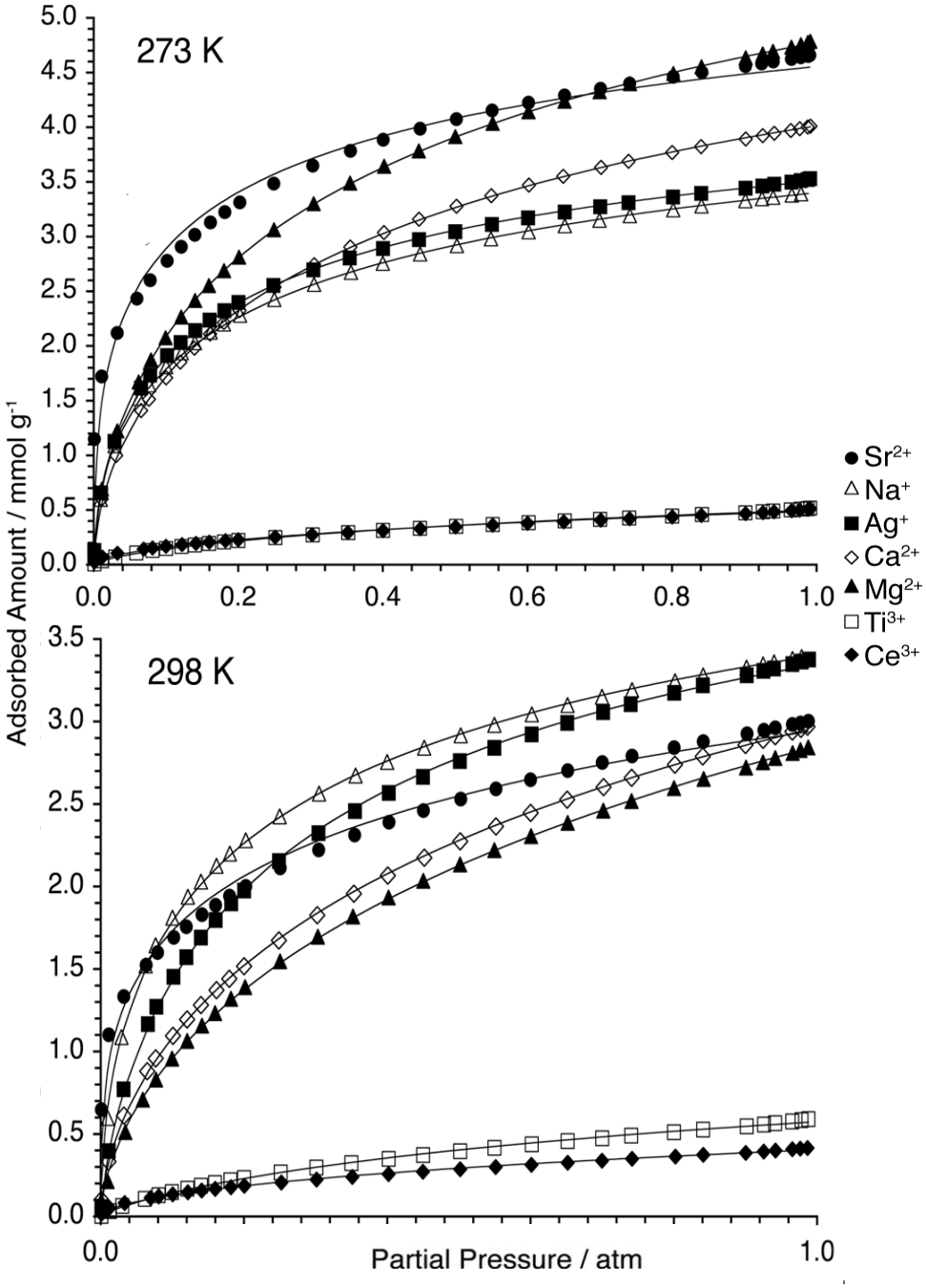

Figure 3-1. Adsorption isotherms of CO_2 on M^{n+}-SAPO-34 at 273 and 298 K. Solid lines represent Langmuir-Freundlich fits.

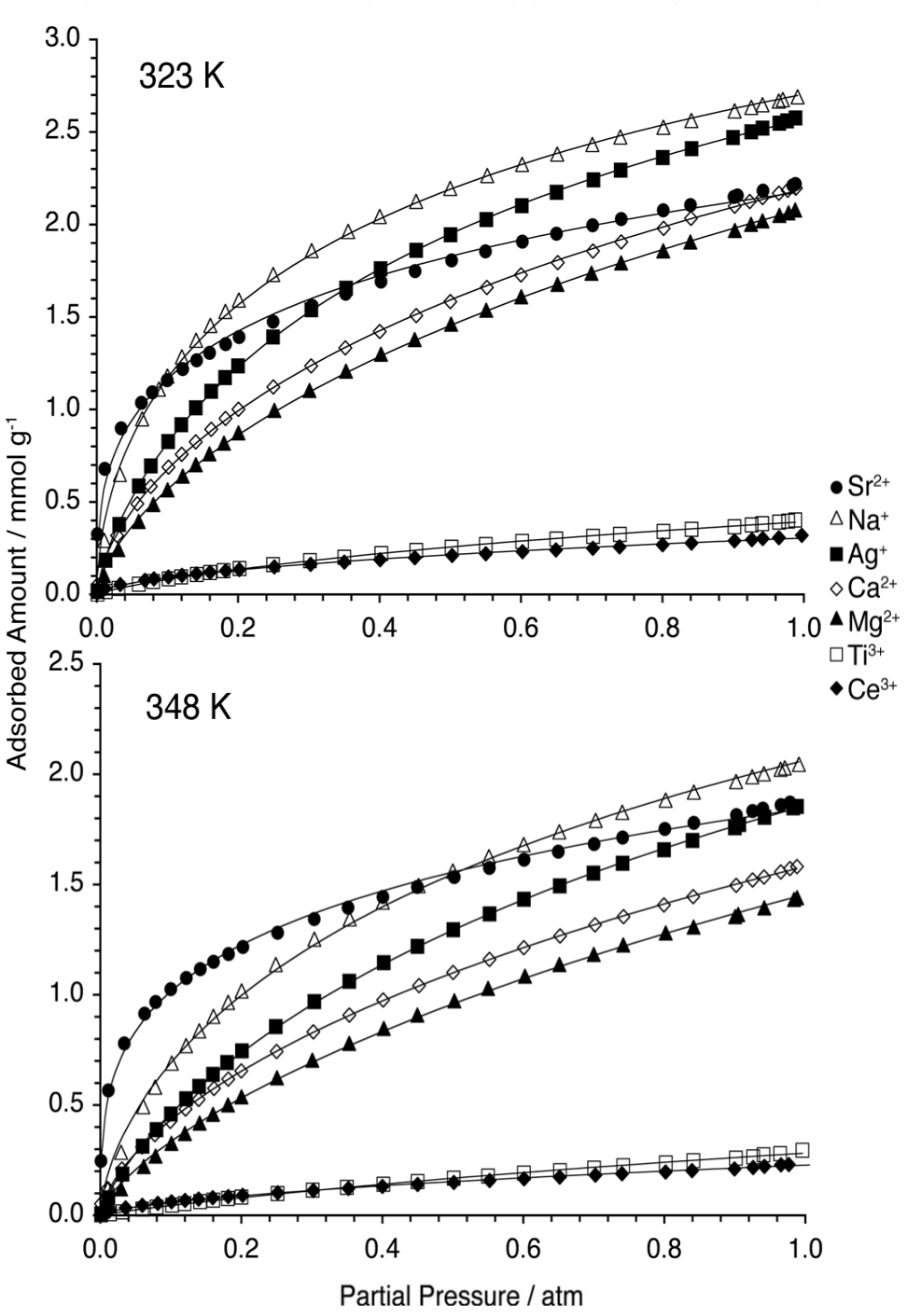

Figure 3-2. Adsorption isotherms of CO_2 on M^{n+}-SAPO-34 at 323 and 348 K. Solid lines represent Langmuir-Freundlich fits.

Table 3-2 summarizes the heterogeneity factor results for all the sorbents at different temperatures. In general, the heterogeneity of the system with respect to carbon dioxide uptake changed as a function of temperature. This should be expected in nanoporous materials frameworks that usually have more sites (i.e., coordination states) available for the charge-balancing cations to occupy (Figure 2-1). The distribution of cationic species on the sites depends on the temperature of heat-treatment, the nature of the species, and the degree of hydration.[38-41]

Table 3-2. Heterogeneity Factor (n_h) for Adsorption of CO_2 in M^{n+}-SAPO-34 Sorbents at Different Temperatures

temp. (K)	Na^+-SAPO-34	Ag^+-SAPO-34	Mg^{2+}-SAPO-34	Ca^{2+}-SAPO-34	Sr^{2+}-SAPO-34	Ti^{3+}-SAPO-34	Ce^{3+}-SAPO-34
273	1.94	1.65	1.64	1.65	2.24	1.44	1.76
298	1.82	1.38	1.66	1.67	2.84	1.26	1.79
323	1.76	1.35	1.51	1.59	2.78	1.24	1.73
348	1.59	1.30	1.42	1.55	3.05	1.12	1.59

Before proceeding further with the discussion, it is very important to note that all the sorbents exhibited fully reversible adsorption-desorption paths (please see Appendix E for example data). This is critical for regeneration cycles, since all the working sorption capacity could be regained by simple engineering means.

3.4.1.a Ag^{+}-SAPO-34. Usually, an increase in cation size of monovalent species results in a decrease of the adsorption capacity in some zeolites.[35] In terms of sorption characteristics, at 273 and 298 K the CO_2 adsorption amounts in the Ag(I) exchanged materials are comparable to those obtained for Na^{+}-SAPO-34. However, as the process temperature is increased, a decrease in the adsorbed amount was observed when compared also to the Na^{+}-sorbent at the same conditions (see Figures 3-1 and 3-2). Sorbents with certain transition metal cations are know to form π-complexation bonds with some sorbates (e.g. N_2, CO),[25] but the carbon dioxide monodentate adsorption mechanism will probably avoid this kind of complexation,[42] resulting in a decrease in interaction with the sorbate at low pressure ranges when compared with other sorbent that exhibit the same adsorption capacity at higher pressures.

3.4.1.b Mg^{2+}-SAPO-34. With the exception of the 273 K test results, this material adsorbed less carbon dioxide at 1 atm when compared to the unmodified material. Based on the observed behavior, is plausible to state that Mg^{2+} cations offer partial blocking of the pore window, affecting the entrance of the sorbate molecules into the crystal framework.[1] It should be mentioned that at 273 K, this material produced an adsorbed amount at 1 atm comparable to the of Sr^{2+}-SAPO-34 sorbent. The CO_2 adsorption in strontium-exchanged materials will be discussed shortly.

3.4.1.c Ca^{2+}-SAPO-34. At 273 K, this sorbent adsorbed more carbon dioxide than Na^{+} and Ag^{+} SAPO-34 materials, respectively. At 298 and 323 K, the carbon dioxide adsorbed amounts (~ 1 atm) are only comparable to those obtained with Sr^{2+}-SAPO-34

(see Figures 3-1 and 3-2). The Ca^{2+}-SAPO-34 material showed heterogeneity factors comparable to those obtained for Mg^{2+}-SAPO-34. With this behavior trend, one could state that Mg^{2+} and Ca^{2+} cations occupied similar sites (SII', see Figure 2-1) within the Chabazite framework.

3.4.1.d Sr^{2+}-SAPO-34. The shape of the adsorption isotherms in this material is sound evidence of stronger sorbent-sorbate interactions. Particularly when compared to the other M^{n+}-SAPO-34 formulations at the low-pressure range (see Figure 3-3). For this sorbent, the results suggest that Sr^{2+} cations are sitting near window sites (site II'), producing strong interactions with the sorbates located within the relevant perimeter. With the exception of the 273 K test results, this material adsorbed less carbon dioxide at 1 atm when compared to Na^{+}-SAPO-34. It is plausible to state that at 273 K, divalent cations are more exposed to interactions with the sorbate. As seen in Figure 3-3, at 298 K and a partial pressure of ca. 10^{-3} atm (or 900 ppm), the Sr^{2+}-SAPO-34 sorbent adsorbs approximately 0.65 mmoles of CO_2 per gram of material. This translates to a sorption capacity of about 2.8-wt%, which is almost twice the observed capacity in 5A-type zeolites at similar conditions.[2] The strong interactions presented by this material towards CO_2 are without a doubt ideal for adsorption applications where traces of carbon dioxide are needed to be removed from a gas mixture (i.e., ultra purification). An additional discussion for the Sr^{2+}-SAPO-34 sorption performance will be presented shortly.

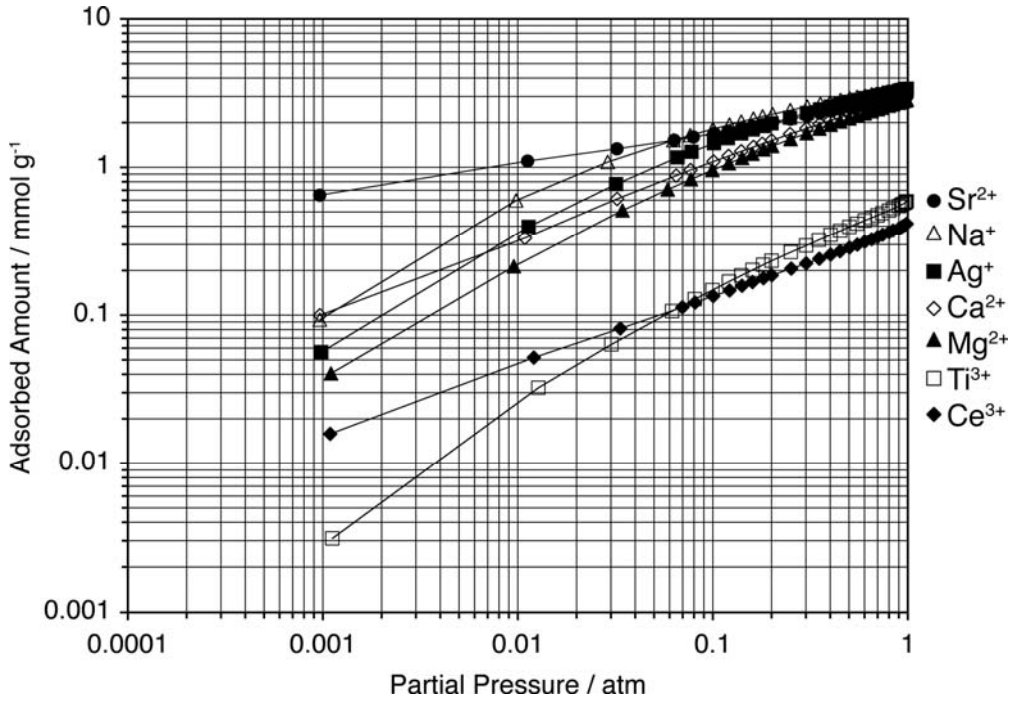

Figure 3-3. Adsorption isotherms (log-log scale) of CO_2 on M^{n+}-SAPO-34 at 298 K.

3.4.1.e Ce^{3+}-SAPO-34 and Ti^{3+}-SAPO-34. For these sorbents, the CO_2 adsorption capacities were much lower than those obtained with the other M^{n+}-SAPO-34 (see Figures 3-1 and 3-2). It is plausible that both Ce^{3+} and Ti^{3+} species occupy sites near the center of the cages (SIII), where they can balance three Al^{3+} tetrahedral negative charges on the framework at the same time. This coordination condition, together with the considerable relative large size of the trivalent cations, should result in pore blocking.

3.4.2 Fractional Uptake and Diffusion Time Constant. Figure 3-4 shows fractional uptake data for the M^{n+}-SAPO-34 sorbents that displayed the best CO_2 overall adsorption capacity (Na^+, Ag^+ and Sr^{2+}). The uptake data were gathered at an arbitrary constant loading condition (e.g., 1.8 mmol/g). It should be mentioned that the diffusion time constants estimated for present sorbates (i.e. N_2, CH_4, CO_2) and sorbents compare very

well with those available in the literature for other sorbents (i.e. Type-A zeolite, Clinoptilolite, CMS).[13, 43, 44] These results suggest that carbon dioxide molecules diffuse equally faster and independently of the nature of these metal cations. Rivera-Ramos and Hernández-Maldonado[1] reported that the estimated pore size for Sr^{2+}-SAPO-34 was smaller than the one obtained for the monovalent sorbents suggesting that the Sr^{2+} cations are sitting near window sites (Sites II and II'). We understand that the strong interaction result between the Sr^{2+} cations and the sorbent molecules are sufficiently high to break any steric effect that the partial blocking of the pore window by the cations can created. Hence, the extraframework species under discussion are indeed not completely blocking the pore window. Diffusion time constants at near zero coverage are summarized in Table 3-3.

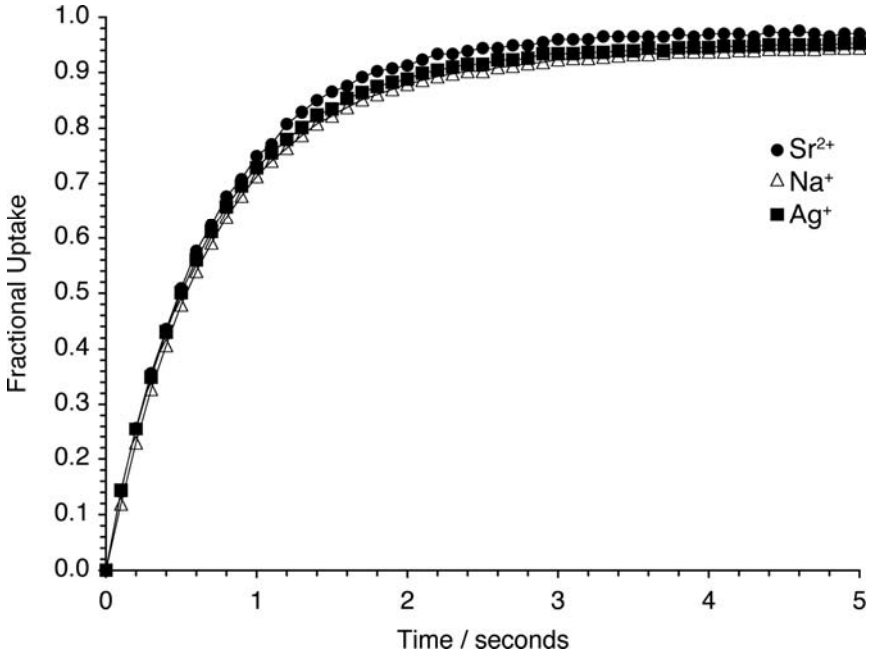

Figure 3-4. Carbon dioxide uptake on M^{n+}-SAPO-34 at 298K.

Table 3-3. Diffusion Time Constant at Near Zero Coverage for Carbon Dioxide and Methane in M^{n+}-SAPO-34 Materials

sorbent	D_o (1/s)	
	CO_2	CH_4
Na^+-SAPO-34	0.0065	0.0214
Ag^+-SAPO-34	0.0078	0.0274
Sr^{2+}-SAPO-34	0.0056	0.0216

3.4.3 Isosteric Heat of Adsorption (ΔH_{ads}) in M^{n+}-SAPO-34. Estimates of isosteric heat of adsorption for all M^{n+}-SAPO-34 materials correlated to physical and reversible adsorption (Figure 3-5). The values varied according to the type of cation exchanged into the SAPO-34 framework and the average was around 30 kJ/mol. Our Na^+-SAPO-34 results are in good agreement with calorimeter analysis previously reported by Dunne and co-workers for the adsorption of CO_2 in NaX zeolite.[15] In addition, many of the adsorbents displayed little degree of heterogeneity, which correlated well with the results shown in Table 3-2. The only exception was the Sr(II) exchanged material.

From Figure 3-5 it is evident that the Sr^{2+}-SAPO-34 sorbents have higher interactions with CO_2 when compared to the other M^{n+}-SAPO-34 materials. The variation of the isosteric heats as a function of adsorption loading was also very notable for this sorbent (see Figure 3-5). This is in good agreement with the heterogeneity factors (largest *n* factor) estimated for this material (see Table 3-2). Noting that the maximum heat of adsorption occurs at 0.65 mmol/g (Figure 3-5) and taking into consideration that the

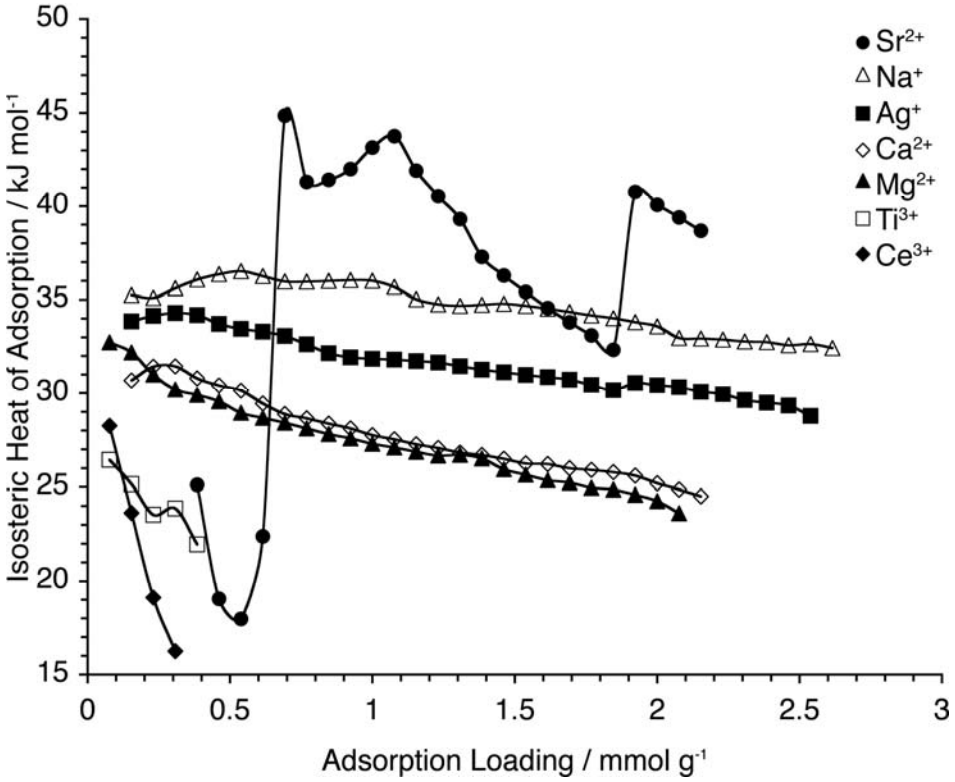

Figure 3-5. Isosteric heat of adsorption for CO_2 on M^{n+}-SAPO-34.

sorbent unit cell composition is given by $|Na^{+}_{0.31}\ Sr^{2+}_{1.05}\ H^{+}_{2.77}|\ [Si_{4.34}\ Al_{18.42}\ P_{13.24}\ O_{72}]$ (as reported by Rivera-Ramos and Hernández-Maldonado),[1] then there are one CO_2 molecule adsorbed per Sr^{2+} cation at this point. The adsorption heat maximum observed for the Sr^{+2} sorbent should be a result of the quadrupole moment interaction between the sorbate and the electric field generated by the cations on the SAPO-34 surface. We understand that once the carbon dioxide molecules have interacted with all the available Sr^{2+} cations, the sorbate continues to interact with the Na^{+} cations that are still present in the material. This corresponds to the subsequent energy decrease at higher loadings (Figure 3-5). The average isosteric heat of adsorption in the 1-2 mmol/g loading region

matches well with those observed for Na^+-SAPO-34. Additional deviations in the heat of adsorption are probably due to sorbate-sorbate interactions within the cages of the structure.[7]

It should be mentioned at this point of the discussion that the Sr^{2+}-SAPO-34 sorption capacity could be further improved if one manages to introduce additional extraframework Sr^{2+} cations. As previously mentioned, the observed unit cell composition shows that Na^+ cations are still present in the structure.

3.4.4 CH_4, CO_2, H_2, N_2 and O_2 Pure Component Equilibrium Adsorption in Na^+-SAPO-34, Ag^+-SAPO-34 and Sr^{2+}-SAPO-34. Although typical natural gas mixtures consist mainly of CH_4, these also include significant quantities of CO_2, N_2 and traces of O_2 and H_2. The portion of impurities gases is usually less than 5% of the total, but there are some reservoirs where the share can be much larger.[5] To study the potential of the M^{n+}-SAPO-34 sorbents for natural gas purification, it was necessary to consider the adsorption behavior of all of these sorbates in the studied sorbents. Figures 3-6 through 3-8 show the pure component adsorption isotherms for all of the aforementioned gases in Na^+-SAPO-34, Ag^+-SAPO-34 and Sr^{2+}-SAPO-34, respectively. The adsorption data of methane and nitrogen was obtained from Rivera-Ramos and Hernández-Maldonado.[1] In general, the sorbents displayed a remarkable selectivity towards CO_2 at all partial pressures. However, to better explain the observed selectivity behavior it is necessary to focus on the contributions to the surface potential or adsorption energy.

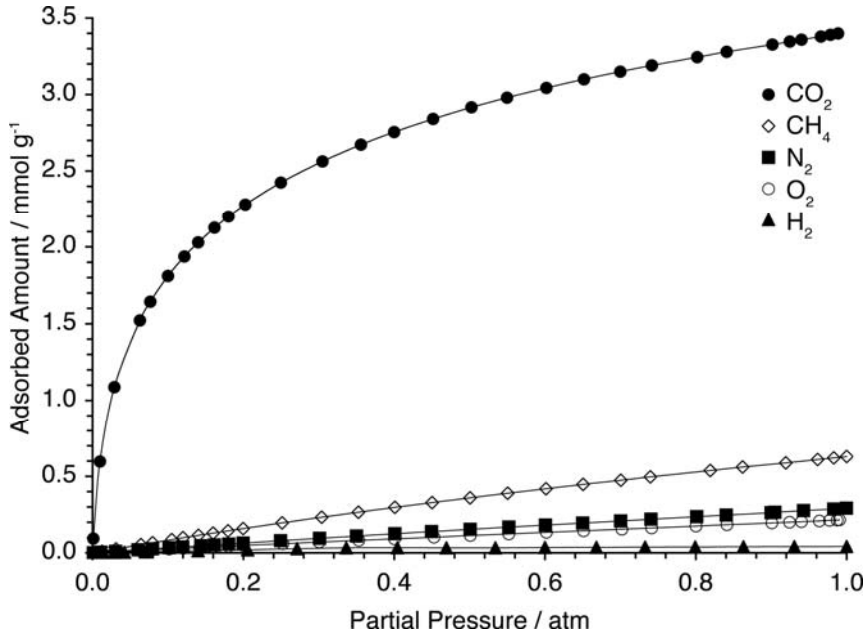

Figure 3-6. Pure component adsorption isotherms for CO_2, CH_4, H_2, N_2 and O_2 on Na^+-SAPO-34 at 298 K.

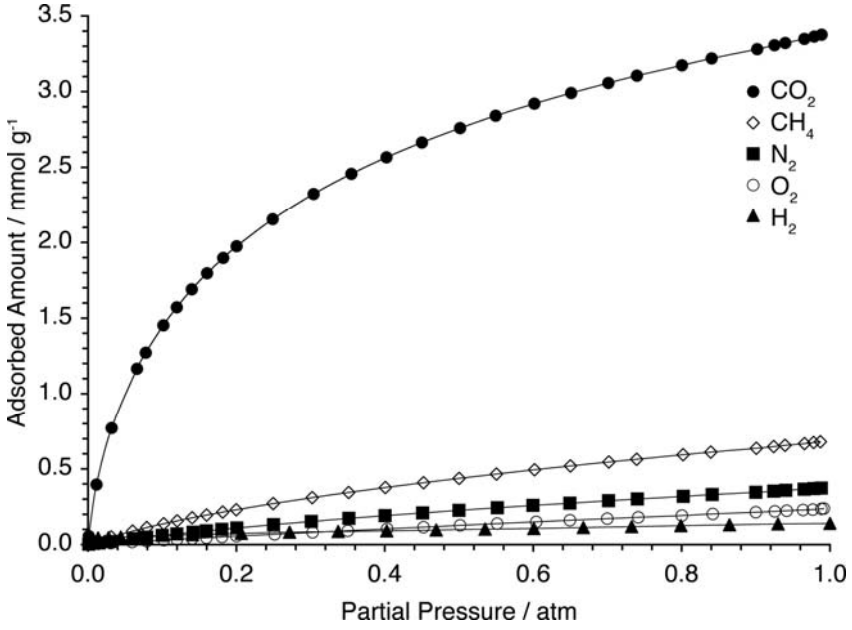

Figure 3-7.Pure component adsorption isotherms for CO_2, CH_4, H_2, N_2 and O_2 on Ag^+-SAPO-34 at 298 K.

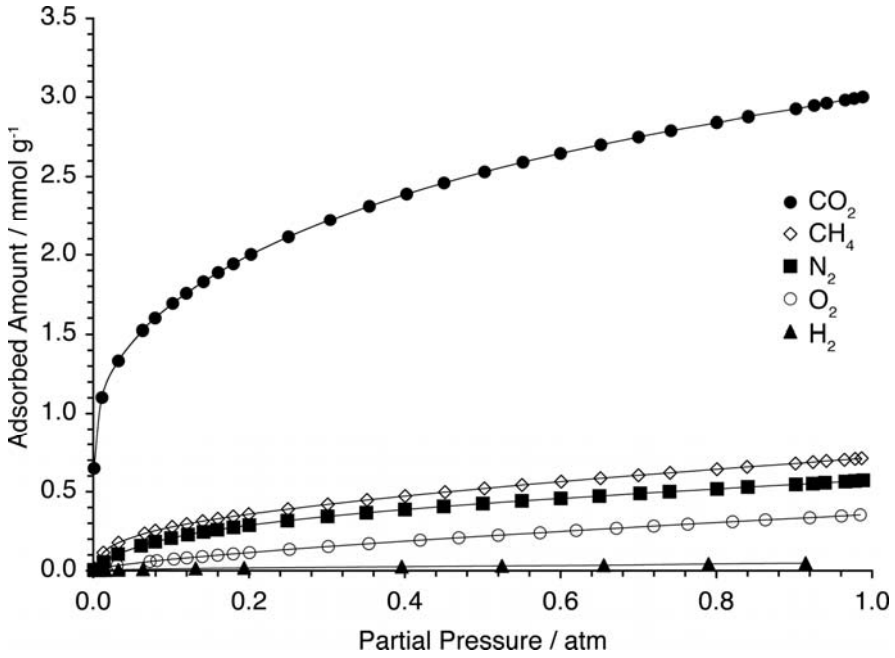

Figure 3-8. Pure component adsorption isotherms for CO_2, CH_4, H_2, N_2 and O_2 on Sr^{2+}-SAPO-34 at 298 K.

The shape of the isotherms is an immediate reflection of the sorbate-sorbent interactions or the heat of adsorption. For physisorption level interactions, the heat of adsorption can be related to several components. These include dispersion and repulsion energies (nonspecific) and additional components attributed to electrostatic interactions (specific). Nonspecific interactions (ϕ_D and ϕ_R) strongly depend on the polarizability, α. Although the sorbates magnetic susceptibility also affects these interactions, the contribution is not as strong as the one provided by the polarizability.[25] The kinetic diameters of CO_2, CH_4 and N_2 are 3.30, 3.80 and 3.64Å, respectively. Meanwhile, the polarizabilities (α) are 29.1×10^{-25}, 25×10^{-25} and 17.6×10^{-25} cm^3, respectively.[24, 25] A simple inspection of these values will lead to the conclusion that CO_2 will have a slight advantage in the nonspecific interactions region. Therefore, this type of interaction contribution does not

offer a satisfactory explanation for the considerable selectivity exhibited by the sorbents (Figures 3-6 through 3-8) and it is necessary to consider the specific contributions.

Specific contributions (ϕ_{Ind}, $\phi_{F\mu}$ and ϕ_{FQ}) arise from charges on the solid surface. However, since CO_2, CH_4 and N_2 do no have a permanent dipole, $\phi_{F\mu}$=0. CO_2 has a strong quadrupole moment (-4.3×10^{-26} $erg^{1/2}$ $cm^{5/2}$)[25] and should make a significant contribution to the total interaction potential or heat of adsorption.[10] In fact, the CO_2 quadrupole moment is 3 times greater than that of N_2. Since CH_4 molecules do not exhibit a quadrupole moment, the observed high selectivity towards CO_2 can only be attributed to its relatively strong quadrupole moment interaction with the cation electric field. Such interaction should also provide the ability to break steric barriers, if any, that the small channels of the framework could generate. Amore specific description of the dependence that holds the nonspecific and specific interactions are presented in Chapter 2 section 2.4.4.

3.4.5 VPSA for CO_2 and CH_4 Separation: Simulation Results. The objective of this section is to demonstrate the theoretical potential of the sorbents to achieve the desire separation of a binary system using a rather simple transient simulation method. Since obtaining empirical data on multi-component adsorption is beyond the scope of this work, a simple mathematical modeling approach for the CO_2/CH_4 separation was carried out for the most promising studied sorbents (Ag^+-SAPO-34, Na^+-SAPO-34 and Sr^{2+}-SAPO-34).

The diffusion time constants at near zero coverage and the isotherm parameters values used for the simulation are summarized in Tables 3-3 and 3-4, respectively. VPSA cycle parameters are shown in Table 3-5. The calculations involving the Sr^{2+}-SAPO-34 sorbent were carried out using a Runge-Kutta routine due to the strong non-linearity that produces the observed heterogeneity factor. The NDFs method was used instead for the Na^{+}-SAPO-34 and Ag^{+}-SAPO-34 cases. Table 6 shows a summary of the simulation results. In general, the results are in good agreement with the pure component adsorption isotherm data behavior described in the previous sections. Sr^{2+}-SAPO-34 required the smaller number of steps to obtain the achieve product purity and presented an acceptable adsorbed phase ratio. The sorbents exhibiting lower CO_2 interactions at low pressures (i.e., Na^{+}-SAPO-34 and Ag^{+}-SAPO-34) required additional VPSA step to achieve the required product purity. Based on these results, all the studied materials are certainly capable sorbents for this kind of separation. However, Sr^{2+}-SAPO-34 is without a doubt the promising candidate due to the strong CO_2 sorbate-sorbent interactions.

Table 3-4. Sips Isotherm Parameters for Carbon Dioxide and Methane in M^{n+}-SAPO-34 Materials at 298 K

sorbent	q_{sat} (mmol/g)		K_{LF} (1/atm)		n	
	CO_2	CH_4	CO_2	CH_4	CO_2	CH_4
Na^{+}-SAPO-34	5.264	2.127	2.989	0.412	1.817	1.000
Ag^{+}-SAPO-34	4.879	1.654	2.951	0.660	1.384	1.104
Sr^{2+}-SAPO-34	6.707	2.003	0.498	1.893	2.839	1.893

Table 3-5. Parameters for VPSA simulations

parameters	value
feed pressure	1 atm
temperature (T)	298 K
particle density[2] ($\rho_{particle}$)	1.06×10^3 kg/m^3
bed void (ε_{bed})	0.348
diffusion volume[45] (D_v)	26.7 (CO_2); 25.14 (CH_4)
particle porosity[2] ($\varepsilon_{particle}$)	0.38
particle tortuosity[2] ($\tau_{particle}$)	4.5
particle radius (R_p)	0.6×10^{-6} m

Table 3-6. VPSA Simulation Results for Purification of CH_4

	Feed Composition (CO_2/CH_4) (mole %)					
	20 / 80		10 / 90		5 / 95	
sorbent	steps required	adsorbed phase ratio (CO_2/CH_4)	steps required	adsorbed phase ratio (CO_2/CH_4)	steps required	adsorbed phase ratio (CO_2/CH_4)
Na^+-SAPO-34	22	0.0291	17	0.0181	4	0.2247
Ag^+-SAPO-34	34	0.0527	33	0.0259	32	0.0130
Sr^{2+}-SAPO-34	6	0.4726	4	0.3619	3	0.2810

* Adsorption steps required (ca. 1 s each) to achieve 99.9999% CH_4 purity.

3.5 Conclusions

The present work has shown that ion-exchanged M^{n+}-SAPO-34 materials could be promising sorbents for the selective removal of CO_2 at temperatures and pressures that approach ambient conditions. In terms of overall adsorption performance the exchanged materials exhibited the following trend: $Ce^{3+}<Ti^{3+}<Mg^{2+}<Ca^{2+}<Ag^{+}<Na^{+}<Sr^{2+}$. Strontium(II) exchanged SAPO-34 was by far the best sorbent in the low-pressure region.

The isosteric heat of adsorption data suggested that all the exchanged Sr^{2+} species were exposed to the Chabazite cages, but did not provide transport resistance or pore blocking. Uptake data indicated that the adsorption kinetics for CO_2 in the Ag^+, Na^+, and Sr^{2+} exchanged materials were fast, evidencing again the absence of transport resistance within the pore channels. Binary component adsorption (CO_2/CH_4) simulation data corroborated that, among the sorbents studied, the strontium(II) exchanged ones were by far superior. Finally, it should be mentioned that all the sorbents studied can be fully regenerated by simple engineering means since the adsorption interactions were in the physisorption range.

3.6 References

[1] Rivera-Ramos, M. E.; Hernandez-Maldonado, A. J., Adsorption of N_2 and CH_4 by Ion-Exchanged Silicoaluminophosphate Nanoporous Sorbents: Interaction with Monovalent, Divalent, and Trivalent Cations. *Ind. Eng. Chem. Res.* **2007,** *46*, (14), 4991-5002.

[2] Ko, D.; Siriwardane, R.; Biegler, L. T., Optimization of Pressure Swing Adsorption and Fractionated Vacuum Pressure Swing Adsorption Processes for CO_2 Capture. *Ind. Eng. Chem. Res.* **2005,** *44*, (21), 8084-8094.

[3] Li, S.; Falconer, J. L.; Noble, R. D., SAPO-34 Membranes for CO_2/CH_4 Separation. *J. Membr. Sci* **2004,** *241*, 121.

[4] Baker, R. W., Future Directions of Membrane Gas Separation Technology. *Ind. Eng. Chem. Res.* **2002,** *41*, 1393.

[5] *Emissions of Greenhouse Gases in the United States-DOE/EIA-0573*; 1936-4512; Energy Information Administration, Office of Energy Markets and End Use, U.S. Dept. of Energy: Washington, D.C., 1994.

[6] Poshusta, J. C.; Tuan, V. A.; Pape, E. A.; Noble, R. D.; Falconer, J. L., Separation of Light Gas Mixtures Using SAPO-34 Membranes. *AIChE J.* **2000,** *46*, (4), 779-789.

[7] Breck, D. W., *Zeolite Molecular Sieves*. Wiley: New York, 1973.

[8] Mulloth, L. M.; Finn, J. E. *Carbon Dioxide Adsorption on a 5A Zeolite Designed for CO_2 Removal in Spacecraft Cabins*; NASA/TM-1998-208752; NASA Ames Research Center: 1998; pp 1-9.

[9] Ko, D.; Siriwardane, R.; Biegler, L. T., Optimization of a Pressure-Swing Adsorption Process Using Zeolite 13X for CO_2 Sequestration. *Ind. Eng. Chem. Res.* **2003,** *42*, (2), 339-348.

[10] Aguilar-Armenta, G.; Hernandez-Ramirez, G.; Flores-Loyola, E.; Ugarte-Castaneda, A.; Silva-Gonzalez, R.; Tabares-Munoz, C.; Jimenez-Lopez, A.; Rodriguez-Castellon, E., Adsorption Kinetics of CO_2, O_2, N_2, and CH_4 in Cation-Exchanged Clinoptilolite. *J. Phys. Chem. B* **2001,** *105*, (7), 1313-1319.

[11] Liu, X.; Li, J.; Zhou, L.; Huang, D.; Zhou, Y., Adsorption of CO_2, CH_4 and N_2 on Ordered Mesoporous Silica Molecular Sieve. *Chem. Phys. Lett.* **2005,** *415*, 198-201.

[12] Liu, X.; Zhou, L.; Fu, X.; Sun, Y.; Su, W.; Zhou, Y., Adsorption and Regeneration Study of the Mesoporous Adsorbent SBA-15 Adapted to the Capture/Separation of CO_2 and CH_4. *Chem. Eng. Sci.* **2007,** *62*, 1101-1110.

[13] Kikkinides, E. S.; Yang, R. T.; Cho, S. H., Concentration and Recovery of CO_2 from Flue-Gas by Pressure Swing Adsorption. *Ind. Eng. Chem. Res.* **1993,** *32*, (11), 2714-2720.

[14] Lovallo, M. C.; Gouzinis, A.; Tsapatsis, M., Synthesis and Characterization of Oriented MFI Membranes Prepared by Secondary Growth. *AIChE J.* **1998,** *44*, (8), 1903-1913.

[15] Dunne, J. A.; Mariwals, R.; Rao, M.; Sircar, S.; Gorte, R. J.; Myers, A. L., Calorimetric Heats of Adsorption and Adsorption Isotherms: 1. O_2, N_2, Ar, CO_2, CH_4, C_2H_6 and SF_6 on Silicalite. *Langmuir* **1996,** *12*, (24), 5888-5895.

[16] Li, S. G.; Martinek, J. G.; Falconer, J. L.; Noble, R. D.; Gardner, T. Q., High-Pressure CO_2/CH_4 Separation using SAPO-34 Membranes. *Ind. Eng. Chem. Res.* **2005,** *44*, (9), 3220-3228.

[17] Li, S.; Falconer, J. L.; Noble, R. D., Improved SAPO-34 Membranes for CO_2/CH_4 Separations. *Adv. Mater.* **2006,** *18*, (19), 2601-2603.

[18] Lok, B. M.; Messina, C. A.; Patton, R. L.; Gajek, R. T.; Cannan, T. R.; Flanigen, E. M. Crystalline Silicoaluminophosphates. US Patent 4,440,871, 1984.

[19] Szostak, R., *Molecular Sieves : Principles of Synthesis and Identification*. Van Nostrand Reinhold: New York, 1989.

[20] Barros, M. A. S. D.; Araujo, I. F.; Arroyo, P. A.; Sousa-Aguiar, E. F.; Tavares, C. R. G., Multicomponent Ion Exchange Isotherms in NaX Zeolite. *Lat. Am. Appl. Res.* **2003,** *33*, (3), 339-344.

[21] Ju, W. S.; Matsuoka, M.; Iino, K.; Yamashita, H.; Anpo, M., The Local Structures of Silver(I) Ion Catalysts Anchored within Zeolite Cavities and their

Photocatalytic Reactivities for the Elimination of N_2O into N_2 and O_2. *J. Phys. Chem. B* **2004,** *108*, (7), 2128-2133.

[22] Hutson, N. D.; Reisner, B. A.; Yang, R. T.; Toby, B. H., Silver Ion-Exchanged Zeolites Y, X, and Low-Silica X: Observations of Thermally Induced Cation/Cluster Migration and the Resulting Effects on the Equilibrium Adsorption of Nitrogen. *Chem. Mat.* **2000,** *12*, (10), 3020-3031.

[23] Guan, J.; Zeng, R.; Long, C.; Hu, X., Dynamic Simulation of Pressure Swing Adsorption System with the Electrical Network. *Chem. Eng. Sci.* **2005,** *60*, 4635-4645.

[24] Jayaraman, A.; Hernandez-Maldonado, A. J.; Yang, R. T.; Chinn, D.; Munson, C. L.; Mohr, D. H., Clinoptilolites for Nitrogen/Methane Separation. *Chem. Eng. Sci.* **2004,** *59*, (12), 2407-2417.

[25] Yang, R. T., *Adsorbents: Fundamentals and Applications*. Wiley: New York, 2003.

[26] Serbezov, A.; Sotirchos, S. V., Multicomponent Transport Effects in Sorbent Particles under Pressure Swing Conditions. *Ind. Eng. Chem. Res.* **1997,** *36*, 3002-3012.

[27] Do, D. D., *Adsorption Analysis: Equilibria and Kinetics*. Imperial College Press: London, 1998.

[28] Ruthven, D. M., *Principles of Adsorption and Adsorption Processes*. Wiley: New York, 1984.

[29] Hernandez-Maldonado, A. J.; Yang, R. T.; Chinn, D.; Munson, C. L., Partially Calcined Gismondine Type Silicoaluminophosphate SAPO-43: Isopropylamine

Elimination and Separation of Carbon Dioxide, Hydrogen Sulfide, and Water. *Langmuir* **2003,** *19*, (6), 2193-2200.

[30] Chen, Y. D.; Yang, R. T., Concentration Dependence of Surface Diffusion and Zeolitic Diffusion. *AIChE J.* **1991,** *37*, (10), 1579-1582.

[31] Shampine, L. F.; Reichelt, M. W., The MATLAB ODE Suite. *SIAM J. Sci. Compu.* **1997,** *18*, 1-22.

[32] Shampine, L. F.; Reichelt, M. W.; Kierzenka, J. A., Solving Index-1 DAEs in MATLAB and Simulink. *SIAM Rev.* **1999,** *41*, 538-552.

[33] Forsythe, G.; M., M.; C., M., *Computer Methods for Mathematical Computations*. Prentice-Hall: New Jersey, 1977.

[34] Kahaner, D.; Moler, C.; Nash, S., *Numerical Methods and Software*. Prentice-Hall: New Jersey, 1989.

[35] Peter, S. A.; Sebastian, J.; Jasra, R. V., Adsorption of Nitrogen, Oxygen, and Argon in Mono-, Di-, and Trivalent Cation-Exchanged Zeolite Mordenite. *Ind. Eng. Chem. Res.* **2005,** *44*, (17), 6856-6864.

[36] Mirajkar, S. P.; Thangaraj, A.; Shiralkar, V. P., Sorption Properties of Titanium Silicate Molecular-Sieves. *J. Phys. Chem.* **1992,** *96*, (7), 3073-3079.

[37] Reddy, K. S. N.; Eapen, M. J.; Soni, H. S.; Shiralkar, V. P., Sorption Properties of Cation-Exchanged Beta-Zeolites. *J. Phys. Chem.* **1992,** *96*, (20), 7923-7928.

[38] Barrer, R. M., *Zeolites and Clay Minerals as Sorbents and Molecular Sieves*. Academic Press: London ; New York, 1978.

[39] Vandun, J. J.; Mortier, W. J., Influence of the Temperature on the Cation Distribution in Dehydrated and Hydrated SrY Zeolites. *Zeolites* **1987,** *7*, (6), 528-534.

[40] Vandun, J. J.; Dhaeze, K.; Mortier, W. J., Temperature-Dependent Cation Distribution in Zeolites: 2. Dehydrated $Na_{13}HY$, $Na_{23}HY$, $Na_{42}HY$, $Na_{54}HY$, $Ca_{15}HY$, and $Sr_{27}Y$. *J. Phys. Chem.* **1988,** *92*, (23), 6747-6754.

[41] Vandun, J. J.; Mortier, W. J., Temperature-Dependent Cation Distribution in Zeolites: 1. A Statistical Thermodynamical Model. *J. Phys. Chem.* **1988,** *92*, (23), 6740-6746.

[42] Sodupe, M.; Branchadell, V.; Rosi, M.; Bauschlicher, C. W. J., Theoretical Study of M+-CO_2 and OM+CO Systems for First Transition Row Metal Atoms. *J. Phys. Chem A* **1997,** *101*, 7854-7859.

[43] Ruthven, D. M.; Xu, Z., Diffusion of Oxygen and Nitrogen in 5A Zeolite Crystal and Commercial 5A Pellets. *Chem. Eng. Sci.* **1993,** *48*, 3307.

[44] Jayaraman, A.; Yang, R. T.; Chinn, D.; Munson, C. L., Tailored Clinoptilolites for Nitrogen/Methane Separation. *Ind. Eng. Chem. Res.* **2005,** *44*, 5184.

[45] Taylor, R.; Krishna, R., *Multicomponent Mass Transfer*. Wiley: New York, 1993.

Chapter 4

Na^+-SAPO-34 Diffusion Time Constants and Particle Size Distribution Dependence

As described in Chapter 2, the observed rate of adsorption data deviates considerably from the prediction of a customary simple solution of a diffusion phenomenological model for solid spherical particles. On the basis of the discussion so far, it is evident that assuming a mean equivalent spherical shape particle characteristic length is a poor approximation for crystal systems analogous to ours. In order to obtain accurate values for the diffusion time constant, it was necessary to account for crystal shape, size, and most importantly, size distribution.

4.1 Introduction

Diffusion in nanoporous sorbents has been studied for some decades.[1-4] Adsorption kinetics in a zeolite particle are described by two distinct processes: the diffusion of the molecules through the large void between microparticles and the diffusion of the molecules into the interior of the crystal pores. Due to the fast diffusion of sorbents between the microparticles, the uptake is then assumed to be controlled by the diffusion of the adsorbed molecules inside the sorbent.[3, 5, 6] For a linear isothermal system where the uptake rate is controlled by intracrystalline diffusion, generally, diffusion time constants (D/R^2) are estimated by fitting fractional uptake data (F) with the solution of a transient diffusion equation for a spherical shape particle.[2, 6-8] However, as discussed in Chapter 2, our sorbents uptake data indicate that the particle morphology and, most importantly, polydispersity, play an important role in predicting diffusion coefficients. Ruthven and co-workers have reported that the sorption curves are quite sensitive to the shape and size distribution of the zeolitic crystals.[9] In fact, zeolitic crystals are non-spherical and commercial molecular sieves contain a widely varying crystal size range.[3] The use of a mean equivalent particle characteristic length can lead to significant errors in the estimation of diffusion time constants and, therefore, the design of commercial sorption beds.

4.2 Experimental Section

4.2.1 Particle Size Distribution. Measurements of particle size were obtained by direct analysis of a scanning electron microscopy (SEM) image. Na^+-SAPO-34 SEM micrograph were obtained using a JEOL JSM-6390 following standard procedures for

low conductive samples. A distribution of particle lengths (x) was obtained via direct sampling from a micrograph. The obtained data was then fitted to recognized analytical functions describing Gaussian, lognormal and gamma distributions. The distributions *f(x)* can be represented as follows:[10]

a) *Gaussian distribution*

$$f(x;\mu,\sigma) = \frac{1}{\sigma\sqrt{2\pi}} \exp\left(-\frac{(x-\mu)^2}{2\sigma^2} \right) \qquad (4\text{-}1)$$

where μ is the mean of the distribution and σ is the standard deviation of x.

b) *Lognormal distribution*

$$f(x;\mu_l,\sigma_l) = \frac{\exp\left(-(\ln x - \mu_l)^2 / 2\sigma_l{}^2\right)}{\sigma_l\sqrt{2\pi}} \qquad (4\text{-}2)$$

where μ_l is the mean of ln x and σ_l is the standard deviation of ln x.

c) *Gamma distribution*

$$f(x;\alpha,\beta) = \frac{1}{\beta^{\alpha}\Gamma(\alpha)} x^{\alpha-1} e^{-\frac{x}{\beta}} \qquad (4\text{-}3)$$

where α and β are distribution parameters. The mean of the distribution (L_{aver}) is the product of α and β.

4.2.2 Carbon Dioxide Uptake Rates on Na^+-SAPO-34. Equilibrium isotherms and diffusion adsorption data were obtained using a static volumetric adsorption system

(Micromeritics ASAP 2020) outfitted with turbo molecular drag pumps. Gases used were CO_2 (Ultra High Purity Grade, Praxair) and He (High Purity Grade, Linde). The latter was used as a backfill gas after the sorbent activation. The inert gas was removed via ultra-high vacuum prior to adsorption tests. Na^+-SAPO-34 samples were treated in vacuum at 648 K to remove water molecules strongly bound inside the structure.[11] The temperature ramp, evacuation rate, and vacuum set used were 10 K/min, 50 mmHg/s and 20 μmHg, respectively. Carbon dioxide uptake tests were performed at 298 K. The kinetic data obtained via volumetric measurements used to determine the fractional uptakes were corrected by the equipment dead time to avoid any instability caused by the system.[12]

4.3 Results and Discussion

4.3.1 Particle Size Distribution. Figure 4-1 shows a typical SEM micrograph for Na^+-SAPO-34. Approximately 1300 crystals were directly in the complete SEM image. It is evident that polydispersity exists with crystals of several micrometers in size (between 0.1 and 2.0 μm), most of them exhibiting a cubic geometry. The particle size measurements were fitted to the Gaussian, lognormal and gamma distributions using equations 4-1, 4-2, and 4-3, respectively. Figures 4-2 through 4-4 show the fit of the different distributions to the experimental measurement. Based on the residual sum of squares, Table 4-1 show that the best fit corresponds to the gamma distribution. The residual sum of squares is the discrepancy between the experimental data and the

distribution model. The smaller the discrepancy, the better the estimation should be. Although the lognormal distribution was also found to describe the particle size distribution in a satisfactory fashion, the inclusion of polidispersity into a cubic particle shape phenomenological model was limited to the gamma distribution case. It should be mentioned that Ruthven and Loughlin successfully added a polidispersity function to a cubic particle shape diffusion model, but the size distribution was of a Gaussian type. [3] As evident in Figure 4-2, a Gaussian distribution function fails to predict the particle size here.

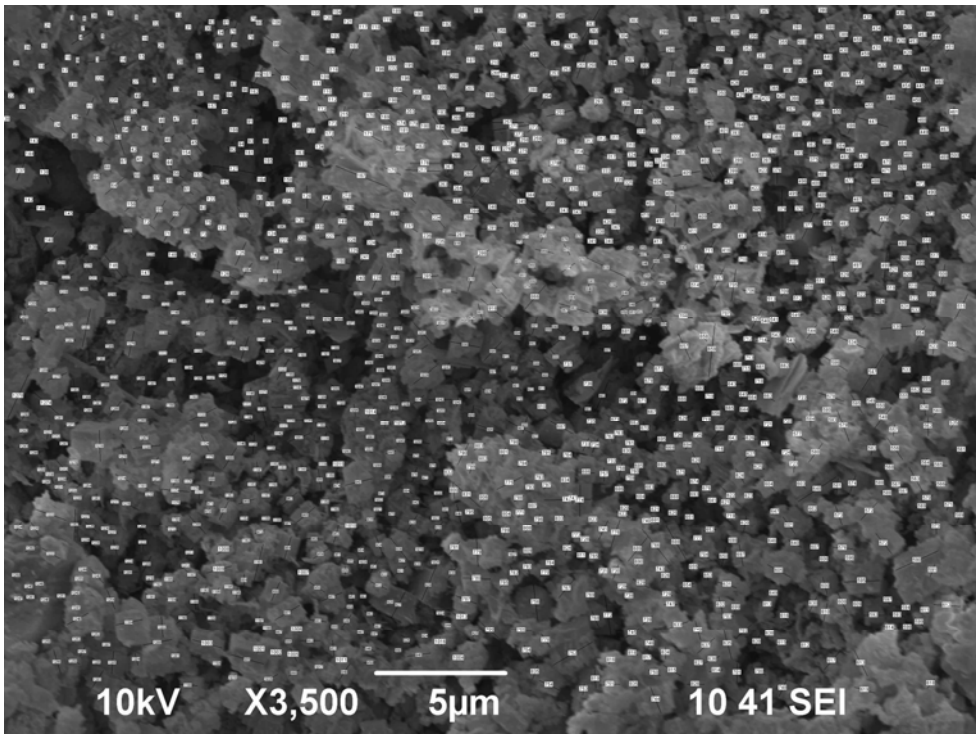

Figure 4-1. SEM micrograph of Na^{+}-SAPO-34 with particle size measurements. Included in the Figure are the particle ID numbers associated to the dimensions.

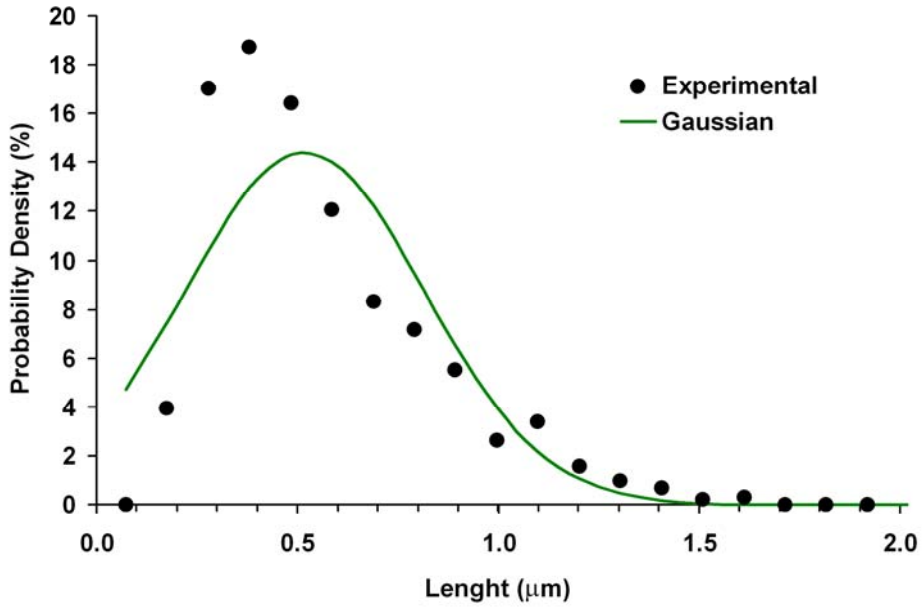

Figure 4-2. Na^{+}-SAPO-34 particle size distribution fitted with a Gaussian function.

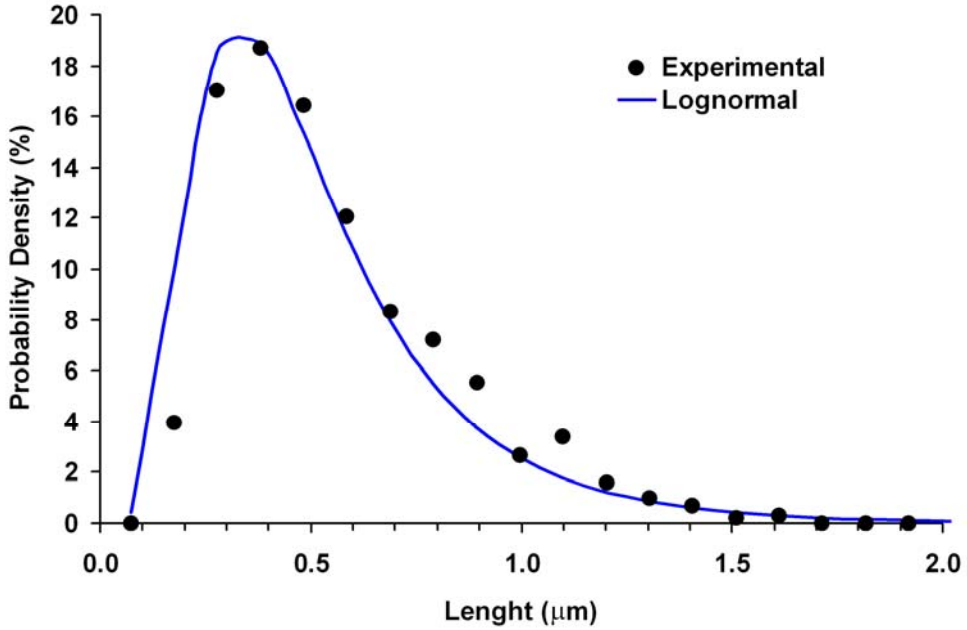

Figure 4-3. Na^{+}-SAPO-34 particle size distribution fitted with a lognormal function.

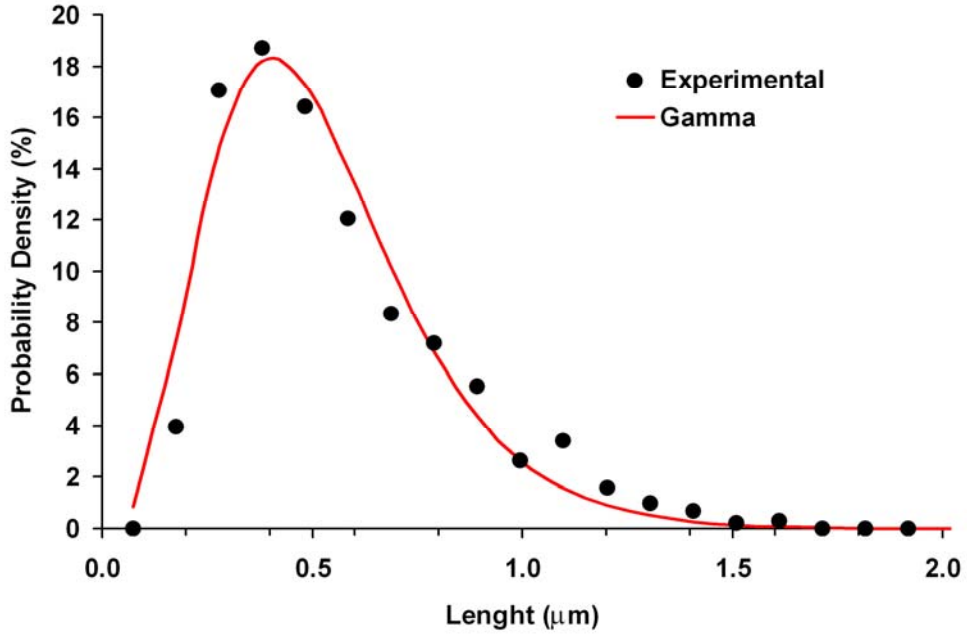

Figure 4-4. Na^+-SAPO-34 particle size distribution fitted with a gamma function.

Table 4-1. Residual Sum of Squares (RSS) for Gaussian, Lognormal and Gamma Distribution Functions

distribution function	RSS
gaussian	1.47
lognormal	0.50
gamma	0.31

4.3.2 Carbon Dioxide Uptake Rates on Na^+-SAPO-34. Figure 4-5 shows carbon dioxide uptake data on Na^+-SAPO-34 at 298K. To diminish the effect of CO_2 molecules already adsorbed inside the crystals, the data was gathered from a completely degassed state sample (with no presence of CO_2) at t = 0. The outgassed sample was suddenly exposed to a loading of 2 mmol/g of CO_2 and the uptake data gathered as a function of time. These data was either fitted with slab, spherical and cubic models paying attention to the latter parts of the sorption model curve which are quiet sensitive to the shape of the crystals. As seen in figure in Figure 4-5, the uptake data do not follow the customary phenomenological models. It should be mentioned that the aforementioned diffusion model assume a linear shape isotherm which should apply in principle only to low pressure at ambient conditions and low molecular weight sorbates.[6] To study the effect of the adsorption behavior, the nonlinearity of the isotherm effect was analyzed.

A thermodynamic correction factor in the transport diffusivity term was used to describe a non-linear isotherm behavior. D. D. Do proposed an algorithm to solve numerically the set of equations by a combination of the orthogonal and the Runge-Kutta method for the case of Langmuir isotherms.[6] However, as discussed in Chapter 3, the adsorption of CO_2 on Na^+-SAPO-34 showed a better data adjustment with the Sips Equations. The already developed algorithm was therefore modified to include the Sip Equation Isotherm (see Appendix G). In general it was found that the data obtained using the modified algorithm does not deviate from the one obtained with the models in where the linearity was assumed.

After discarding the possible effect of the isotherm on our models, it was possible to state that the deviation of the studied models from the experimental data solely corresponds to the crystal shape, size, and particle size distribution.

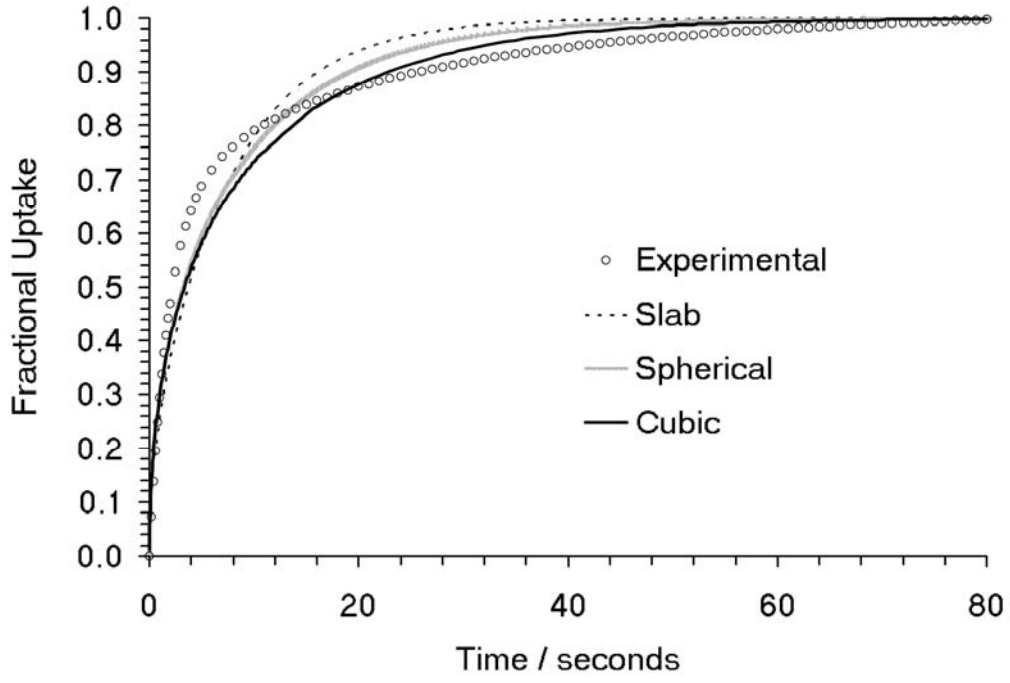

Figure 4-5. Carbon dioxide uptake on Na^+-SAPO-34 at 298K. The data was fitted with slab, spherical and cubic models.

4.3.3 Polidispersity Dependence. As discussed in Chapter 2, Na^+-SAPO-34 showed crystals of several micrometers in size, most of them exhibiting a cubic geometry. The transport model to predict the diffusivity in crystals with cubic geometry should be given by the following equation:[9]

$$F = 1 - \frac{8}{\pi^6} \sum_{n=0}^{\infty} \sum_{m=0}^{\infty} \sum_{p=0}^{\infty} \frac{\exp\left\{-4\left[\left(n+\frac{1}{2}\right)^2 + \left(m+\frac{1}{2}\right)^2 + \left(p+\frac{1}{2}\right)^2\right]\pi^2 \frac{Dt}{L^2}\right\}}{\left(n+\frac{1}{2}\right)^2 \left(m+\frac{1}{2}\right)^2 \left(p+\frac{1}{2}\right)^2} \qquad (2\text{-}10)$$

where F is the fractional uptake, D is the diffusivity constant, t is time and L is the characteristic length (see Appendix F for details of the derivation).

Introducing a gamma particle distribution of volume fraction with length in the interval x to $x+ dx$ to eq 2-10,[10] the transport model expression become:

$$F = 1 - \frac{8}{\pi^6}\sum_{n=0}^{\infty}\sum_{m=0}^{\infty}\sum_{p=0}^{\infty}\int_{x=0}^{\infty}\left(\frac{\exp\left\{-4\left[\left(n+\tfrac{1}{2}\right)^2+\left(m+\tfrac{1}{2}\right)^2+\left(p+\tfrac{1}{2}\right)^2\right]\pi^2\frac{Dt}{x^2 * L_{aver}{}^2}\right\}}{\left(n+\tfrac{1}{2}\right)^2\left(m+\tfrac{1}{2}\right)^2\left(p+\tfrac{1}{2}\right)^2} * \frac{1}{\beta^{\alpha}\Gamma(\alpha)}x^{\alpha-1}\exp\left\{-x/\beta\right\}\right)dx \quad (4\text{-}4)$$

where $x = L/L_{aver}$ and L_{aver} is the mean characteristic length of the distribution.

Figure 4-6 shows the carbon dioxide uptake on Na^+-SAPO-34 at 298K fitted with both cubic and cubic/polydispersity models. The significant difference between the model sorption curves due to the incorporation of the crystals size distribution is clearly apparent. The cubic/polydispersity model shows a better fit to the experimental data. These results confirmed that the crystal shape, and most importantly, the particle size distribution of the material are therefore required to obtain reliable diffusivity data. The effect of crystal shape and size distribution is also evident in the values of the diffusion time constant presented in Table 4-2.

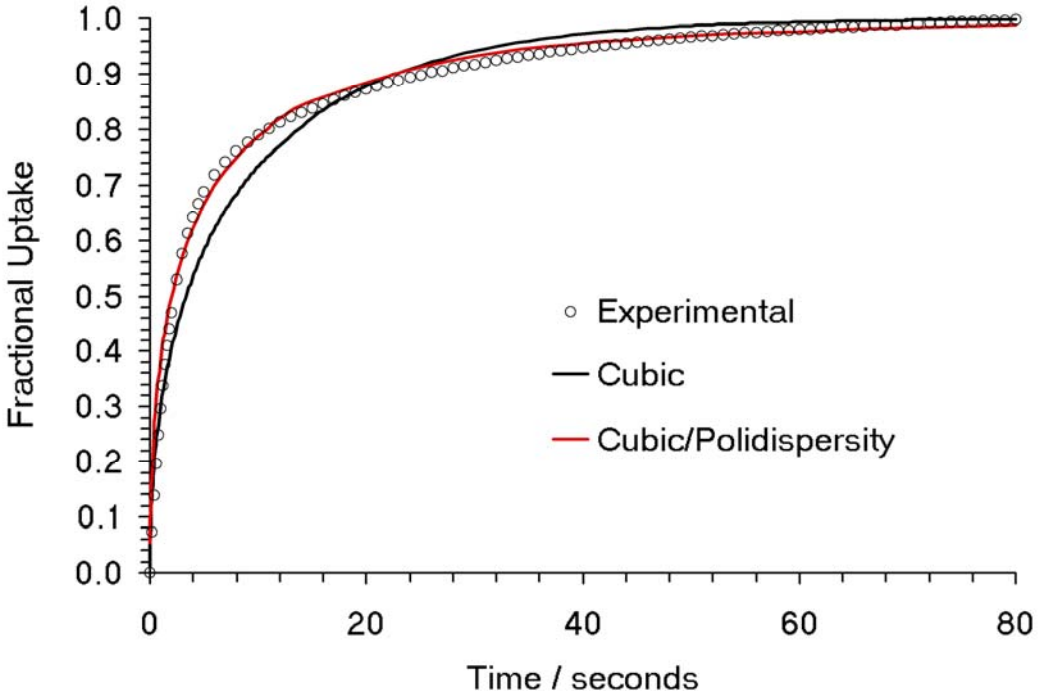

Figure 4-6. Carbon dioxide uptake on Na^+-SAPO-34 at 298K. The data was fitted with cubic and cubic/polydispersity models.

Table 4-2. Diffusion Time Constants at 0.03 atm for Carbon Dioxide in Na^+-SAPO-34 at 298 K

model	D/L^2 (1/s)
slab	0.0527
spherical	0.0096
cubic	0.0025
cubic/polydispersity	0.0008

4.4 Conclusions

The results presented in this chapter confirmed that the observed deviations between experimental uptake data and customary phenomenological models may be corrected by considering the shape and size distribution of the particles. Instead of the normally distribution proposed in the literature, the distribution that best described our material is the gamma function.

4.5 References

[1] Magalhaes, F. D.; Laurence, R. L.; Conner, W. C., Diffusion of Cyclohexane and Alkylcyclohexanes in Silicalite. *J. Phys. Chem. B* **1998,** *102*, (13), 2317-2324.

[2] Ruthven, D. M., *Principles of Adsorption and Adsorption Processes*. Wiley: New York, 1984.

[3] Ruthven, D. M.; Loughlin, K. F., The Effect of Crystallite Shape and Size Distribution on Diffusion Measurements in Molecular Sieves. *Chem. Eng. Sci.* **1971,** *26*, (5), 577-&.

[4] Yang, R. T., *Adsorbents : Fundamentals and Applications*. Wiley-Interscience: New Jersey, 2003.

[5] Yucel, H.; Ruthven, D. M., Diffusion in 4A Zeolite. *J. Chem. Soc., Faraday Trans. I* **1980,** *76*, 60-70.

[6] Do, D. D., *Adsorption Analysis: Equilibria and Kinetics*. Imperial College Press: London, 1998.

[7] Cavalcante, C. L.; Ruthven, D. M., Adsorption of Branched and Cyclic Paraffins in Silicalite .2. Kinetics. *Ind. Eng. Chem. Res.* **1995,** *34*, (1), 185-191.

[8] Hernandez-Maldonado, A. J.; Yang, R. T.; Chinn, D.; Munson, C. L., Partially Calcined Gismondine Type Silicoaluminophosphate SAPO-43: Isopropylamine Elimination and Separation of Carbon Dioxide, Hydrogen Sulfide, and Water. *Langmuir* **2003,** *19*, (6), 2193-2200.

[9] Loughlin, K. F.; Derrah, R. I.; Ruthven, D. M., On the Measurement of Zeolitic Diffusion Coefficients. *Can. J. Chem Eng.* **1971,** *49*, (1), 66-&.

[10] Popplewell, J.; Sakhnini, L., The Dependence of the Physical and Magnetic-Properties of Magnetic Fluids on Particle-Size. *J. Magn. Magn. Mater.* **1995,** *149*, (1-2), 72-78.

[11] Hutson, N. D.; Reisner, B. A.; Yang, R. T.; Toby, B. H., Silver Ion-Exchanged Zeolites Y, X, and Low-Silica X: Observations of Thermally Induced Cation/Cluster Migration and the Resulting Effects on the Equilibrium Adsorption of Nitrogen. *Chem. Mat.* **2000,** *12*, (10), 3020-3031.

[12] Jayaraman, A.; Hernandez-Maldonado, A. J.; Yang, R. T.; Chinn, D.; Munson, C. L.; Mohr, D. H., Clinoptilolites for Nitrogen/Methane Separation. *Chem. Eng. Sci.* **2004,** *59*, (12), 2407-2417.

Chapter 5

Bottom-up Synthesis of Titanium Silicate Based Nanostructured Materials

The current chapter focuses on the bottom-up synthesis of a new family of titanium silicates (TS) nanostructured sorbent materials with flexible characteristics involving templated synthesis. The addition of an organic template during the TS synthesis results in the formation of structures with increased void volume for adsorption. The present work involves the synthesis and characterization of TS materials using tetramethylammonium hydroxide (TEAOH) as a structure-directing agent (SDA). Materials characterization includes scanning electron microscopy (SEM), infrared spectroscopy (FTIR), thermogravimetric analysis (TGA), powder x-ray diffraction (XRD), and *in situ* differential scanning calorimetry (DSC) powder XRD.

In addition to synthesizing these novel materials, the effectiveness of template removal was also studied, which is important in order to maximize the adsorption volume while still maintaining the crystallinity of the structure. The template removal process is a challenging one due to the apparent crystalline structure destruction during thermal treatment. One example of such method is traditional calcinations in air to burn off the SDA.

5.1 Introduction

Synthetic nanoporous materials have proven to be useful in many applications, such as adsorption, molecular sieving, ion exchange, and catalysis.[1-3] However, there is an ongoing effort to discover nanoporous crystalline materials to be tailored as highly selective and high capacity sorbents.[4, 5] There have been many nanoporous materials that exhibit desirable characteristics, such as small pore size and narrow pore-size distribution, for gas separation. Examples include carbon molecular sieves (CMS), Clinoptilolites, silicoaluminophosphates (SAPOs) and titanium silicates (TS).

Titanium silicates (TS) with both penta and octahedral coordination transition metal centers are materials with characteristics that allow alteration of the effective pore size, thus permitting passage of only molecules with specific dimensions and facilitating size exclusion based separations. For instance, flexible TS materials that have been tested for the purification of natural gas are the Engelhard TitanoSilicate (ETS) material series.[6] These materials are built of tetrahedral as well as penta and octahedral units, forming a class of mixed oxides containing tetrahedral coordinated silicon and octahedral and semi-octahedral coordinated titaniums.[6]

ETS-4 was first synthesized in 1990,[7] and since then many groups have studied this molecular sieve.[8-11] As-synthesized ETS-4 has been described as a material of low stability and has not been found to be useful in any applications. However, a strontium ion-exchanged ETS-4 was synthesized and found to be useful in light gas separations.[12] This Zorite-like titanosilicate molecular sieve presents adjustable pores for size-selective

adsorption of small molecules.[6, 11-13] For example, the effective pore size of strontium exchanged ETS-4 decreases as the dehydration temperature is increased, allowing this material to be used for the separation of mixtures of molecules with similar sizes in the 4.0 to 3.0 Å range such as N_2/CH_4, Ar/O_2 and N_2/O_2 pairs. The observed equilibrium adsorption uptakes, however, indicate that the material has low capacities even at pressures around 1 atm.[9, 14] This is due to the absence of cages in ETS-4 materials, which should significantly decrease pore volume and, therefore, sorption capacity. To include such framework volume characteristics while preserving small pore dimensions, it is often necessary to employ templated synthesis routes.

The use of organic amines as SDAs influences the subsequent crystallization during the zeolitic synthesis[1] generating precursors that direct the structure elements assembly around them.[15] It is now possible to design nanoscale-frameworks by controlling specific synthesis variables.[16]

5.2 Experimental Section

5.2.1 Sorbent Synthesis. Modified titanium silicates based on a Zorite starting composition were prepared at different SiO_2, and HCl ratios using hydrothermal synthesis and a molecular SDA (TEAOH). Figure 5-1 shows a ternary plot signed with all the as-synthesized material variants. All the materials were identified as UPRM-4*x* where the *x* represent a letter from *a* to *j*. The reactants used for the synthesis of all variants were sodium silicate solution (27 wt % SiO_2, Sigma-Aldrich), titanium (III) chloride (Aldrich), sodium hydroxide (Sigma), potassium fluoride dihydrate (98 wt %, Aldrich),

tetramethylammonium hydroxide (TEAOH, Fluka), hydrochloric acid (37 wt %, Sigma-Aldrich), and distilled/deionized water. The mixtures were heated to 453 K inside sealed Teflon lined autoclaves under autogenous pressure heads for periods up to 14 days. The final products were recovered via filtration and washed with copious amounts of deionized water and dried in a forced convection oven for 24 hours at 363 K.

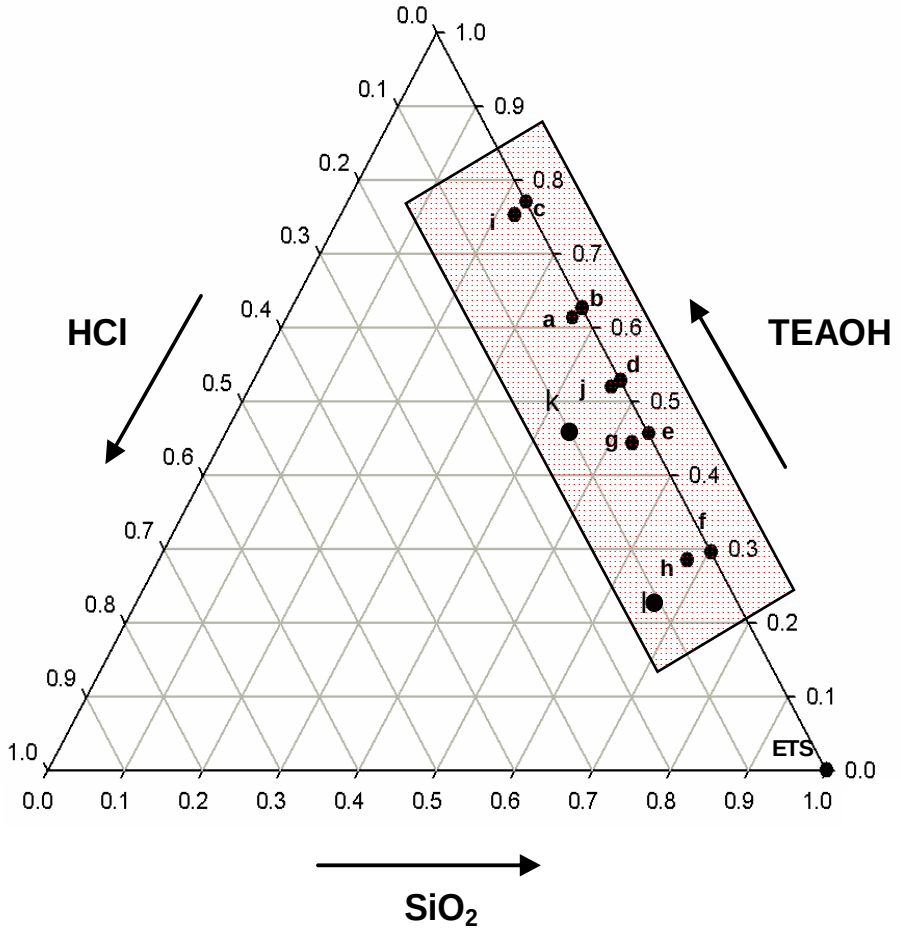

Figure 5-1. UPRM-4x composition terniary plot.

5.2.2 Sorbent Characterization. The as-synthesized materials were characterized by X-ray powder diffraction (XRD), scanning electron microscopy (SEM), infrared spectroscopy (FTIR), differential scanning calorimetry (DSC-XRD), thermo gravimetric

analyzer (TGA), and Synchrotron X-ray powder diffraction. XRD patterns were obtained using a Rigaku Ultima III Theta-Theta Goniometer unit equipped with a Cu Kα target operating at 40 kV and 44 mA with a continuous scanning rate. The diffraction patterns were used to evidence the crystallinity of the as-synthesized materials. SEM micrographs were obtained using a JEOL JSM-6390. The images were obtained following standard procedures for low conductive samples. These images provided preliminary data on the morphology of the materials. FTIR data were obtained on a Varian 800 FT-IR and were used to analyze the SDA removal characteristics. DSC-XRD data was obtained by using a DSC attachment with flowing helium at 100 cc/min and a heating rate of 5 °C/min. This data was used to observe the process of the SDA elimination, as well as changes in structure and framework as heat was added. TGA analyses were performed in a TA Q500. TGA data was used to follows the progress of the material weight-loss in helium at 100 cc/min and a heating rate of 5 °C/min. Synchrotron X-ray powder diffraction experiments were performed at the beamline 11-BM of the Advanced Photon Source (APS) at Argonne National Laboratory. The 11-BM diffractometer has 12 analyzers and offers simultaneous high-speed (< 1 hr) and high-resolution (<2 x 10^{-4} $\Delta Q/Q$) data collection. The data will be used for unit cell determination and refinement and these results will be reported elsewhere.

5.2.3 Template Removal. A conventional technique to remove the SDAs (detemplation) consists of calcination methods using flowing air in a computer-controlled muffle furnace to decompose the template. A temperature of ca. 823 K has been reported for the removal of TEAOH from other zeolitic materials.[17, 18] Due to the expected thermo sensibility of our as-synthesized materials, non-traditional methods for template removal were studied in detail.

5.2.3.a Solvent Extraction. The samples were extracted to remove the SDA from the intrazeolitic pore space. The solvent extractions were performed in a one-step equilibration batch system using 0.5 g of sorbent in 175 ml of acetic acid solution (28.5 wt%) for 24 hours at 373 K. After the extraction step, samples were filtered and washed with deionized/distilled water and dried at 363 K for 24 hr in a forced convection oven. Additional studies were performed by varying the pH of the extraction solution from 2 to 10 via the controlled addition of a 15 wt % NaOH solution.

5.2.3.b Ion Exchange. The ion exchange procedures were performed in a one-step equilibration batch system using 0.5 g of sorbent in 175 ml of an NH_4Cl solution 1 M at 80 ºC for 24hr.[17] After the ion exchange step, samples were filtered and washed with deionized/distilled water and dried at 353 K for 24 hr in a forced convection oven.

5.3 Results and Discussion

5.3.1 Sorbents Characterization. Figures 5-2 to 5-5 show the SEM micrographs for all the as-synthesized materials. Many of the sorbents presented different crystals morphologies within the same sample which suggested the presence of multiple phases. It is also evident that small differences in the gel composition produced dramatical changes in the final product morphology. After analyzing all of the aforementioned micrographs, it was found that the *a*, *d*, *h* and *l* variants presented what appeared to be the most homogeneous phases. Therefore, the rest of the discussion/result will focus on these variants. See Appendix H for additional results of the other variants.

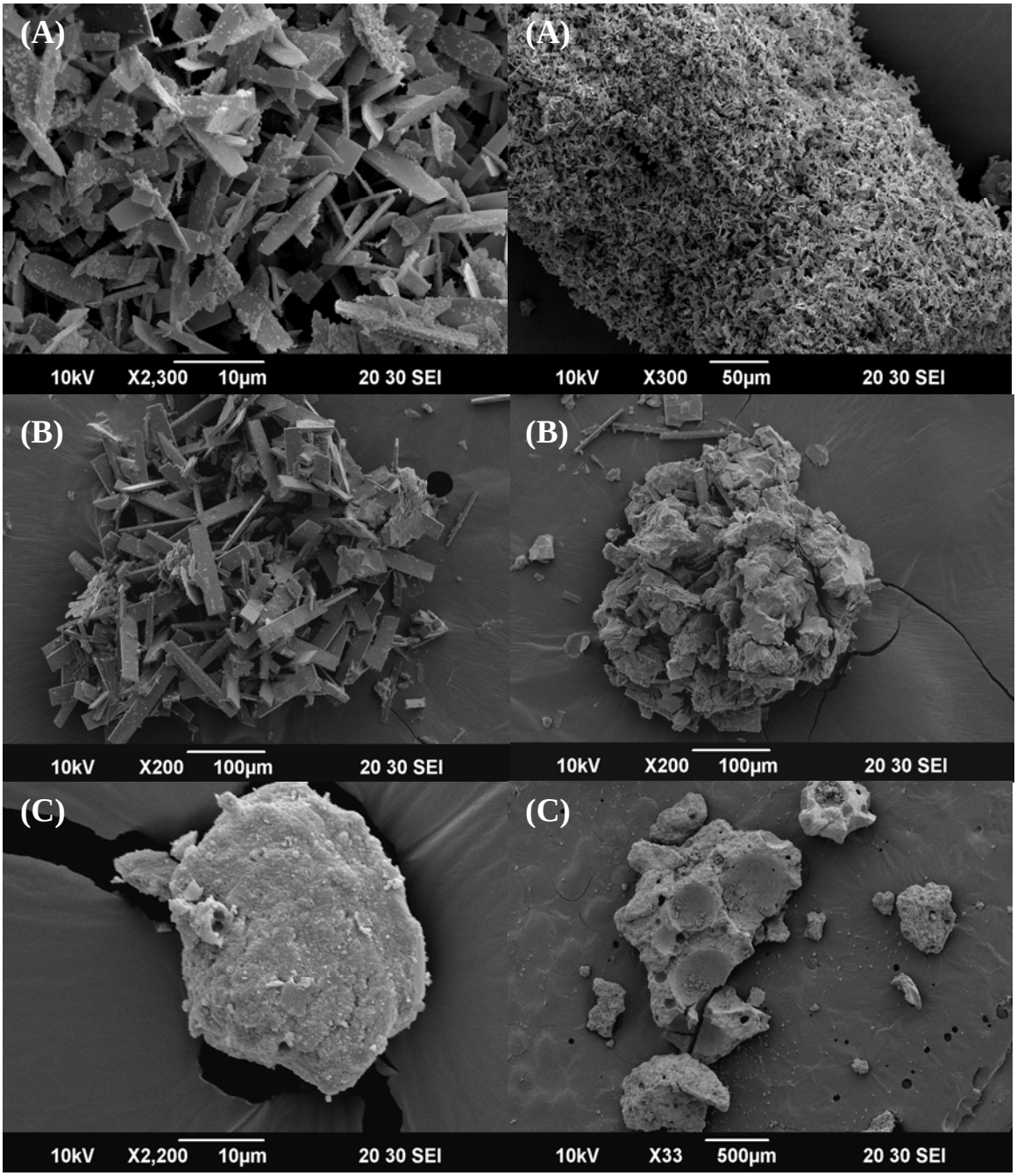

Figure 5-2: SEM images of (A) UPRM-4a, (B) UPRM-4b, and (C) UPRM-4c.

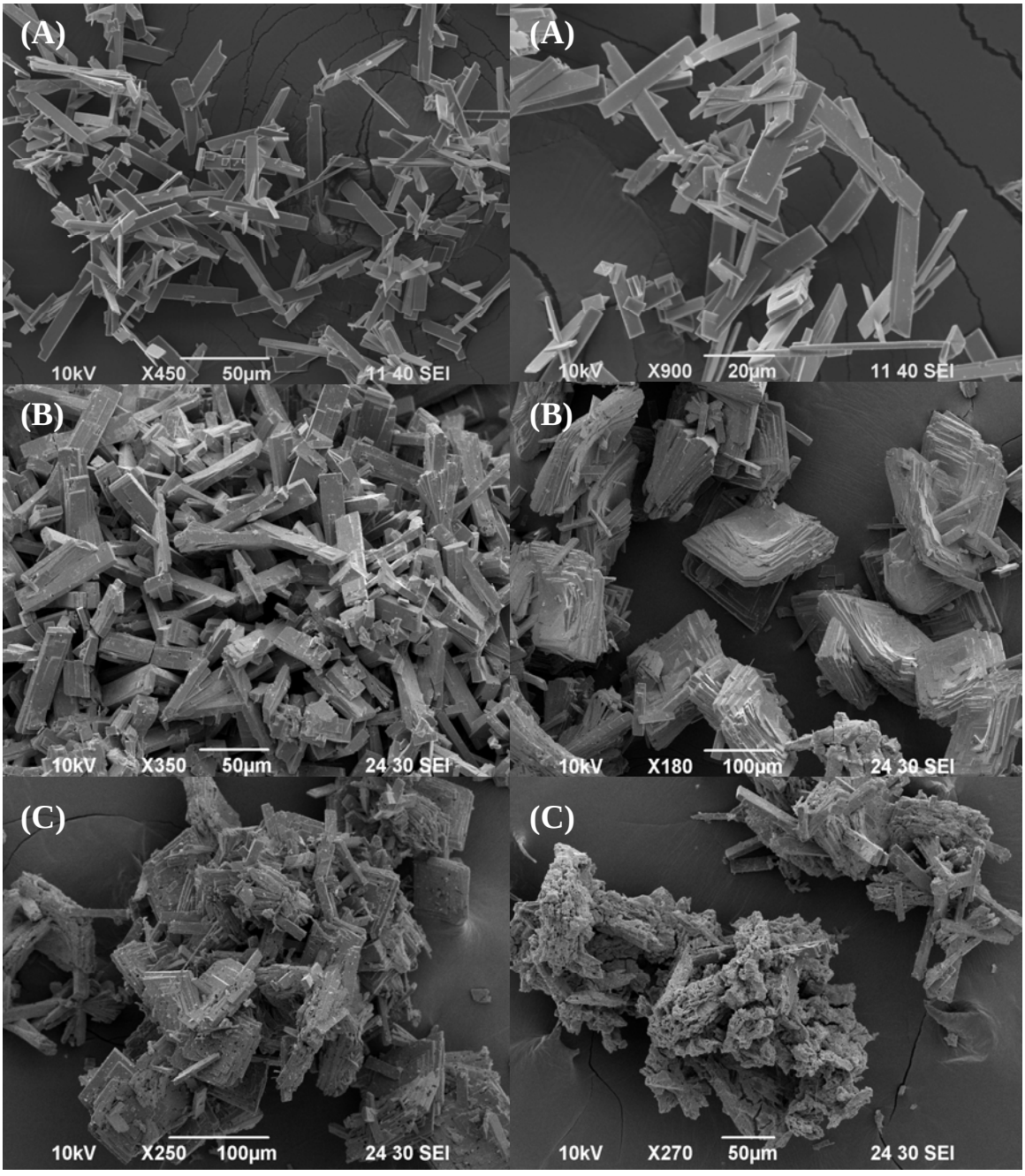

Figure 5-3: SEM images of (A) UPRM-4d, (B) UPRM-4e, and (C) UPRM-4f.

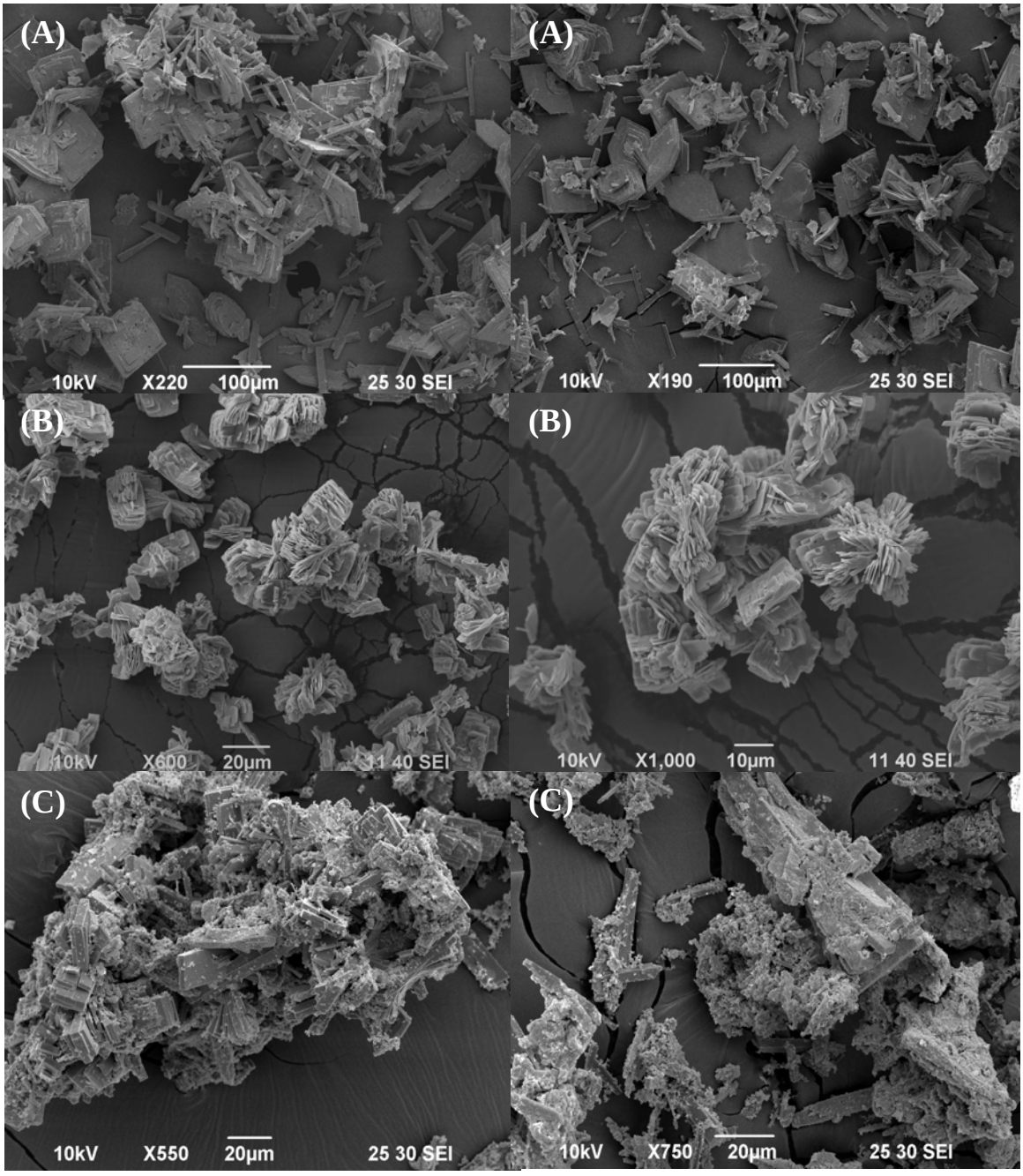

Figure 5-4: SEM images of (A) UPRM-4g, (B) UPRM-4h, and (C) UPRM-4I.

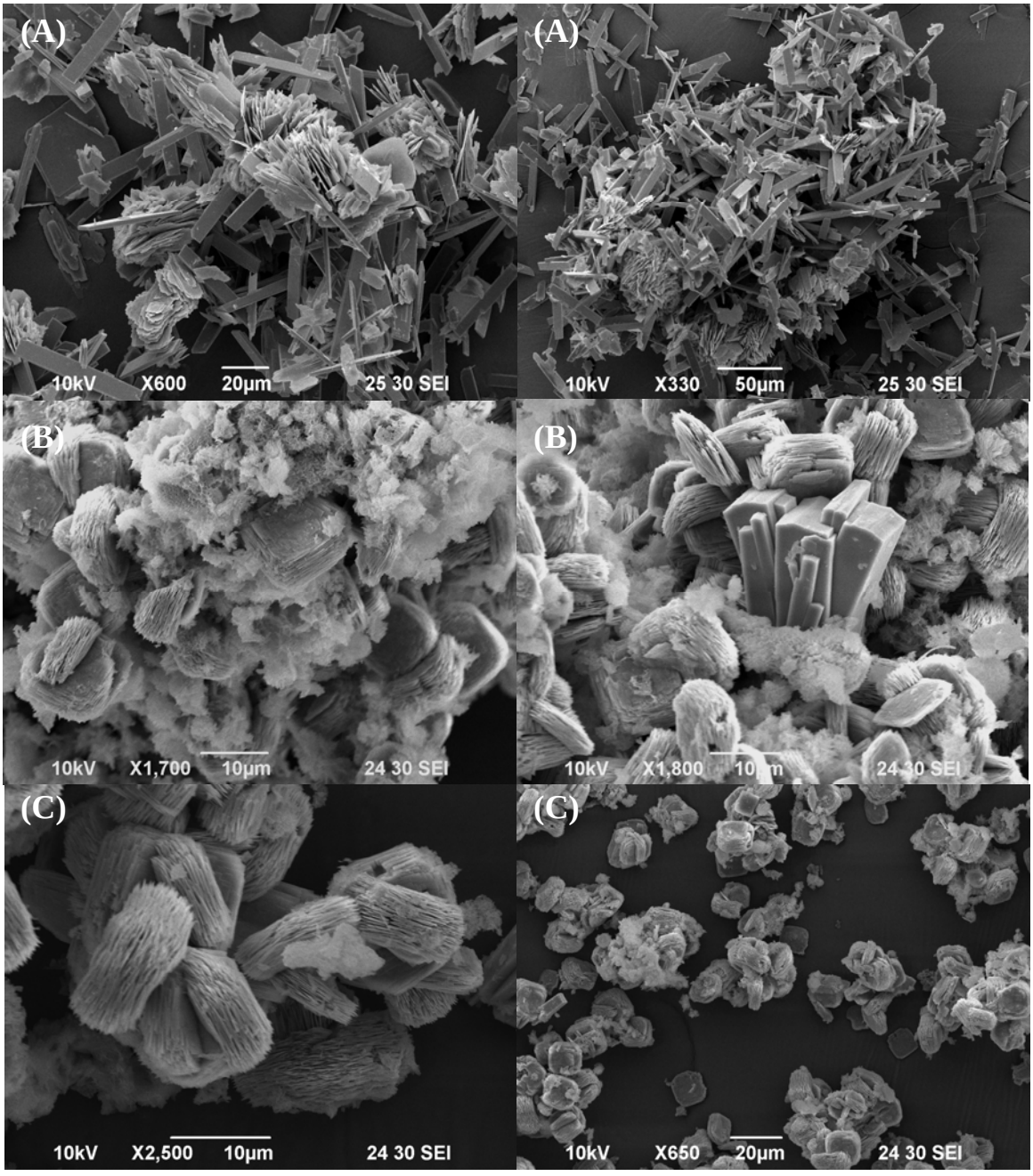

Figure 5-5: SEM images of (A) UPRM-4j, (B) UPRM-4k, and (C) UPRM-4l.

Figure 5-6 shows XRD data of the most homogeneous UPRM-4 materials, confirming the high crystallinity of the sorbent structures. UPRM a, d and h XRD patterns do not agreed with those reported in the literature for ETS-4 or to any other titanosilicate. However, the XRD data of UPRM-4l corresponded with those reported for ETS-10 prepared from $TiCl_3$ precursors.[19]

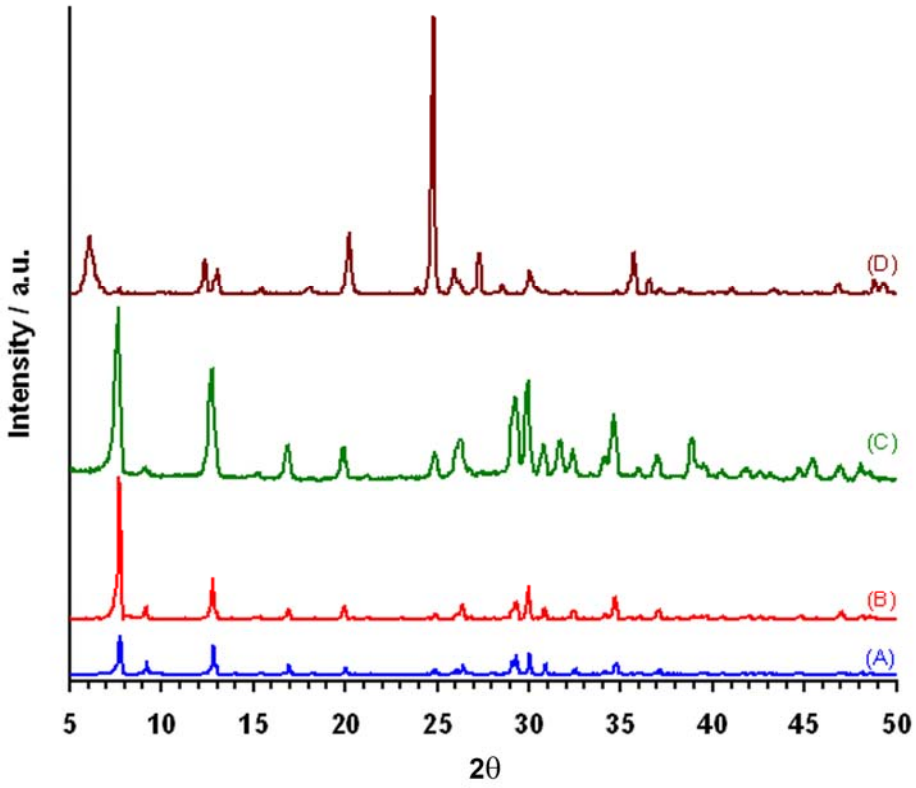

Figure 5-6: XRD patterns of (A) UPRM-4a, (B) UPRM-4d, (C) UPRM-4h, and (D) UPRM-4l.

In spite of the similarity among the XRD patters of the as-synthesized UPRM a, d and h, these materials present differences in there structure stability. This was evidenced in the XRD-DSC (Figures 5-7 to 5-9) and TGA (Figure 5-10) analyses. From the DSC data is evident that UPRM-4d required more energy to breakdown the structure when compared

to the other materials. The XRD patterns show that many of the diffraction peaks still remain at higher temperatures (over 500 K) when compared to the other cases. Further evidence of higher stability is provided by the TGA data in which the last weight loss transition, attributed to the loss of structural water and the breakdown of template, occurred over 500 K. The reported corresponding temperature for the as-synthesized ETS-4 material is ca. 473 K.[12, 20] It is plausible to state at this stage of the discussion that the template incorporated in the UPRM-4 structures extends the thermal stability range of the frameworks.

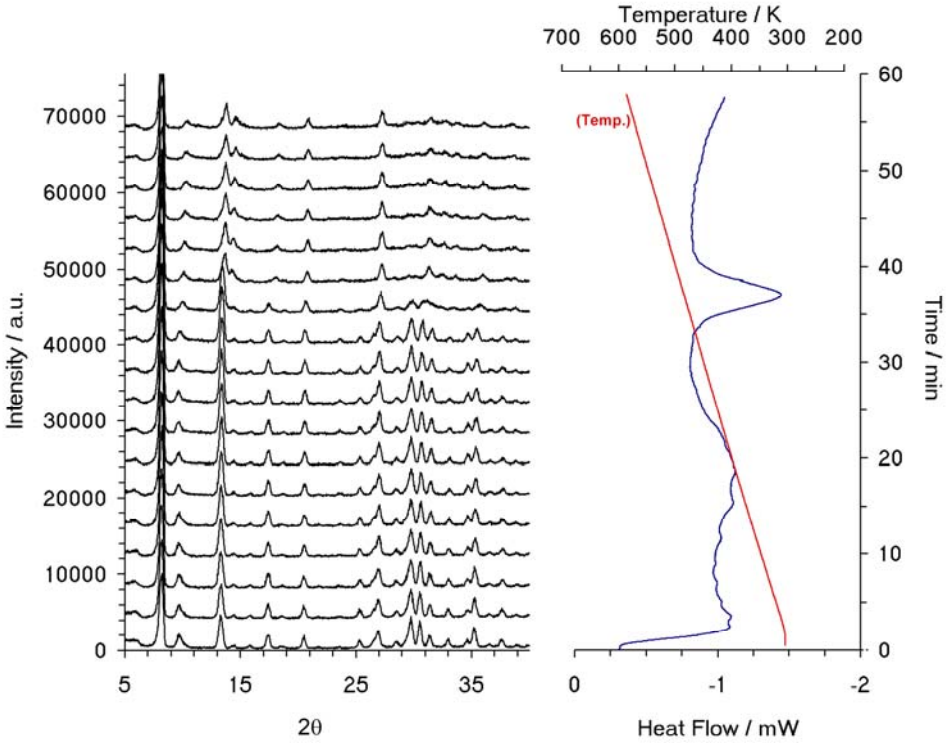

Figure 5-7: XRD-DSC patterns of UPRM-4a.

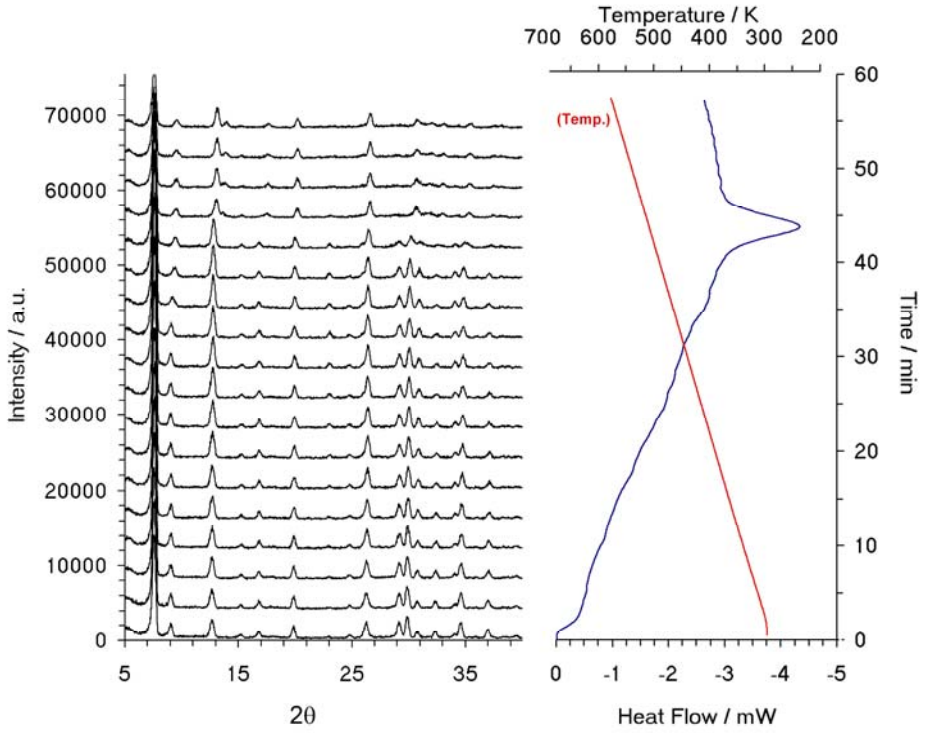

Figure 5-8: XRD-DSC patterns of UPRM-4d.

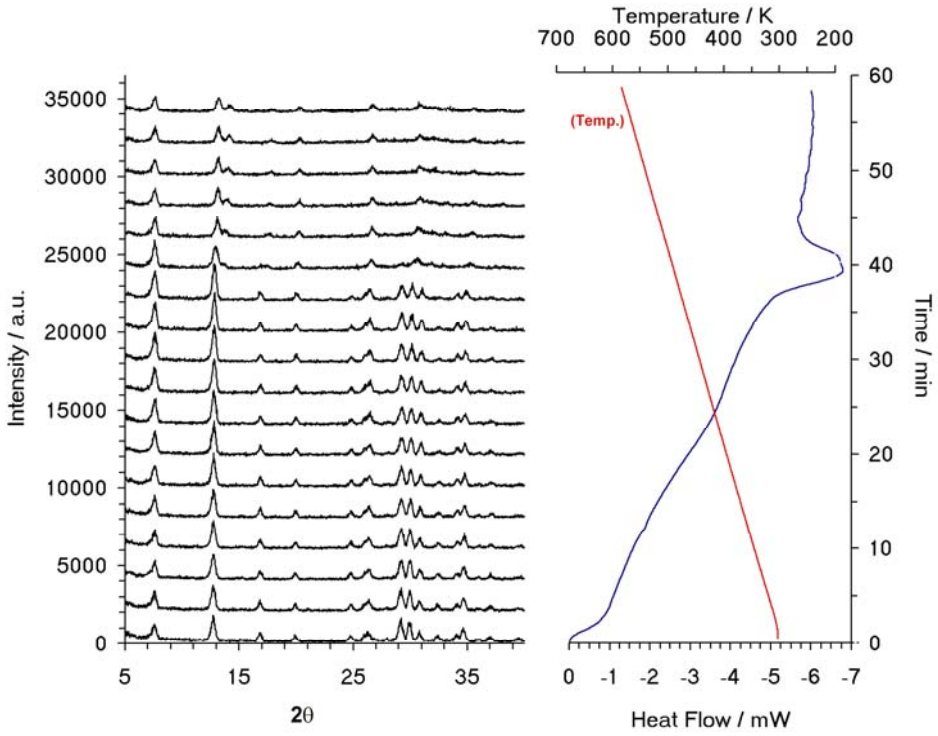

Figure 5-9: XRD-DSC patterns of UPRM-4h.

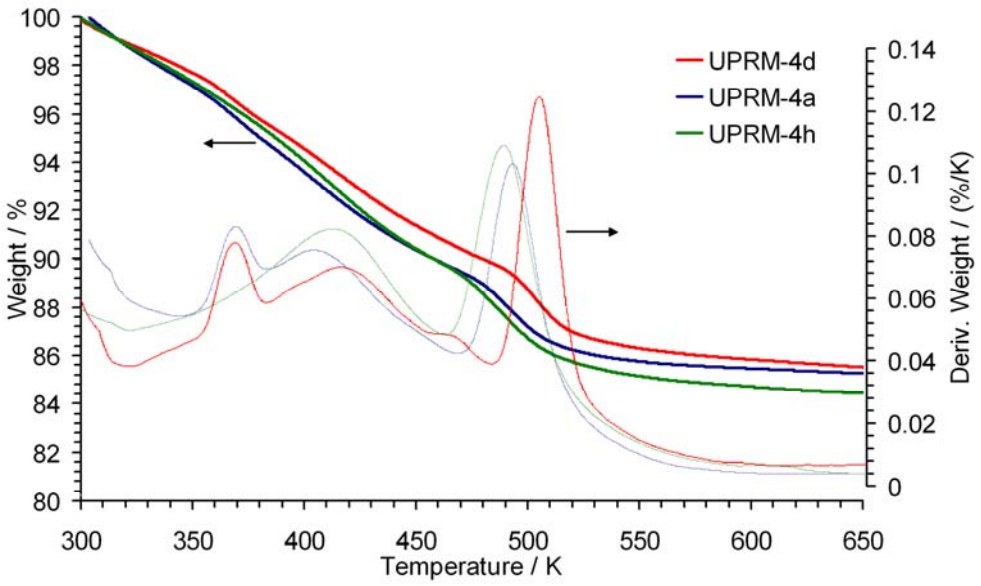

Figure 5-10: TGA data for UPRM-4a, UPRM-4d, and UPRM-4h.

5.3.2 Template Removal. DSC and TGA data (Figures 5-7 to 5-10) confirmed that the use of traditional calcination at temperatures over 500 K would produce detrimental changes to the framework of the sorbents. UPRM-4a surface area analysis were performed for samples treated in air at 773 K, and in vacuum at 648 and 373 K, giving surface area results of 5, 6, and 8 m^2/g, respectively. Although initial data of the new as-synthesized material proved the presence of a highly crystalline structure, the low thermal stability of the material also proved to be a problem for detemplation. For ETS-4, Armaroli and co-workers reported that the surface area is ca. 19 m^2/g.[8] It is plausible to state that the reported surface areas do not take in to account the entire surface area related to the cages due to the materials access limits to the probing nitrogen molecules at 77 K. In other words, the expected surface area for our materials should be grater that those reported for ETS-4.

5.3.2.a Solvent Extraction. Non-traditional methods to remove the organic molecules from the as-synthesized materials includes the use of an extracting solvent (e.g. acetic acid).[17] Attempts for the removal of TEAOH from our materials were performed using an acetic acid solution (28.5 wt%) with a pH of ca. 2. Although the UPRM-4a surface area of the treated sample were ca. 250 m^2/g, XRD analysis showed that a different material phase was obtained. From the analysis, the material was identified as anatase,[21] one of the three mineral forms of titanium dioxide. Work in the literature indicates that under different pH values, especially acidic conditions, structural changes were produced on some titanosilicate materials, such as ETS-10.[22] Acid treatment leads to the dissolution of the siliceous species resulting in the conversion of the Ti moieties into the anatase phase.

Additional post-treatments were performed with acetic acid at different pH values to study the structure stability. The pH of the acetic acid was varied from 2 to 10 using a 15 wt % solution of sodium hydroxide. Figure 5-11 shows FTIR spectra (fingerprint area) for the treated UPRM-4a. It is evident that at pH 4 and under, mayor structural changes were observed. On the other hand, at pH over 4, the structure maintains its properties. The pH values have a vital impact on the sorbent structure and therefore on their adsorption properties. Although surface area analyses indicate that at basic pH the material is stable; the template was not removed satisfactorily. These results were in agreement with the FTIR spectrum in where the bands identified with the TEA ions were observed.

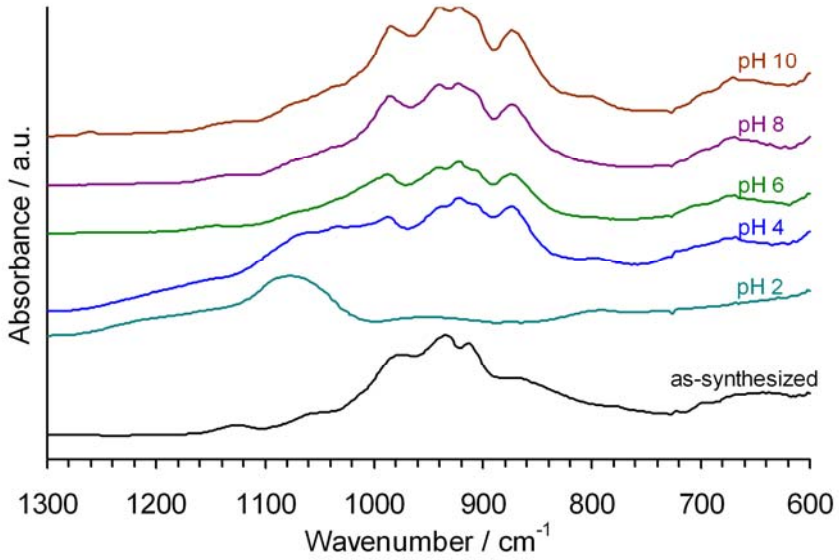

Figure 5-11: FTIR spectrum of solvent extracted UPRM-4a at different pH.

5.3.2.b Ion Exchange. Since the as-synthesized material pores are host to organic structure-directing agent cations, an ion exchange method was investigated to release the pore volume/surface area. The TEA ions, which balance the negative charges of the coordinated titanium atoms, were exchanged for ammonium ions. Detemplation was achieved via traditional aqueous phase ion exchange procedures employing an ammonium salt solution (pH ~ 5). FTIR analyses were performed to the TEA-UPRM-4d and the detemplated NH4-UPRM-4d samples (Figure 5-12). In FTIR, quaternary amine salts, as TEAOH, are characterized by the skeletal vibrations of NC_4. This vibrations are analogous to the quaternary carbon, NC_4, skeletal stretching. For the tetraethylammonium ions the antisymmetric and symmetric NC_4 stretching occurs at around the 1060-1030 cm^{-1} and 672-666 cm^{-1} regions.[23] As shown in Figure 5-12, the TEA-UPRM-4d spectrum confirms the presence of NC4 stretching, indicating that the TEA ions are present in the as-synthesized sample. The TEA ion bands are also present in the spectrum

for the solvent extracted materials presented previously in Figure 5-11. However, these signals are not present in the ion exchanged sorbent (Figure 5-12) indicating that the template removal was successfully achieved.

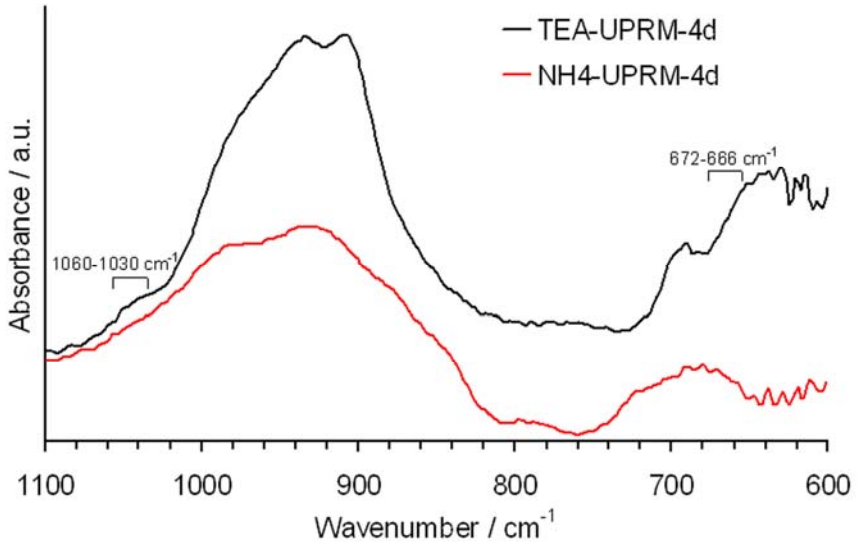

Figure 5-12: FTIR spectrum of as-synthesize TEA-UPRM-4d and ion exchanged NH4-UPRM-4d.

In addition, the surface area of the post-treated material was determined by volumetric adsorption porosimetry to be 32 m^2/g. When compared to the surface area of the as-synthesized material (5 m^2/g), it was concluded that the template had been removed. Surface areas for the ion exchanged UPRM-4a and UPRM-4h were 15 and 129 m^2/g, respectively. As mentioned before, the reported surface area for ETS-4 was 19 m^2/g. UPRM-4d and UPRM-4h present higher accessible surface areas than those reported for ETS-4 and these results also suggest that a modification of the original Zorite framework was obtained.

X-ray diffraction was used to verify the effect of the ion exchange on the crystallinity of the UPRM-4d samples. Figure 5-13 shows the X-ray patterns of TEA-UPRM-4d and the NH4-UPRM-4d. As can be seen in the diffractograms, both samples exhibit high crystallinity. No additional peaks belonging to other phases are observed. However, shifts in the peaks were observed which suggest that the interplanar spacing has been modified.

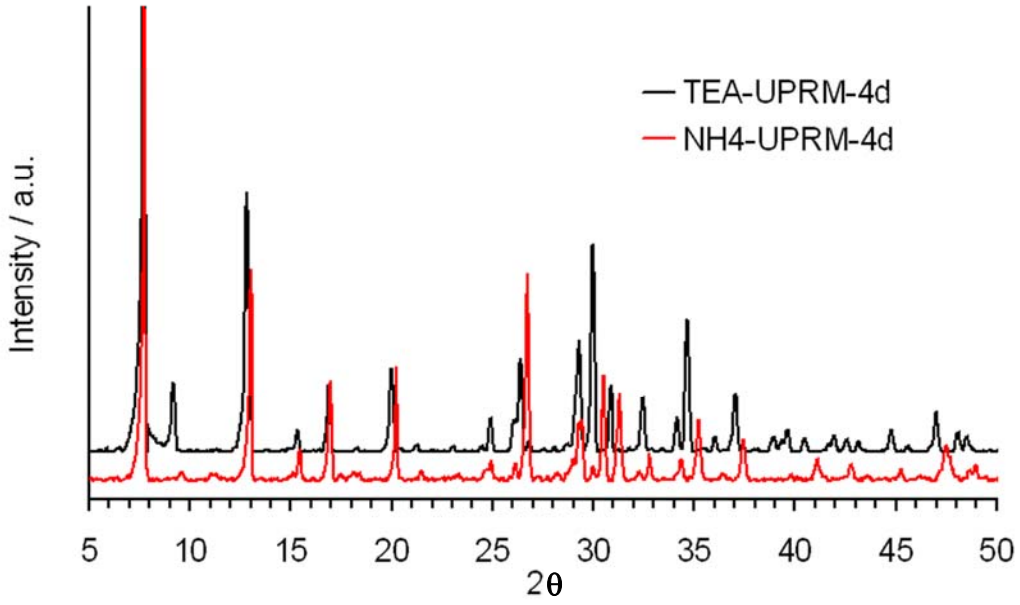

Figure 5-13: XRD patterns of as-synthesize TEA-UPRM-4d and ion exchanged NH4-UPRM-4d.

To fully understand the structural changes of this novel material, unit cell data calculation and refinement of the novel materials will be performed with the Synchrotron XRD data obtained from the Advance Photon Source at the Argonne National Laboratories (Figure 5-14). This part of the work will be performed in collaboration with Dr. Tsapatsis' research group at the University of Minnesota.

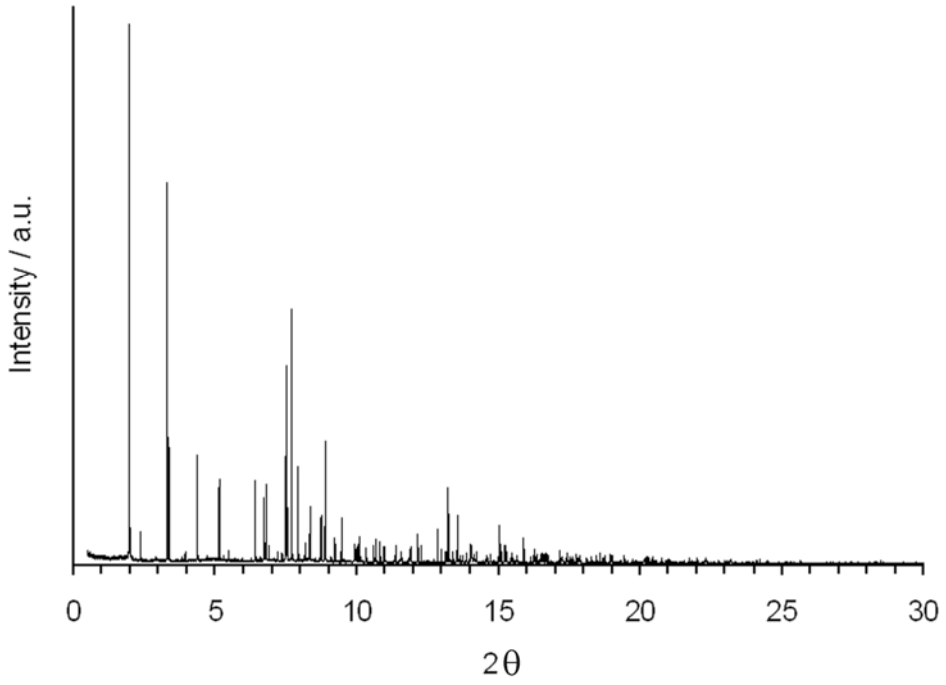

Figure 5-14: Synchrotron XRD patterns of as-synthesized TEA-UPRM-4d.

XRD-DSC analysis was performed to the detemplated sample to study its thermal stability (Figure 5-15). The sample is thermally stable up to about 475 K, after which all the peaks disappeared or diminished considerably in intensity. The release energy observed in the DSC data is attributed to the breakdown of the sorbent framework, due to the absence of the template molecules. These results are in agreement with the TGA data presented in Figure 5-16. After confirming the template removal, NH4-UPRM4d was ion exchanged with strontium (II) cations to increase the interactions between the sorbent and gas sorbates.[24] Additional structure characterization including Si MAS NMR and Ti MAS NMR for TEA-UPRM-4d and Sr-UPRM-4d and preliminary adsorption data for the Sr-UPRM-4h will be discussed in the next chapter.

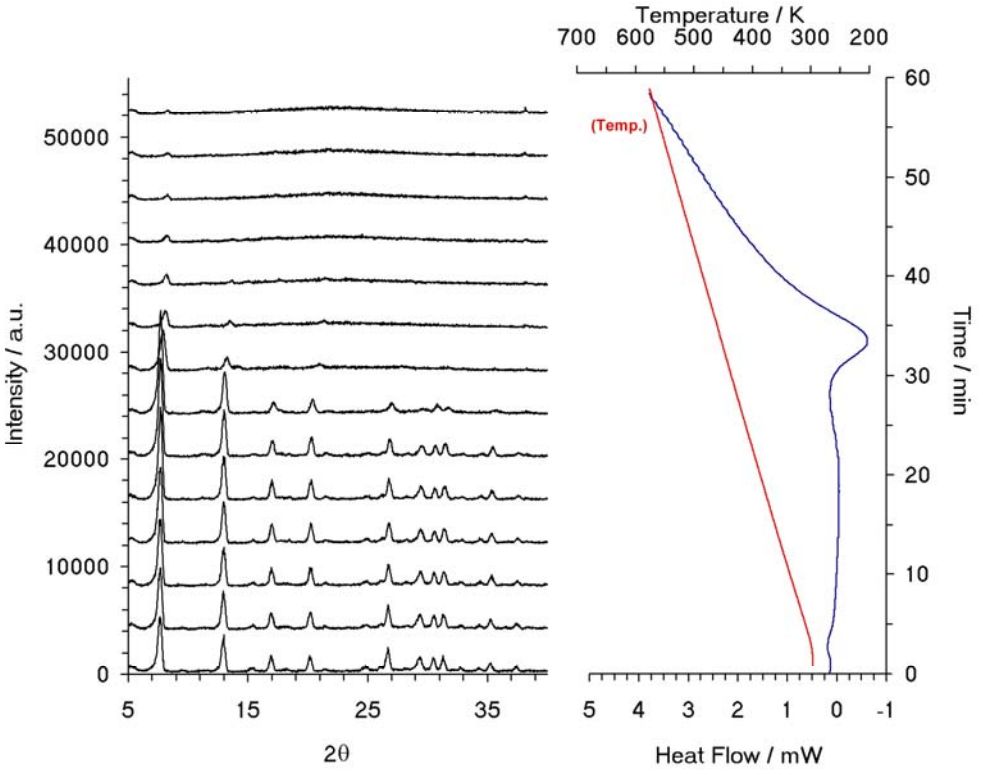

Figure 5-15. XRD-DSC patterns of NH4-UPRM-4d.

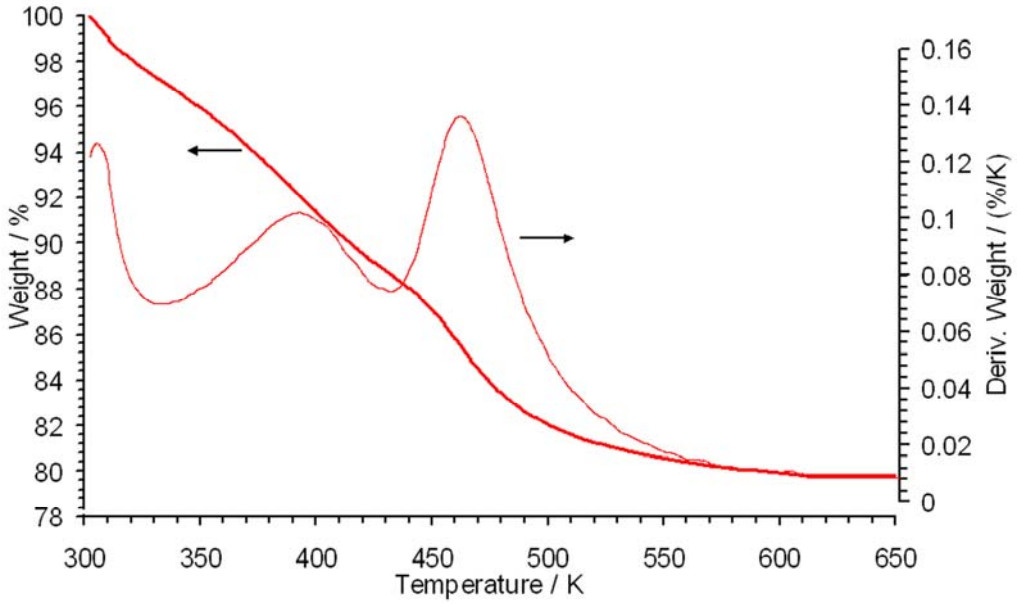

Figure 5-16: TGA data for NH4-UPRM-4d.

5.4 Conclusions

It has been found that by changing the SiO_2, TEAOH and HCl ratios, the structure of the material can be significantly altered. Our results have demonstrated that the titanosilicate UPRM-4d exhibits a crystalline structure, adequate thermal stability, flexible framework, and considerable surface area. After careful detemplation, UPRM-4d is a promising nanoporous material for large and selective adsorption of gas molecules.

5.5 References

[1] Yang, R. T., *Adsorbents: Fundamentals and Applications*. Wiley: New York, 2003.

[2] Hammonds, K. D.; Heide, V.; Dove, M. T., Rigid-unit Modes and the Quantitative Determination of the Flexibility Possessed by Zeolite Framework. *J. Phys. Chem. B* **1998,** *102*, 1759-1767.

[3] Yang, R. T., *Gas Separation by Adsorption Processes*. Butterworth: Boston, MA, 1987. Reprinted by Imperial College Press: London, 1997.

[4] Ruthven, D. M., Past Progress and Future Challenges in Adsorption Research. *Ind. Eng. Chem. Res.* **2000,** *39*, (7), 2127-2131.

[5] Szostak, R., *Molecular Sieves: Principles of Synthesis and Identification*. Van Nostrand Reinhold: New York, 1989.

[6] Braunbarth, C.; Hillhouse, H. W.; Tsapatsis, M.; Burton, A.; Lobo, R. F.; Jacubinas, R. M.; Kuznicki, S. M., Structure of Strontium Ion-Exchanged ETS-4 Microporous Molecular Sieves. *Chem. Mater.* **2000,** *12*, (7), 1857-1865.

[7] Kuznicki, S. M. Preparation of Small-Pored Crystalline Titanium Molecular Sieve Zeolites. U.S. Patent 4,938,939, 1990.

[8] Armaroli, T.; Busca, G.; Milella, F.; Bregani, F.; Toledo, G. P.; Nastro, A.; De Luca, P.; Bagnascod, G.; Turco, M., A Study of ETS-4 Molecular Sieves and of their Adsorption of Water and Ammonia. *J. Mater. Chem.* **2000,** *10*, 1699-1705.

[9] Kuznicki, S. M.; Bell, V. A.; Jacubinas, R. M.; Nair, S.; Braunbarth, C. M.; Hillhouse, H. W.; Tsapatsis, M., ETS-4 Pore Contraction: The Molecular Gate Effect. *Abstr. Pap. ACS* **2001,** *221*, U726-U726.

[10] Pillai, R. S.; Peter, S. A.; Jasra, R. V., Adsorption of Carbon Dioxide, Methane, Nitrogen, Oxygen and Argon in NaETS-4. *Micropo. Mesopor. Mat.* **2008,** *113*, 268-276.

[11] Philippou, A.; Anderson, M. W., Structural Investigation of ETS-4. *Zeolites* **1996,** *16*, (2-3), 98-107.

[12] Kuznicki, S. M.; Bell, V. A.; Nair, S.; Hillhouse, H. W.; Jacubinas, R. M.; Braunbarth, C. M.; Toby, B. H.; Tsapatsis, M., A Titanosilicate Molecular Sieve with Adjustable Pores for Size-Selective Adsorption of Molecules. *Nature* **2001,** *412*, (6848), 720-724.

[13] Mintova, S.; Valtchev, V.; Angelova, S.; Konstantinov, L., Kinetic Investigation of the Effect of Na, K, Li and Ca on the Crystallization of Titanium Silicate ETS-4. *Zeolites* **1997,** *18*, (4), 269-273.

[14] Jayaraman, A.; Hernandez-Maldonado, A. J.; Yang, R. T.; Chinn, D.; Munson, C. L.; Mohr, D. H., Clinoptilolites for Nitrogen/Methane Separation. *Chem. Eng. Sci.* **2004,** *59*, (12), 2407-2417.

[15] Tuel, A.; Taarit, Y. B., Synthesis of TS-1 from Titanosilicate Gels containing TPAOH/TEAOH and TPAOH/NH_4OH Mixtures *Microp. Mat.* **1993,** *1*, 179-189.

[16] Belén-Cordero, D. S.; Méndez-González, S.; Hernández-Maldonado, A. J., SBE Type Cobalt Aluminophosphate Nanoporous Materials: Degradation of the Structure-Directing Agent. *Micropo. Mesopor. Mat.* **2008,** *109*, 287-297.

[17] Takewaki, T.; Beck, L. W.; Davis, M. E., Zincosilicate CIT-6: A Precursor to a Family of *BEA-Type Molecular Sieves. *J. Phys. Chem. B* **1999,** *103*, 2674-2679.

[18] Rivera-Ramos, M. E.; Hernandez-Maldonado, A. J., Adsorption of N_2 and CH_4 by Ion-Exchanged Silicoaluminophosphate Nanoporous Sorbents: Interaction with Monovalent, Divalent and Trivalent Cations. *Ind. Eng. Chem. Res.* **2007,** *46*, 4991-5002.

[19] Rocha, J.; Ferreira, A.; Lin , Z.; Anderson, M. W., Synthesis of Microporous Titanosilicate ETS-10 from $TiCl_3$ and TiO_2: A Comprehensive Study. *Micropo. Mesopor. Mat.* **1998,** *23*, 253–263.

[20] Rocha, J.; Anderson, M. W., Microporous Titanosilicates and other Novel Mixed Octahedral-Tetrahedral Framework Oxides. *Eue. J. Inorg. Chem.* **2000**, 201-218.

[21] Li, J. G.; Ishigaki, T.; Sun, X., Anatase, Brookite, and Rutile Nanocrystals via Redox Reactions under Mild Hydrothermal Conditions: Phase-Selective Synthesis and Physicochemical Properties. *J. Phys. Chem. C* **2007,** *111*, 4969-4976.

[22] Lv, L.; Zhou, J. K.; Su, F.; Zhao, X. S., Local Structure Changes of Microporous Titanosilicate ETS-10 upon Acid Treatment. *J. Phys. Chem. C* **2007,** *111*, 773-778.

[23] Lin-Vien, D.; Colthup, N. B.; Fateley, W. G.; Grasselli, J. G., *The Handbook of Infrared and Raman Characteristic Frequencies of Organic Molecules*. Academic Press: San Diego, 1991.

[24] Rivera-Ramos, M. E.; Ruiz-Mercado, G. J.; Hernández-Maldonado, A. J., Separation of CO_2 from Light Gas Mixtures using Ion-Exchanged Silicoaluminophosphate Nanoporous Sorbents. *Ind. Eng. Chem. Res.* **2008,** *47*, 5602-5610.

Chapter 6

Selective CO_2 Adsorption Using Porous Titanosilicates

The use of organic amines as structure directing agents (SDA) clearly influences the subsequent during zeolitic synthesis[1] and generate precursors that direct the structure assembly around them.[2] It is now possible to design nanoscale-frameworks by controlling specific synthesis parameters.[3] Among the several compositional variants developed in our lab, UPRM-4d showed what appears to be a functional flexible high capacity titanium silicate (TS) framework. The post-detemplated material potential as a CO_2 selective sorbent is discussed in the following sections, including a direct comparison with in-house prepared Sr-ETS-4.

6.1 Introduction

An adsorption application of particular interest is that of the separation of mixtures of molecules of similar sizes, such as carbon dioxide, methane and nitrogen. The separation of nitrogen and carbon dioxide from methane is becoming increasingly important for natural gas recovery.[4] There is a large amount of "low-quality" natural gas reserves that contain significant amounts of nitrogen and carbon dioxide, which bring down the energy values.[5] This natural gas reserves need to be upgraded in order to meet the pipeline quality for minimum heating value specifications (970 BTU/ft^3).[6] Due to the small differences in kinetic size (CO_2 = 3.3 Å, N_2 = 3.64 Å, CH4 = 3.8 Å), it is important to understand and control surface interactions and framework topology, in order to allow for the separation of these gases. Based on these needs, recently there has been a search for nanostrucutured zeolitic-like sorbent materials with characteristics that allow for the separation of gas mixtures.[7-10]

A porous material that has been tested for the separation of light gases, including natural gas, is a titanium silicate known as ETS-4.[11] During the past decade, many groups have studied this Zorite-like titanosilicate molecular sieve that presents adjustable pores for size-selective adsorption of small molecules.[12-15] For example, the effective pore size of strontium exchanged ETS-4 decreases as the dehydration temperature is increased, allowing this material to be used for the separation of mixtures of molecules with similar sizes in the 4.0 to 3.0 Å range such as N_2/CH_4 Ar/O_2 and N_2/O_2 pairs. The observed equilibrium adsorption uptakes, however, indicate that the material has low capacities even at pressures around 1 atm.[5, 16] This is due to the absence of cages in ETS-4

materials, which should significantly increase pore volume and, therefore, sorption capacity. To include such framework volume characteristics while preserving small pore dimensions, it is often necessary to employ templated synthesis routes.

6.2 Experimental Section

6.2.1 Sorbent Synthesis. The sorbent was prepared using hydrothermal synthesis and a molecular SDA. The reactants used were sodium silicate solution (27 wt % SiO2, Sigma-Aldrich), titanium (III) chloride (Aldrich), sodium hydroxide (Sigma), potassium fluoride dihydrate (98 wt %, Aldrich), tetramethylammonium hydroxide (TEAOH, Fluka), hydrochloric acid (37 wt %, Sigma-Aldrich), and deionized water. The mixture was heated to 453 K inside a sealed Teflon lined autoclave under autogenous pressure for approximately 12 days. The final product was then filtered and washed with copious amounts of deionized water and dried in a convection oven for 24 hours at 363 K.

6.2.2 Sorbent Characterization. The materials were characterized by solid-state Si and Ti nuclear magnetic resonance (MAS NMR), inductive couple plasma analysis (ICP), ReactorX powder diffraction, and thermo gravimetric analyzer (TGA). MAS NMR experiments were performed on a ultra-narrow bore 833 MHz magnet with a Bruker DRX NMR console using a home-made single resonance 4 mm MAS NMR at the National High Magnetic Field Laboratory at the University of Florida in Tallahassee. For the Ti analyses the standard was $TiCl_4$ and the probe parameters were: Larmor frequency of 46.97 MHz, recycle delay of 2s, pulse length of 1 us (~ pi/10 small angle pulse), td of 1024, dwell time of 1.0 us a sample spinning rate of ~ 8 kHz, and 2048 scans 102400 for

TEA-UPRM-4d and 99900 for Sr-UPRM-4d. For the Si analyses, the standard was $Si(CH_3)_4$ and the parameters were: Larmor frequency of 165.55 MHz, recycle delay of 10s, pulse length of 1 us (~ pi/10 small angle pulse, td of 1024, dwell time of 5 us, a sample spinning rate of ~ 8 kHz, and 340 scans for TEA-UPRM-4d, and 594 for Sr-UPRM-4d. Elemental identification of surface features was obtained using a Perkin Elmer Optima 2000 ICP instrument. XRD patterns were obtained using Rigaku Ultima III Theta-Theta Goniometer unit equipped with a Cu Kα target operating at 40 kV and 44 mA and a ReactorX attachment. The data was obtained in flowing helium at 100 cc/min and a heating rate of 5 °C/min. TGA analyses were performed in a TA Q500.

6.2.3 Template Removal and Ion Exchange. To remove the template (TEAOH), the as-synthesize material was ion exchanged with an NH_4Cl solution 1 M at 353 K for 24hr.[17] After the template removal treatment, the sorbent was ion exchanged again but this time by a three step method using $SrCl_2 \cdot 6H_2O$ solutions with increasing concentrations (5 wt%, 7.2 wt%, and 8.8 wt%).[15] Each ion exchange step was performed at 353 K for 1.5hr and the recovered samples washed with copious amounts of distilled/deionized water. Finally, the solid was dried in a forced convection oven for 24 hours at 363 K.

6.2.4 Adsorption Equilibrium Isotherms. Equilibrium isotherms were obtained using a ultra-high vacuum static volumetric adsorption system (Micromeritics ASAP 2020). Gases used were N_2 (High Purity grade, Linde), CH_4 (Ultra High Purity grade, Praxair), CO_2 (Ultra High Purity grade, Praxair), and H_e (High Purity grade, Linde). The latter was used as backfill gas after the sorbent activation. All samples were treated in vacuum *in*

situ at 363, 463 or 543 K prior to each sorption test. The nitrogen and methane equilibrium test were performed at 298 K while the carbon dioxide equilibrium tests were performed at 298 K and 323 K.

6.3 Results and Discussion

6.3.1 Sorbents Characterization. After confirming successful template removal (Chapter 5), NH4-UPRM4d was ion exchanged with strontium (II) cations to increase the interactions between the sorbent and the gas sorbates.[18] Figures 6-1 and 6-2 show the ^{29}Si MAS NMR spectra of the as-synthesized TEA-UPRM-4d and the strontium (II) ion exchanged Sr-UPRM-4d. The TEA-UPRM-4d spectrum exhibits two resonances at -93 and -97.5 ppm, with relative intensities of about 3.75:1. For ETS-4, Crusian and co-workers reported that two lines are observed at -90 and -95 with a ratio of 5:1.[19] Therefore, the former resonances can be attributed to two different silicon environments in the structure, the first one to Si(2Si,2$Ti_{oct.}$) and the latter to Si (3Si, 1$Ti_{semi\text{-}oct.}$).[14] It is plausible to state that TEA-UPRM-4d material is formed in a stacking fashion, having both 5- and 6-coordinated Ti atoms in the framework. By comparing the spectrum of the Sr-UPRM-4d with that of TEA-UPRM-4d, the two resonances that appear for the as-synthesized material were broadened and a sharp signal appear at -25 ppm, indicating that the Si environments were changed after the ion-exchange treatment. It is possible that some Ti positions were replaced by Sr ions so that the possibilities will be: Si(3Ti0Sr), Si(2Ti1Sr), Si(1Ti2Sr), Si(1Ti0Sr), and Si(0Ti1Sr). The first four possible distributions give the chemical shifts distributed from -90 to -95 ppm, while the last one gives the chemical shift at -25 ppm.

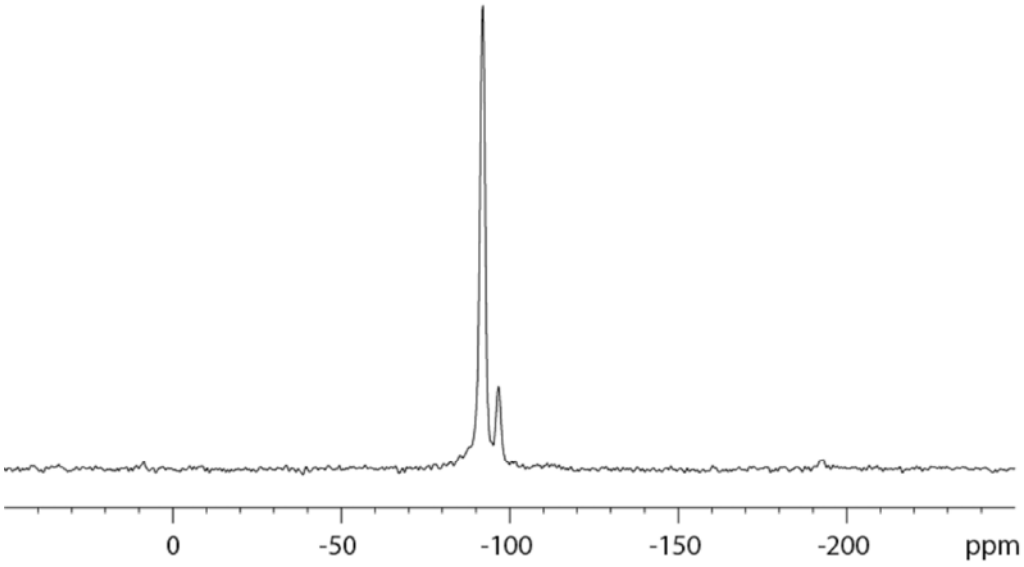

Figure 6-1. ^{29}Si MAS NMR spectrum of TEA-UPRM-4d spinning at 12 kHz ns=7300

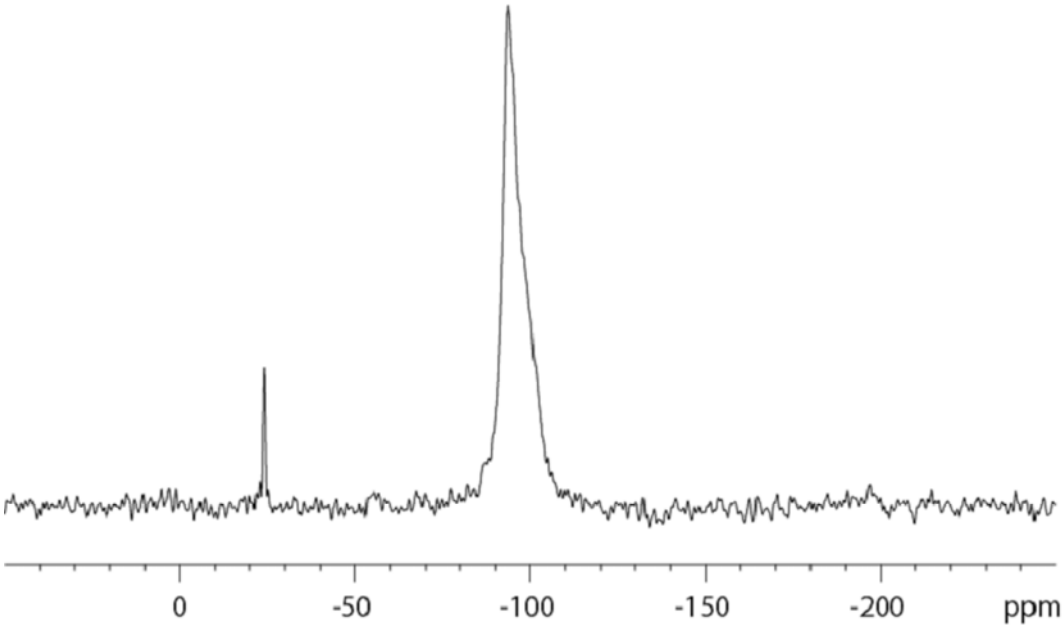

Figure 6-2. ^{29}Si MAS NMR spectrum of Sr-UPRM-4d spinning at 12 kHz ns=2200

Ti MAS NMR spectra recorded on an 830 MHz NMR spectrometer for TEA-UPRM-4d and Sr-UPRM-4d are presented in Figure 6-3. The peaks around 1000~2000 ppm and -4500 ppm appear to be background signals. Two resonance areas were identified at around 0 and -1000 ppm. Each area is composed of two resonance lines that are assigned to the ^{49}Ti and ^{47}Ti nuclides.[20-22] On the basis of the results obtained from the Si MAS NMR, the observed resonance can be attributed to two different Ti environments, semi-octahedral and octahedral Ti atoms. The similarities of both spectrums indicate that the Ti environments were not changed after the ion-exchange treatment. Additional MAS NMR data (e.g. Sr MAS NMR) and the unit cell data refinement will be necessary to fully understand the sorbent structure characteristics.

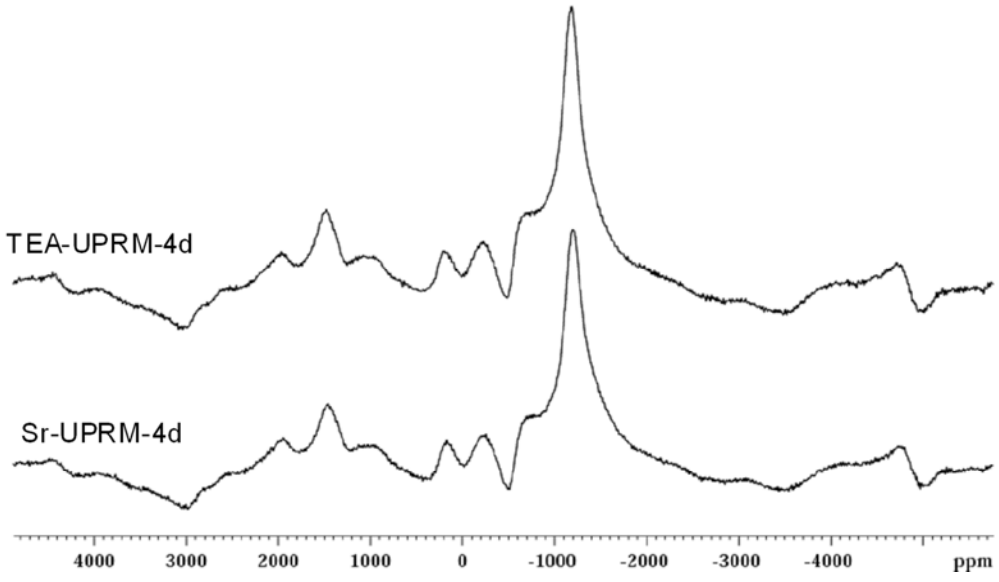

Figure 6-3. Ti MAS NMR spectra of TEA-UPRM-4d and Sr-UPRM-4d spinning at 8 kHz

Inductive couple plasma (ICP) analysis gave a Si/Ti and a (Na+K+Sr)/Ti of ca. of 4.5 and 5.18, respectively confirming the presence of the Sr^{2+} cations on the sorbent. The

reported Si/Ti and (Na+K)/Ti ratio for the as-synthesized ETS-4 were 2.6 and 1.5-2.0, respectively.[11]

Figure 6-4 shows the XRD patterns obtained with the Reactor X attachment for Sr-UPRM-4d. Evidently the structure was maintained after the ion exchanged treatment and continues to be stable up to 550 K. As the temperature is further increased, a shift of the peaks to lower d-spacing (higher 2) occurs, which is indicative of shrinkage of the pores system in the material. TGA data (Figure 6-5) shows a small inflection point at ca. 550 K, confirming that at this temperature the structure looses the remaining structural water and the framework starts to collapse. The total destruction and the partial volatilization of the structure occurred over 800 K. It is evident that the strontium exchange further extends the thermal stability range of the framework.

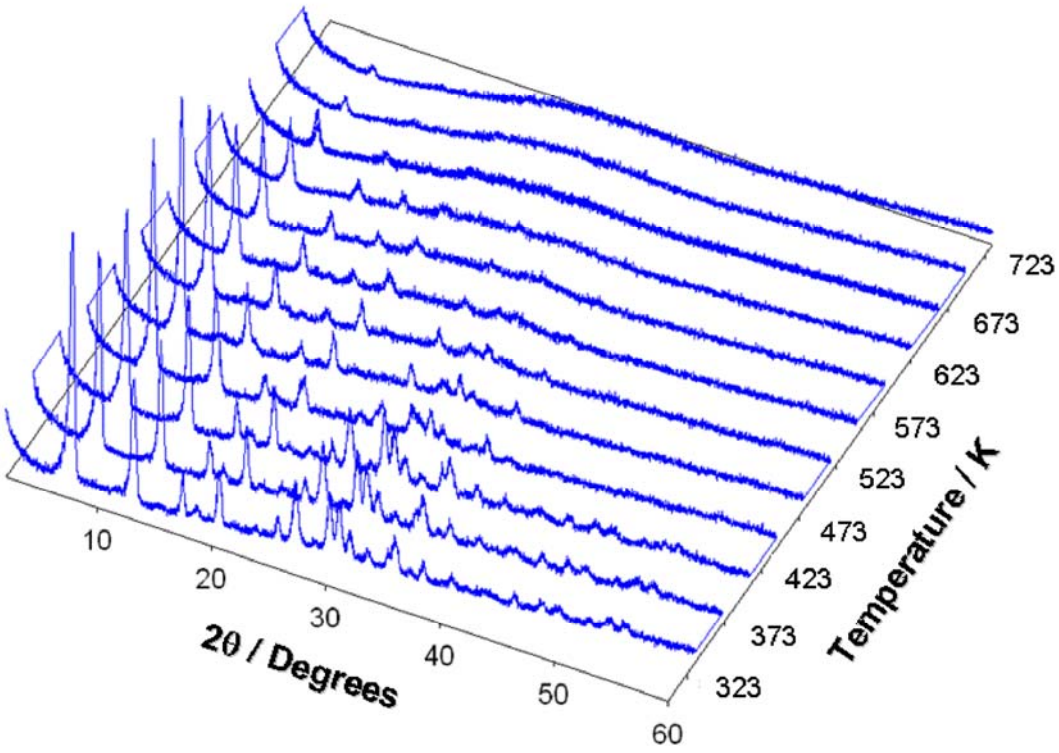

Figure 6-4. ReactorX diffraction patterns for Sr-UPRM-4d.

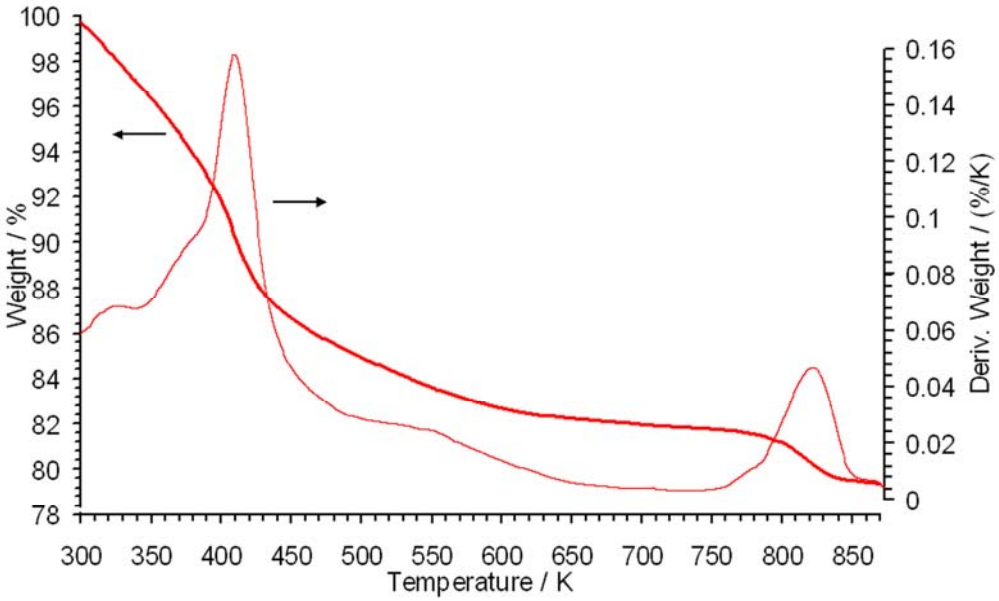

Figure 6-5: TGA data for Sr-UPRM-4d.

6.3.2 Equilibrium Adsorption and Isosteric Heat of Adsorptions

6.3.2.a NH4-UPRM-4d and Sr-UPRM-4d. Figure 6-6 shows pure component CO_2 adsorption isotherms on NH4-UPRM-4d and Sr-UPRM-4d at 298 K. Both sorbents were pre-treated at 363 K. The strontium exchanged sorbent evidently showcases stronger sorbent-sorbate interactions when compared to the NH_4 variant. A similar trend was also observed for the pure component adsorption of N_2 and CH_4. It should be mentioned that an isosteric heat of adsorption profile for CO_2 adsorption on Sr-UPRM-4d pre-treated at 363 K (see Figure 6-7) corresponds to a rather heterogeneous surface, something prominent in materials with cations occupying unique, exposed sites along the framework channels.[18] The estimated heats of adsorption presented in Figure 6-7 confirmed the strong interactions produced by strontium cations over CO_2 when compared to the NH_4 sorbent. This is in agreement with the fact that an increase of the cation charge results in much larger energies for polyvalent cations when compared to monovalent species.[18]

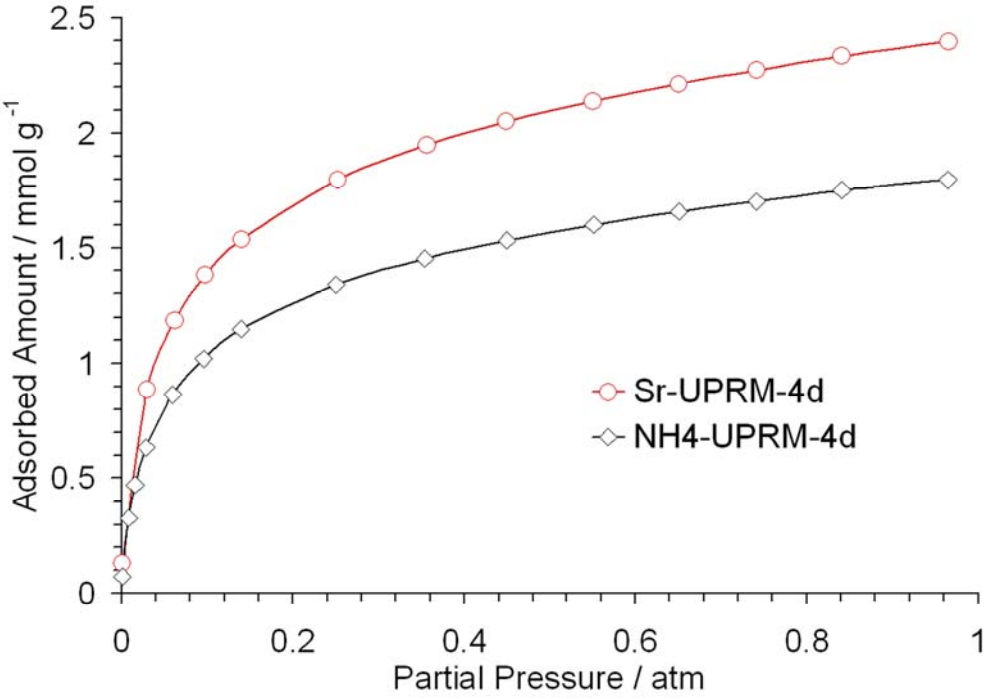

Figure 6-6. Pure component adsorption isotherms at 298 K for CO_2 on NH_4-UPRM-4d and Sr-UPRM-4d sorbents both pre-treated at 363 K.

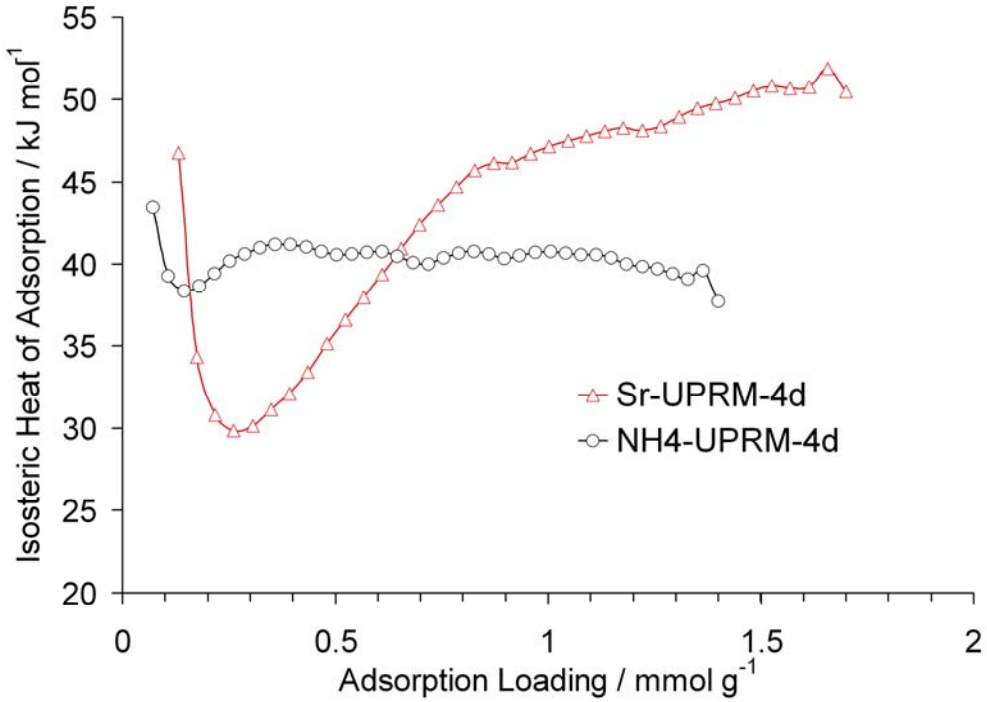

Figure 6-7. Isosteric heat of adsorption profiles for CO_2 on NH_4-UPRM-4d and Sr-UPRM-4d both pre-treated at 363 K.

6.3.2.b Sr-UPRM-4d Pore Gate Effect. Figure 6-8 shows CO_2 adsorption isotherms after sorbent activation at 363, 463 or 543 K. The considerable decrease in sorption capacity plausibly indicates a framework and/or pore contraction, similar to the one observed in ETS-4, a well known Zorite-like phase. Figures 6-9 to 6-11 show pure component isotherms of CO_2, CH_4, and N_2 on Sr-UPRM-4d pre-treated at 363, 463 or 543 K. In general, the sorbent displayed a remarkable selectivity towards CO_2 at all partial pressures. It seems at this point that a pre-treatment temperature of 363 K should result in the best overall CO_2 sorption capacity. CO_2 has a strong quadrupole moment (-4.3×10^{-26} $erg^{1/2}$ $cm^{5/2}$)[1] and should make a significant contribution to the total interaction potential or heat of adsorption.[23] In fact, the CO_2 quadrupole moment is 3 times greater than that of N_2. Since CH_4 molecules do not exhibit a quadrupole moment, the observed high selectivity towards CO_2 can only be attributed to its relatively strong quadrupole moment interaction with the cation electric field. Such interaction should also provide the ability to break steric barriers, if any, that the small channels of the framework could generate.

Adsorption results for the material pre-treated at 463 K (Figure 6-10) also shows N_2 selectivity over CH_4. It is plausible to state that this material presents a pore gate effect that depends of the pre-treatment temperature. This behavior could be attributed to the relocation of cations due to the loss of structural water during the dehydration process as in the case of ETS-4.[24, 25] Pre-treatment of the sample at 543 K (Figure 6-11) shows that higher temperature thermal treatment results in lower uptake of CO_2 as well as blockage of N_2 and CH_4 molecules.

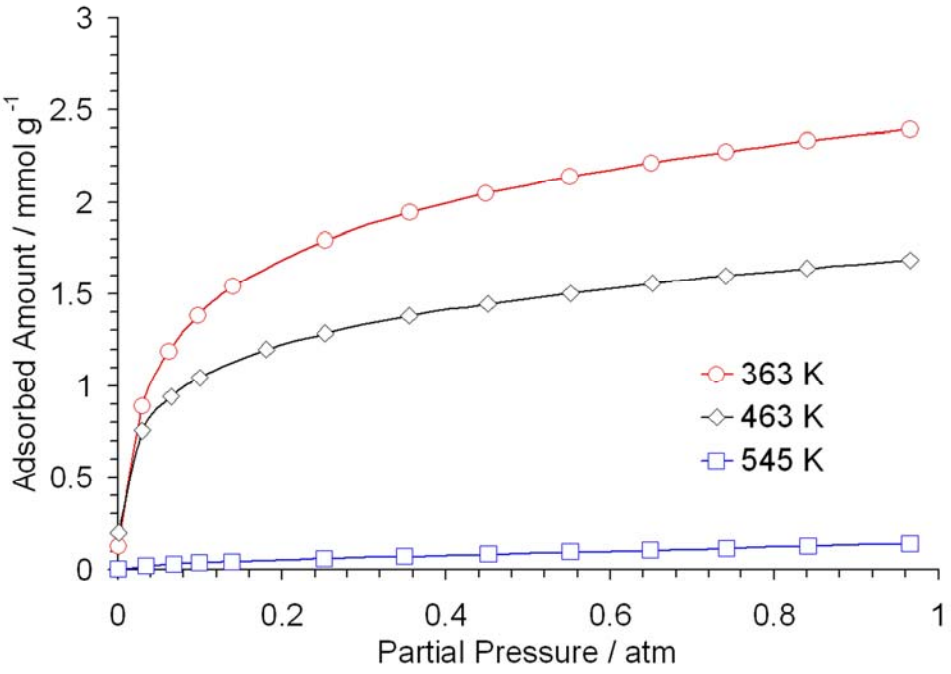

Figure 6-8. Pure component adsorption isotherms at 25 ºC for CO_2 on Sr-UPRM-4d pre-treated at 363, 463 or 543 K.

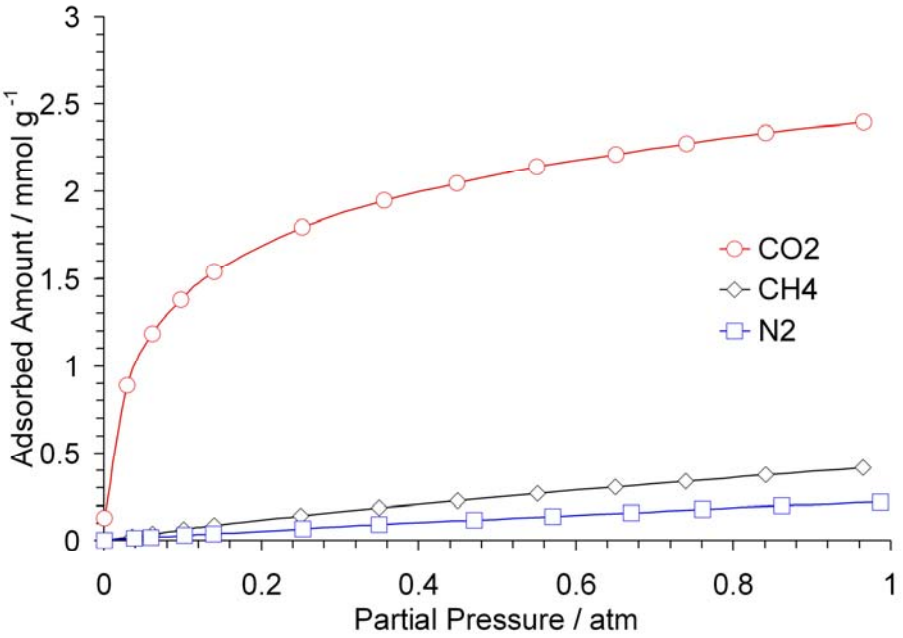

Figure 6-9. Pure component adsorption isotherms at 298 K for CO_2, CH_4, and N_2 on Sr-UPRM-4d pre-treated at 363 K.

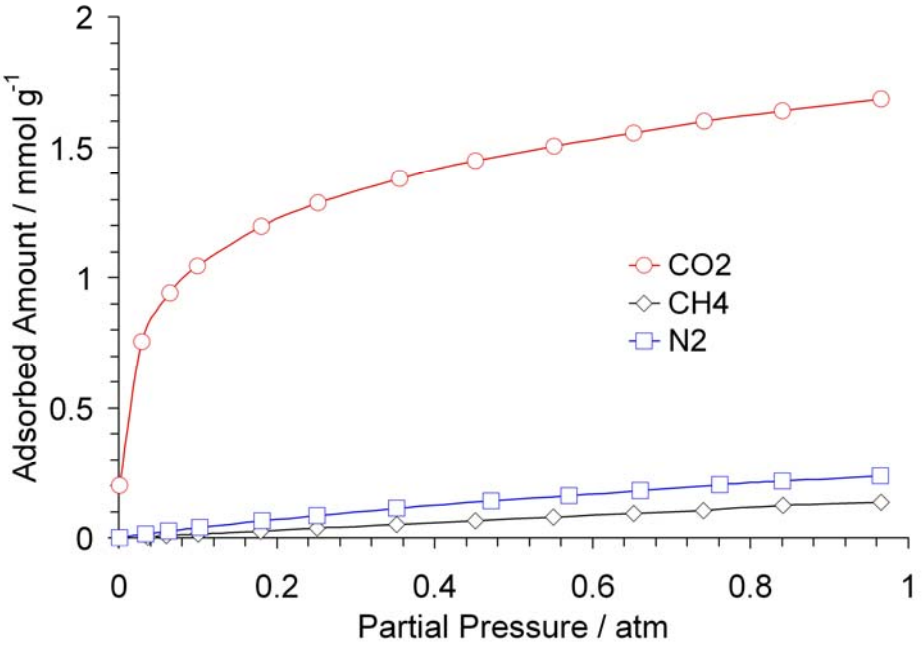

Figure 6-10. Pure component adsorption isotherms at 298 K for CO_2, CH_4, and N_2 on Sr-UPRM-4d pre-treated at 463 K.

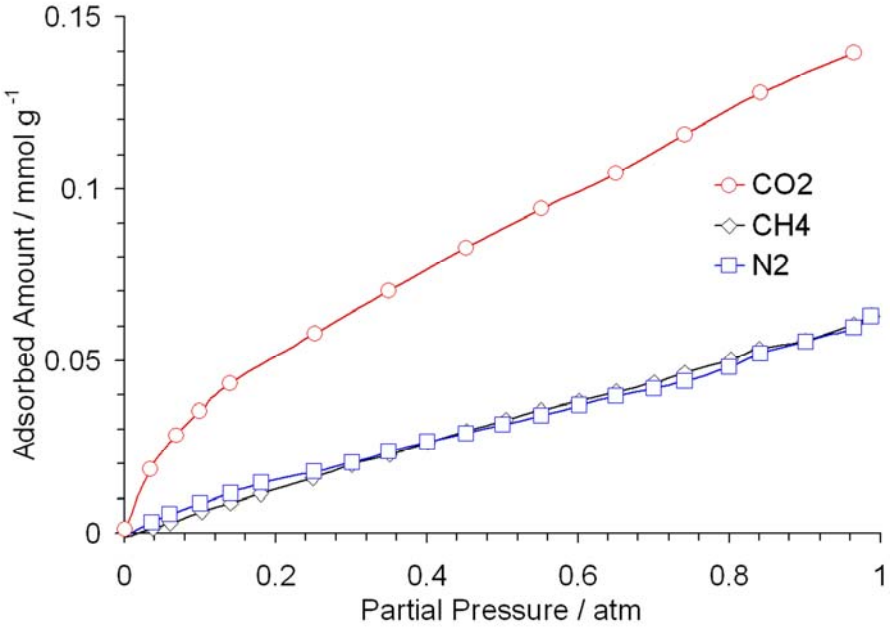

Figure 6-11. Pure component adsorption isotherms at 298 K for CO_2, CH_4, and N_2 on Sr-UPRM-4d pre-treated at 543 K.

Furthermore, CO_2 isosteric heats of adsorption profiles (see Figure 6-12) evidence rather strong interactions with the pores of the sorbent activated at 463 K. This could be the result of a considerable overlapping of the surface potential resulting from a pronounced pore diameter reduction. In other words the effective pore dimensions are within the range of the sorbate kinetic diameter. These results subtend that the extra-framework cations get displaced from their original positions during the heat treatment do to the coming out of the structural water molecules.

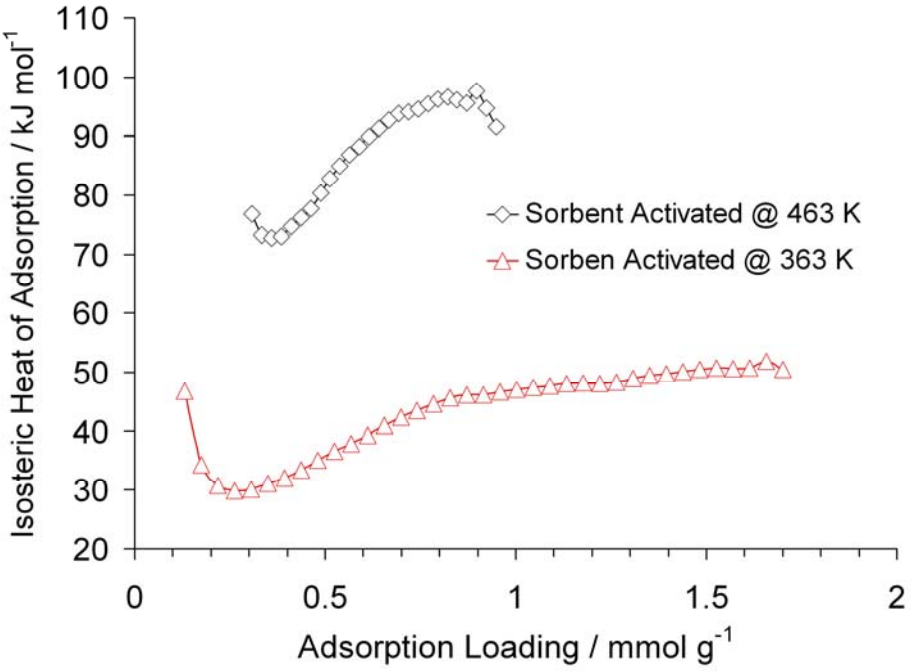

Figure 6-12. Isosteric heat of adsorption profiles for CO_2 on Sr-UPRM-4d pre-treated at different temperatures.

6.3.2.c Sr-UPRM-4d and Sr-ETS-4 CO_2 Adsorption Capacity. Figure 6-13 shows CO_2 isotherms at 298 K on Sr-UPRM-4d and Sr-ETS-4 both pre-treated at 363 K. At 1 atm, Sr-UPRM-4d adsorption capacity is more than double that of Sr-ETS-4, which probably indicates considerable framework differences.

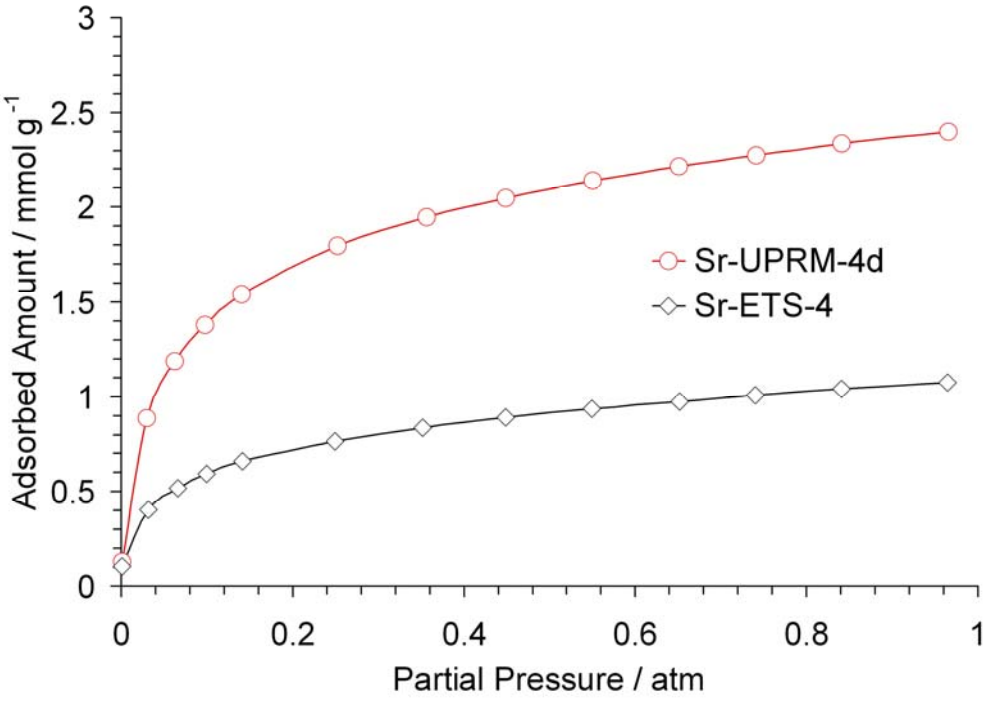

Figure 6-13. Pure component adsorption isotherms at 298 K for CO_2 on Sr-UPRM-4d and Sr-ETS-4 pre-treated at 363 K.

6.4 Conclusions

Our results have demonstrated that the titanosilicate UPRM-4d, after adequate template removal, is a promising nanoporous material for large and selective adsorption of CO_2 molecules. In general, material properties such as surface area and pore size are highly dependent on the synthesis recipe and following treatment of the titanosilicate. Since this leaves many variables open to consideration, the synthesis conditions have much room for improvement and future work should focus on optimization of the synthesis and post-synthesis parameters (e.g. temperature, time, ion exchange).

6.5 References

[1] Yang, R. T., *Adsorbents: Fundamentals and Applications*. Wiley: New York, 2003.

[2] Tuel, A.; Taarit, Y. B., Synthesis of TS-1 from Titanosilicate Gels containing TPAOH/TEAOH and TPAOH/NH_4OH Mixtures *Microp. Mater.* **1993,** *1*, 179-189.

[3] Belén-Cordero, D. S.; Méndez-González, S.; Hernández-Maldonado, A. J., SBE Type Cobalt Aluminophosphate Nanoporous Materials: Degradation of the Structure-Directing Agent. *Micropo. Mesopor. Mat.* **2008,** *109*, 287-297.

[4] Baker, R. W., Future Directions of Membrane Gas Separation Technology. *Ind. Eng. Chem. Res.* **2002,** *41*, (6), 1393-1411.

[5] Jayaraman, A.; Hernandez-Maldonado, A. J.; Yang, R. T.; Chinn, D.; Munson, C. L.; Mohr, D. H., Clinoptilolites for Nitrogen/Methane Separation. *Chem. Eng. Sci.* **2004,** *59*, (12), 2407-2417.

[6] *Emissions of Greenhouse Gases in the United States-DOE/EIA-0573*; 1936-4512; Energy Information Administration, Office of Energy Markets and End Use, U.S. Dept. of Energy: Washington, D.C., 1994.

[7] Frankiewicz, T. C.; Donnelly, R. G., Methane/Nitrogen Gas Separation over the Zeolite Clinoptilolite by the Selective Adsorption of Nitrogen. *ACS Symp. Ser.* **1983,** *223*, 213-233.

[8] Falamaki, C.; Mohammadi, A.; Sohrabi, M., N_2 and O_2 Adsorption Properties of an Iranian Clinoptilolite-Rich Tuff in the Original and Pre-Exchanged Forms. *Colloid. Surf. A* **2004,** *246*, (1-3), 31-37.

[9] Poshusta, J. C.; Tuan, V. A.; Pape, E. A.; Noble, R. D.; Falconer, J. L., Separation of Light Gas Mixtures Using SAPO-34 Membranes. *AIChE J.* **2000,** *46*, (4), 779-789.

[10] Li, S.; Falconer, J. L.; Noble, R. D., Improved SAPO-34 Membranes for CO_2/CH_4 Separations. *Adv. Mater.* **2006,** *18*, (19), 2601-2603.

[11] Kuznicki, S. M. Preparation of Small-Pored Crystalline Titanium Molecular Sieve Zeolites. U.S. Patent 4,938,939, 1990.

[12] Kuznicki, S. M.; Bell, V. A.; Nair, S.; Hillhouse, H. W.; Jacubinas, R. M.; Braunbarth, C. M.; Toby, B. H.; Tsapatsis, M., A Titanosilicate Molecular Sieve with Adjustable Pores for Size-Selective Adsorption of Molecules. *Nature* **2001,** *412*, (6848), 720-724.

[13] Mintova, S.; Valtchev, V.; Angelova, S.; Konstantinov, L., Kinetic Investigation of the Effect of Na, K, Li and Ca on the Crystallization of Titanium Silicate ETS-4. *Zeolites* **1997,** *18*, (4), 269-273.

[14] Philippou, A.; Anderson, M. W., Structural Investigation of ETS-4. *Zeolites* **1996,** *16*, (2-3), 98-107.

[15] Braunbarth, C.; Hillhouse, H. W.; Tsapatsis, M.; Burton, A.; Lobo, R. F.; Jacubinas, R. M.; Kuznicki, S. M., Structure of Strontium Ion-Exchanged ETS-4 Microporous Molecular Sieves. *Chem. Mater.* **2000,** *12*, (7), 1857-1865.

[16] Kuznicki, S. M.; Bell, V. A.; Jacubinas, R. M.; Nair, S.; Braunbarth, C. M.; Hillhouse, H. W.; Tsapatsis, M., ETS-4 Pore Contraction: The Molecular Gate Effect. *Abstr Pap Am Chem S* **2001,** *221*, U726-U726.

[17] Takewaki, T.; Beck, L. W.; Davis, M. E., Zincosilicate CIT-6: A Precursor to a Family of *BEA-Type Molecular Sieves. *J. Phys. Chem. B* **1999,** *103,* 2674-2679.

[18] Rivera-Ramos, M. E.; Ruiz-Mercado, G. J.; Hernández-Maldonado, A. J., Separation of CO_2 from Light Gas Mixtures using Ion-Exchanged Silicoaluminophosphate Nanoporous Sorbents. *Ind. Eng. Chem. Res.* **2008,** *47*, 5602-5610.

[19] Cruciani, G.; De Luca, P.; Nastro, A.; Pattison, P., Rietveld Refinement of the Zorite Structure of ETS-4 Molecular Sieves. *Micropo. Mesopor. Mat.* **1998,** *21*, 143-153.

[20] Gervais, C.; Veautier, D.; Smith, M. E.; Babonneau, F.; Belleville, P.; Sanchez, C., Solid State Ti-47,Ti-49, Sr-87 and Ba-137 NMR Characterisation of Mixed Barium/Strontium Titanate Perovskites. *Solid State NMR* **2004,** *26,* (3-4), 147-152.

[21] Dmitrieva, L. V.; Vorotilova, L. S.; Podkorytov, I. S.; Shelyapina, M. E., A Comparison of NMR Spectral Parameters of Ti-47 and Ti-49 Nuclei in Rutile and Anatase. *Phys. Solid State* **1999,** *41,* (7), 1097-1099.

[22] Padro, D.; Howes, A. P.; Smith, M. E.; Dupree, S. R., Determination of Titanium NMR Parameters of ATiO3 Compounds: Correlations with Structural Distortion. *Solid State NMR* **2000,** *15*, 231-236.

[23] Aguilar-Armenta, G.; Hernandez-Ramirez, G.; Flores-Loyola, E.; Ugarte-Castaneda, A.; Silva-Gonzalez, R.; Tabares-Munoz, C.; Jimenez-Lopez, A.; Rodriguez-Castellon, E., Adsorption Kinetics of CO_2, O_2, N_2, and CH_4 in Cation-Exchanged Clinoptilolite. *J. Phys. Chem. B* **2001,** *105*, (7), 1313-1319.

[24] Nair, S.; Tsapatsis, M.; Toby, B. H.; Kuznicki, S. M., A Study of Heat-Treatment Induced Framework Contraction in Strontium-ETS-4 by Powder Neutron Diffraction and Vibrational Spectroscopy. *J. Am. Chem. Soc.* **2001,** *123,* 12781-12790.

[25] Pillai, R. S.; Peter, S. A.; Jasra, R. V., Adsorption of Carbon Dioxide, Methane, Nitrogen, Oxygen and Argon in NaETS-4. *Micropo. Mesopor. Mat.* **2008,** *113,* 268-276.

Chapter 7

Concluding Remarks

7.1 Thesis Contributions

Our results indicate that the nature of extraframework cationic species in ion-exchanged M^{n+}-SAPO-34 greatly affect the sorbents' performance and the saturation adsorption capacity towards light gases. The present work has shown that ion-exchanged M^{n+}-SAPO-34 materials could be promising sorbents for the selective removal of CO_2 at temperatures and pressures that approach ambient conditions. In terms of the CO_2 overall adsorption performance the exchanged materials exhibited the following trend: $Ce^{3+}<Ti^{3+}<Mg^{2+}<Ca^{2+}<Ag^{+}<Na^{+}<Sr^{2+}$. All the M^{n+}-SAPO-34 sorbents studied can be fully regenerated by simple engineering means since the adsorption interactions were in the physisorption range. Strontium(II) exchanged SAPO-34 was by far the best sorbent in the low-pressure region for the selective adsorption of CO_2. The isosteric heat of adsorption data suggested that all the exchanged Sr^{2+} species were exposed to the Chabazite cages and did not provide transport resistance or pore blocking. Binary component adsorption (CO_2/CH_4) simulation data corroborated that, among the sorbents studied, the strontium(II) exchanged ones were by far superior.

The Na^{+}-SAPO-34 uptake data indicate that the particle morphology and, most importantly, polydispersity, play an important role in predicting diffusion coefficients. The results presented in this work confirm that the observed deviations between experimental uptake data and customary phenomenological models may be corrected by considering the shape and size distribution of the particles.

In general, material properties of the titanosilicates, such as surface area and pore size, are highly dependent on the synthesis recipe and post-synthesis treatments. Our results have demonstrated that the titanosilicate UPRM-4d presents a crystalline structure, expanded thermal stability, flexible framework, and considerable surface area. Sr-UPRM-4d presents a higher adsorption capacity than Sr-ETS-4 without missing the selectivity toward molecules of similar kinetic diameters (eg. CO_2, N_2)

Our results have demonstrated that both M^{n+}-SAPO-34 and modified titanium silicates UPRM-4 materials are promising nanoporous sorbents for large and selective adsorption of gas molecules.

7.2 Future Work

In general, ion-exchanged Mn^{+}-SAPO-34 sorbents are promising for light gas mixture separations and more studies will be definitely needed to understand how to functionalize the sorbents pore windows to tailor them for size exclusion capabilities in the 0.2-0.3 Å range. To increase the adsorption capacity and selectivity, it would be desired to optimize the ion exchange methods to increase the concentration of extraframework cations per unit cell. Traditional and advanced ion exchanged techniques, including solid state, using Sr^{2+} and Ba^{2+} cations must be explored.

To correlate and analyze the effect of synthesis and modification methods on the new titanium silicate UPRM-4 materials it is necessary to gather unit cell and framework geometry data. In addition, synthesis conditions of UPRM-4d have much room for improvement and future work should focus on optimization of the synthesis and post-synthesis parameters (e.g. temperature, time, ion exchange).

Appendix A

Na^+-SAPO-34 Binary Ion-Exchange with Divalent Cations

Na^+-SAPO-34 was modified by binary ion exchange using two different exchangeable divalent cations at the same time. The ion-exchanges were performed each in a one step equilibration batch system using a high cation chloride salt/zeolite aqueous solution with an equivalent molar ratio of 10:1 for each cation. Each step was performed under vigorous stirring at 333 K for 24 hours.

A.1 Nitrogen and Methane equilibrium adsorption on Mg/Ca-SAPO-34

A.2 Nitrogen and Methane equilibrium adsorption on Mg/Sr-SAPO-34

A.3 Nitrogen and Methane equilibrium adsorption on Ca/Sr-SAPO-34

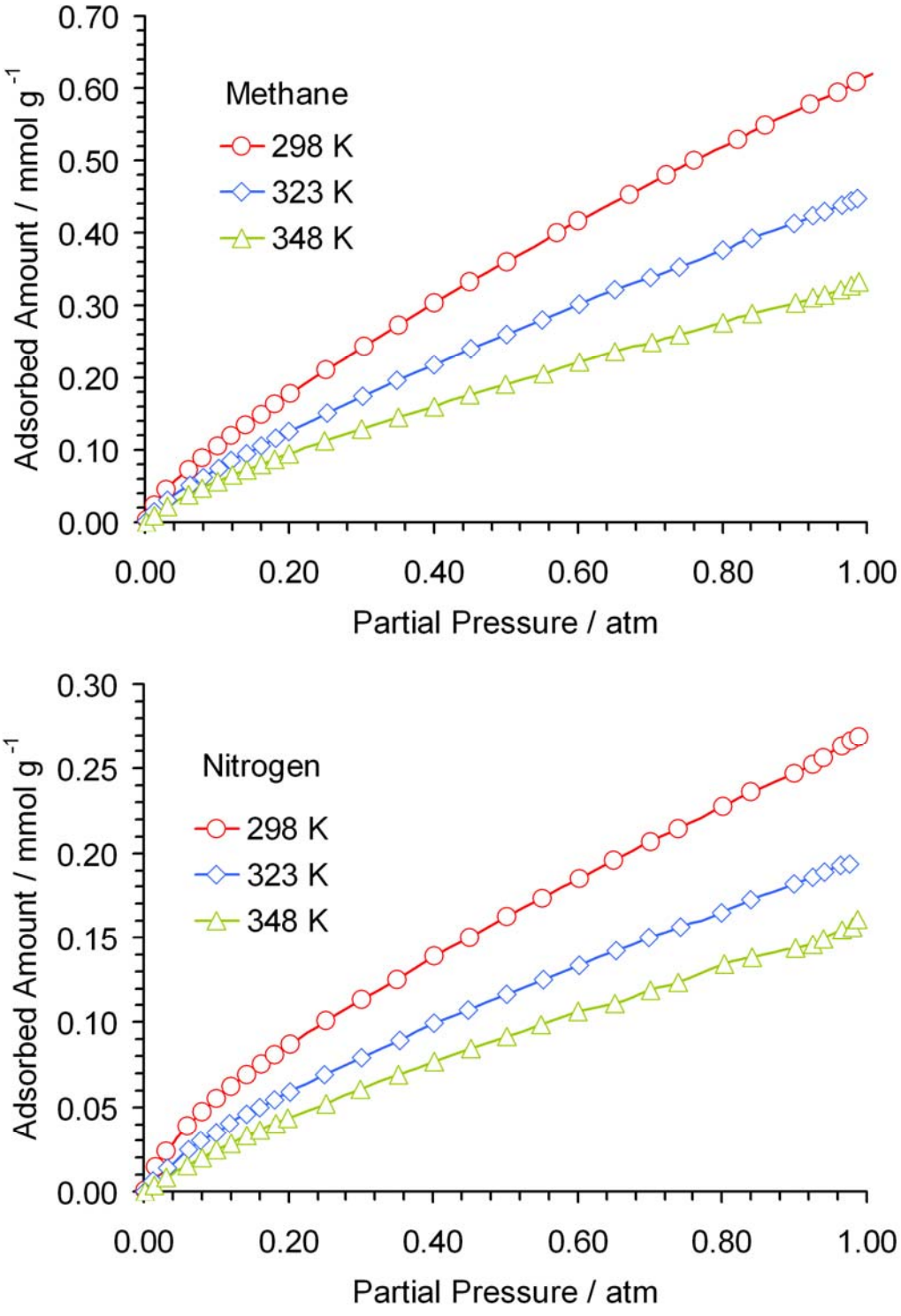

Figure A.1 Adsorption isotherms of nitrogen and methane on ion-exchanged Mg/Ca-SAPO-34 at 298, 323 and 348 K.

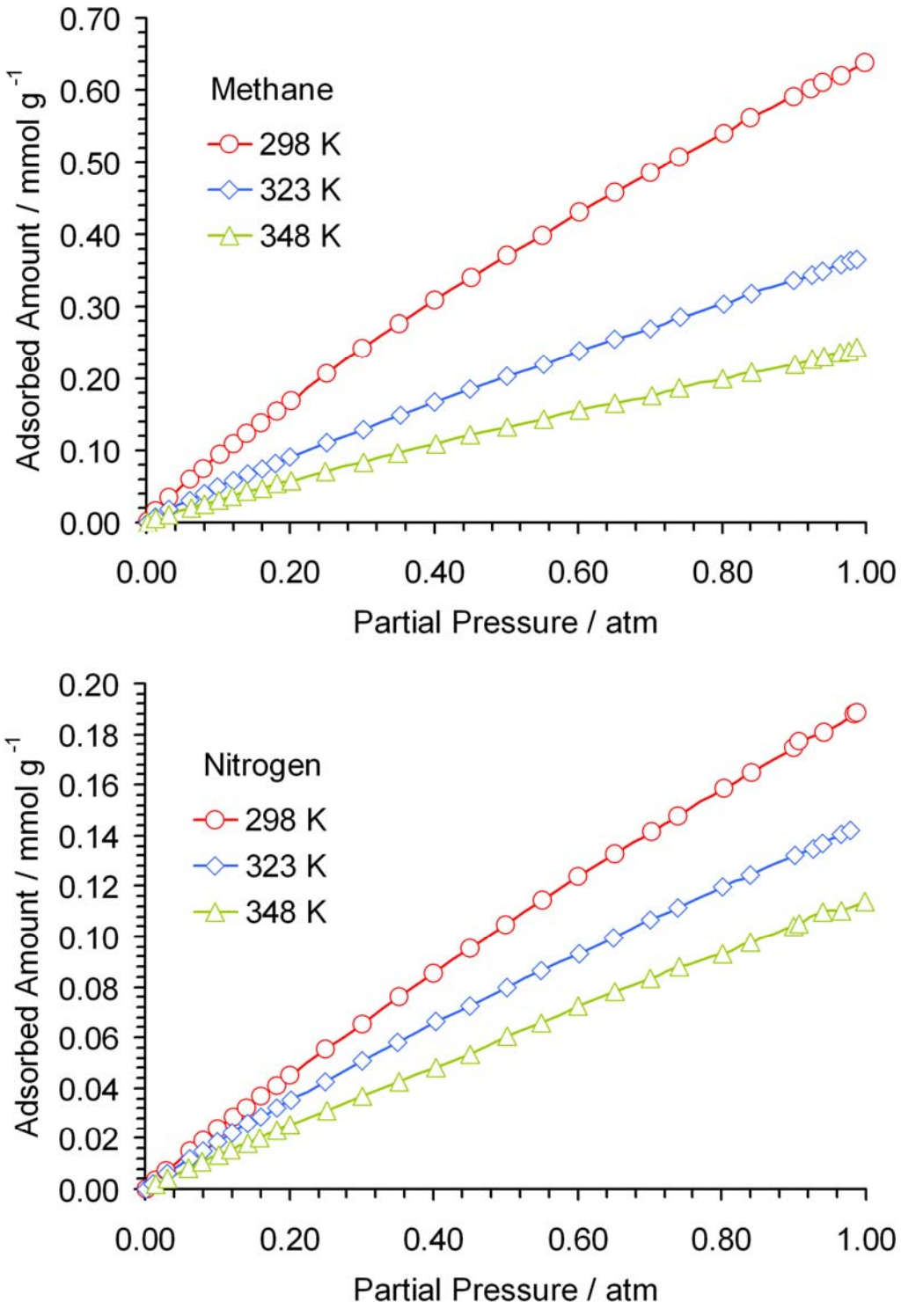

Figure A.2 Adsorption isotherms of nitrogen and methane on ion-exchanged Mg/Sr-SAPO-34 at 298, 323 and 348 K.

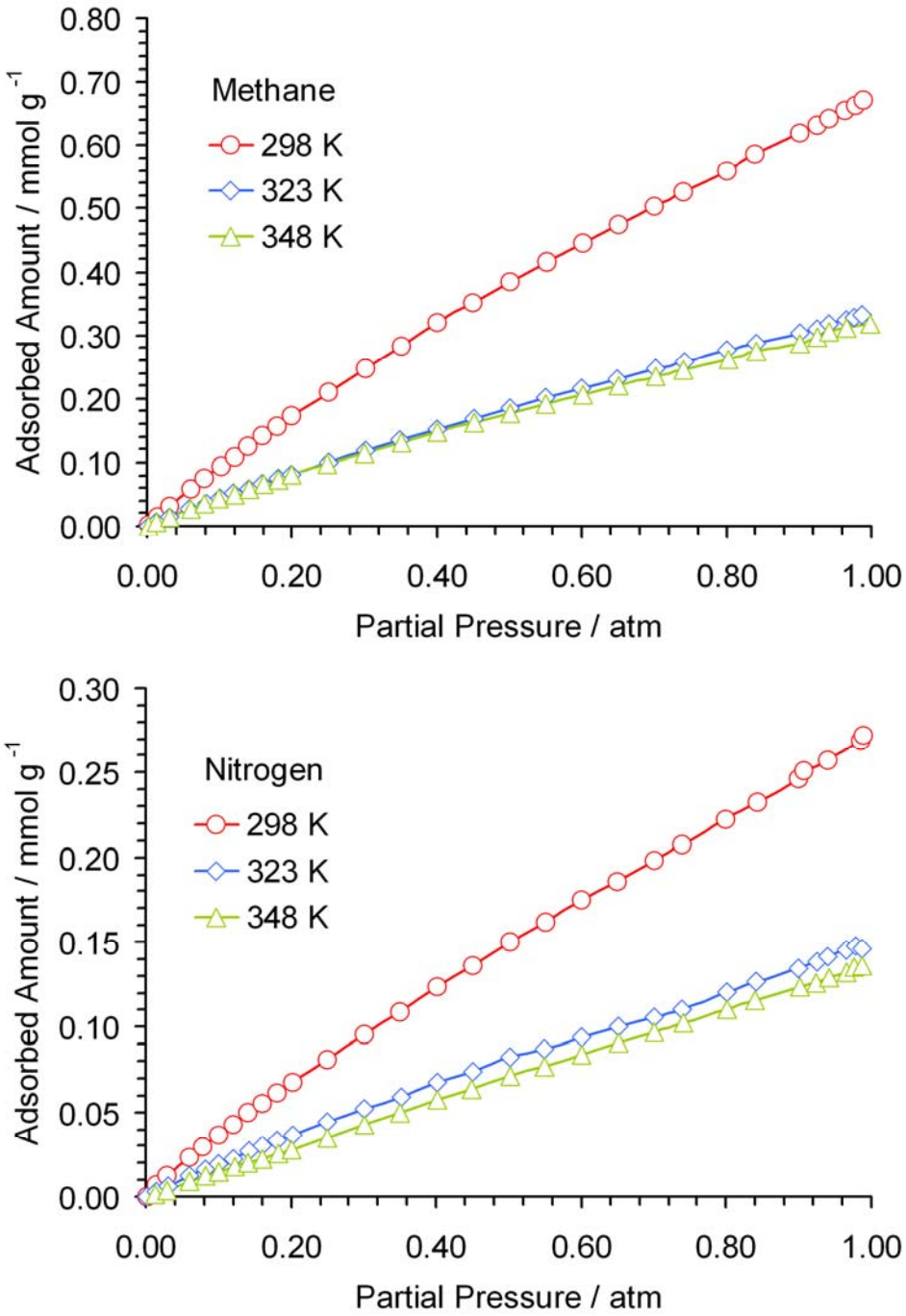

Figure A.3 Adsorption isotherms of nitrogen and methane on ion-exchanged Ca/Sr-SAPO-34 at 298, 323 and 348 K.

Appendix B

LiCl Monolayer Dispersion on Na^+-SAPO-34

The dispersion of a salt or an oxide to a zeolite is a spontaneous process where both cations and anions disperse on the external and/or internal surfaces. Monolayer dispersion on the surface of Na^+SAPO-34 using lithium chloride was performed using 1 gram of the sorbent and 0.034 grams of the salt. A ramp procedure was used at a heating rate of 10 K/min; the mixture was heated 1 hour at 398 K and 24 hour at 457 K in nitrogen at 5 cc/min. In terms of sorption characteristics, the LiCl monolayer dispersed sample adsorbed less nitrogen and methane when compared to the Na^+-SAPO-34 counterparts.

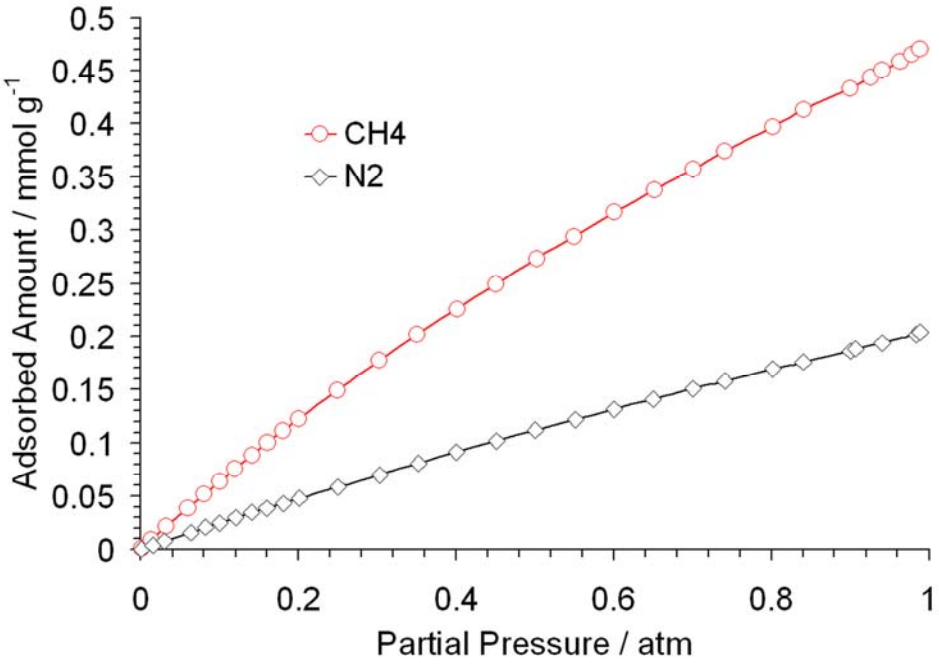

Figure B.1 Adsorption isotherms of nitrogen and methane on LiCl-SAPO-34 at 298 K.

Appendix C

Na^+-SAPO-34 Hydrothermal Synthesis Modification with KOH

Na^+-SAPO-34 is synthesized by hydrothermal crystallization of silicoaluminophosphate gels containing a molecular structure-directing agent. Substituting or adding a different compound to the reacting gel prior to crystallization permits the incorporation of other cations into the framework. K^+-SAPO-34 was synthesized adding KOH instead NaOH into the reacting gel.

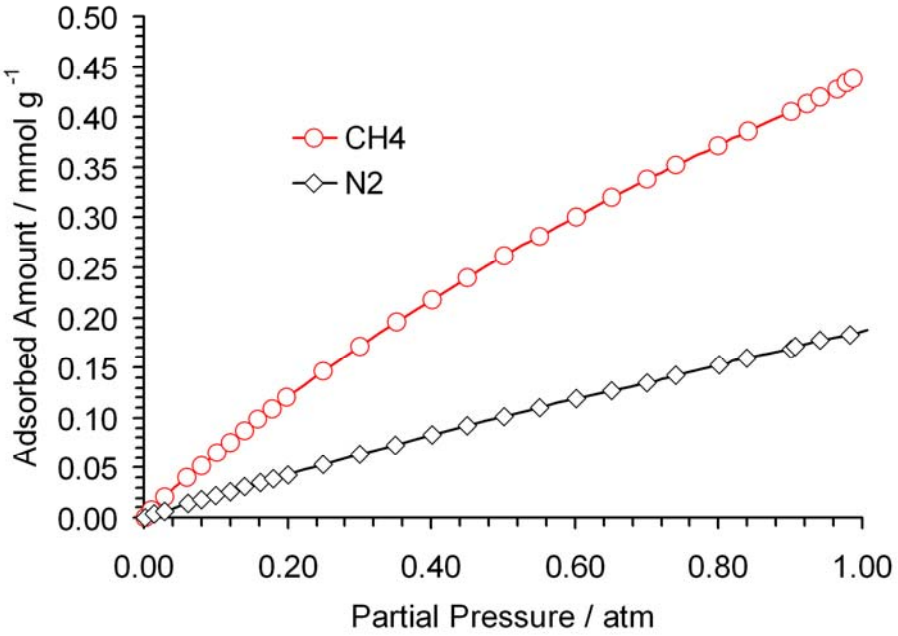

Figure C.1 Adsorption isotherms of nitrogen and methane on K-SAPO-34 at 298 K.

Appendix D

N_2/CH_4 Adsorption Isotherms on Na^+-SAPO-34

During these experiments, the initial adsorbed gas (N_2 or CH_4) was changed to the other at a partial pressure of ~ 0.3 atm. The isotherms show that neither of the adsorbed gas produces a blockage of the pore windows, permitting the access of other molecules into the cages of the structure.

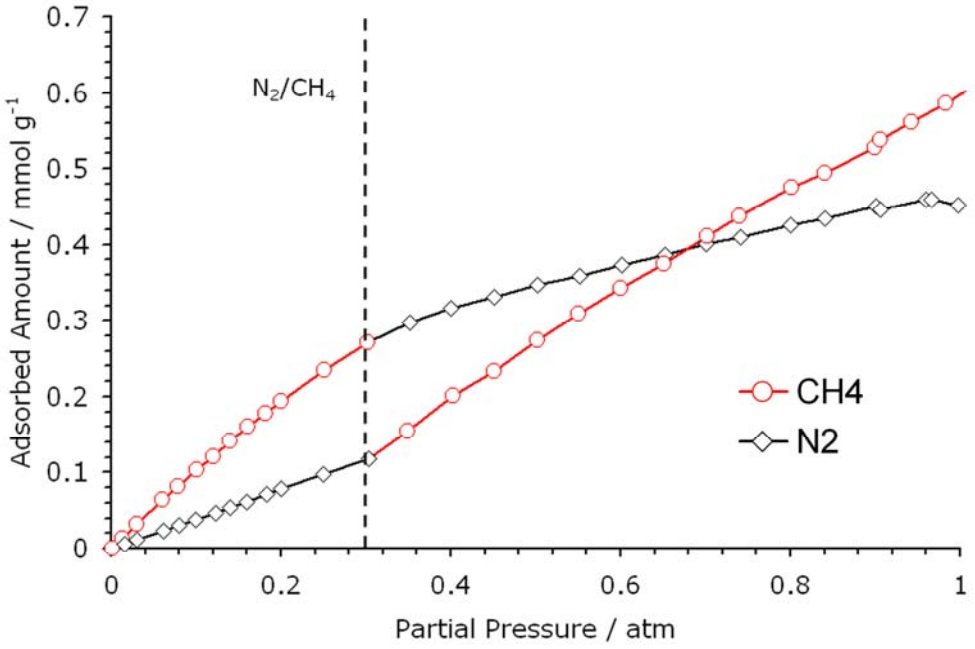

Figure D.1 Adsorption isotherms of N_2/CH_4 on K-SAPO-34 at 298 K.

Appendix E

CO_2 Adsorption and Desorption on Sr^{2+}-SAPO-34

Our data indicates that besides the strong CO_2 interaction, the heat of adsorption correlates to physical and reversible adsorption type. Figure B.1 shows data for the adsorption and desorption of carbon dioxide in Sr^{2+}-SAPO-34 at 273K after increasing and decreasing the CO_2 partial pressure. We understand that with a vacuum pressure swing adsorption process our materials could be used for natural gas purification applications.

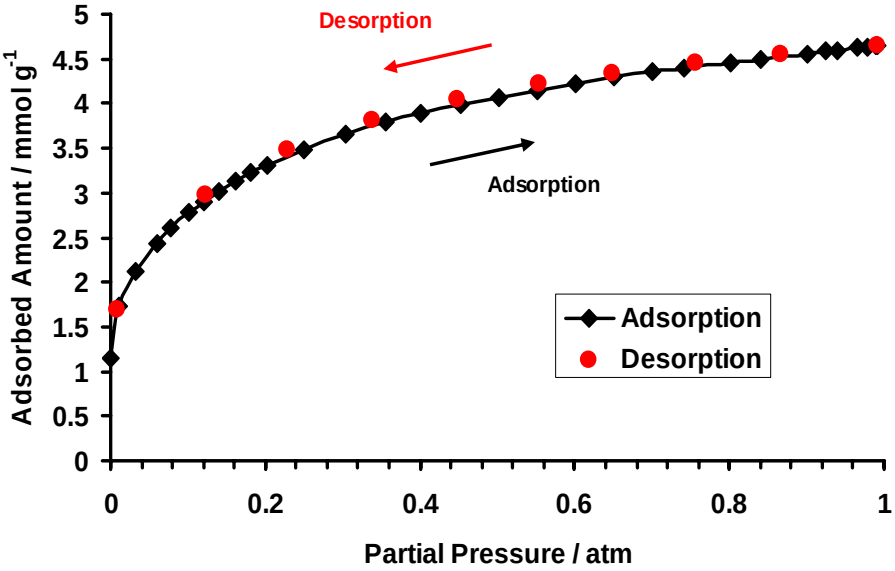

Figure E.1 Adsorption isotherms of CO_2 on Sr^{2+}-SAPO-34 at 273 K.

Appendix F

Cubic Phenomenological Model Derivation

Conservation equation in rectangular coordinates for diffusion in a cube:

$$\left(\frac{\partial^2 C}{\partial x^2}+\frac{\partial^2 C}{\partial y^2}+\frac{\partial^2 C}{\partial z^2}\right)D=\frac{\partial C}{\partial t}$$

$$X=\frac{x}{L} \quad dx=LdX \quad dx^2=LdX^2$$

$$\theta=\frac{C_A}{C_o} \quad dC_A=C_o d\theta \quad dC_A{}^2=C_o d\theta^2$$

$$\left(\frac{C_o\partial^2\theta}{L\partial X^2}+\frac{C_o\partial^2\theta}{L\partial Y^2}+\frac{C_o\partial^2\theta}{L\partial Z^2}\right)D=\frac{C_o\partial\theta}{\partial t}$$

$$\tau=\frac{tD}{L^2} \quad dt=\frac{L^2}{D}d\tau$$

$$\left(\frac{\partial^2\theta}{\partial X^2}+\frac{\partial^2\theta}{\partial Y^2}+\frac{\partial^2\theta}{\partial Z^2}\right)=\frac{\partial\theta}{\partial\tau}$$

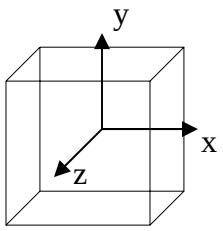

Using boundary conditions presented in table 2-7 and the Finite Fourier Transform (FFT method:

$$\Phi_n(X)=\sqrt{4}\cos\left[2\left(n+\tfrac{1}{2}\right)\pi X\right]$$
$$\Psi_m(Y)=\sqrt{4}\cos\left[2\left(m+\tfrac{1}{2}\right)\pi Y\right]$$
$$\mathrm{B}_p(Z)=\sqrt{4}\cos\left[2\left(p+\tfrac{1}{2}\right)\pi Z\right]$$

$$\theta_n(\tau,Y,Z)=\int_0^{1/2}\Phi_n(x)\,\theta(X,Y,Z,\tau)dX$$

$$\theta(X,Y,Z,\tau)=\sum_{n=1}^{\infty}\theta_n(Y,Z,\tau)\Phi_n(x)$$

$$\theta_{nm}(\tau,Z)=\int_0^{1/2}\int_0^{1/2}\Phi_n(X)\,\Psi_m(Y)\,\theta(X,Y,Z,\tau)dX\;dY$$

$$\theta(X,Y,Z,\tau)=\sum_{n=1}^{\infty}\sum_{m=1}^{\infty}\theta_{nm}(Z,\tau)\Phi_n(x)\Psi_m(Y)$$

$$\theta_{nmp}(\tau)=\int_0^{1/2}\int_0^{1/2}\int_0^{1/2}\Phi_n(X)\,\Psi_m(Y)\,\mathrm{B}_p(Z)\,\theta(X,Y,Z,\tau)dX\;dY\;dZ$$

The solution is therefore expressed as

$$\theta(X,Y,Z,\tau)=\sum_{n=1}^{\infty}\sum_{m=1}^{\infty}\sum_{p=1}^{\infty}\theta_{nmp}(\tau)\Phi_n(x)\Psi_m(Y)\mathrm{B}(Z)$$

Transforming the differential equation:

$$\int_0^{1/2}\int_0^{1/2}\int_0^{1/2}\Phi_n(X)\,\Psi_m(Y)\,\mathrm{B}_p(Z)\,\theta(X,Y,Z,\tau)dX\;dY\;dZ=$$

$$\frac{2\sqrt{4}}{\pi}\frac{\left(n+1/2\right)}{\left(m+1/2\right)\left(p+1/2\right)}(-1)^n(-1)^m(-1)^p-4\left(n+1/2\right)^2\pi^2\theta_{nmp}$$

$$+\frac{2\sqrt{4}}{\pi}\frac{\left(m+1/2\right)}{\left(n+1/2\right)\left(p+1/2\right)}(-1)^n(-1)^m(-1)^p-4\left(m+1/2\right)^2\pi^2\theta_{nmp}$$

$$+\frac{2\sqrt{4}}{\pi}\frac{\left(p+1/2\right)}{\left(n+1/2\right)\left(m+1/2\right)}(-1)^n(-1)^m(-1)^p-4\left(p+1/2\right)^2\pi^2\theta_{nmp}$$

The partial differential equation reduces to:

$$\frac{d\theta_{nmp}}{d\tau}=(-1)^{n+m+p}\frac{4}{\pi}\left[\frac{\left(n+1/2\right)^2+\left(m+1/2\right)^2+\left(p+1/2\right)^2}{\left(n+1/2\right)\left(m+1/2\right)\left(p+1/2\right)^2}\right]$$

$$-4\pi^2\left[\left(n+1/2\right)^2+\left(m+1/2\right)^2+\left(p+1/2\right)^2\right]\theta_{nmp}$$

The solution to the above equation is:

$$\theta_{nmp} = \frac{(-1)^{n+m+p}}{\pi^3}\left[\frac{1}{\left(n+\frac{1}{2}\right)\left(m+\frac{1}{2}\right)\left(p+\frac{1}{2}\right)^2}\right]\left\{1-\exp\left(-4\pi^2\tau\left[\left(n+\frac{1}{2}\right)^2+\left(m+\frac{1}{2}\right)^2+\left(p+\frac{1}{2}\right)^2\right]\right)\right\}$$

The concentration is therefore given by:

$$\theta(X,Y,Z,\tau) = 1-\frac{8}{\pi^3}\sum_{n=0}^{\infty}\sum_{m=0}^{\infty}\sum_{p=0}^{\infty}\left[(-1)^{n+m+p}\frac{\cos\left[2\left(n+\frac{1}{2}\right)\pi X\right]\cos\left[2\left(m+\frac{1}{2}\right)\pi Y\right]\cos\left[2\left(p+\frac{1}{2}\right)\pi Z\right]}{\left(n+\frac{1}{2}\right)\left(m+\frac{1}{2}\right)\left(p+\frac{1}{2}\right)^2}\right]*$$
$$\left\{\exp\left(-4\pi^2\tau\left[\left(n+\frac{1}{2}\right)^2+\left(m+\frac{1}{2}\right)^2+\left(p+\frac{1}{2}\right)^2\right]\right)\right\}$$

The total mass inside the cube, as a function of time is given by:

$$\begin{aligned}M(t) &= 8\int_0^{1/2}\int_0^{1/2}\int_0^{1/2} C(t,x,y,z)\,dx\,dy\,dz \\ &= 8C_oL^3\int_0^{1/2}\int_0^{1/2}\int_0^{1/2}\theta(\tau,X,Y,Z)\,dX\,dY\,dZ \\ &= C_oL^3\left(1-\frac{8}{\pi^6}\sum_{n=0}^{\infty}\sum_{m=0}^{\infty}\sum_{p=0}^{\infty}\frac{\exp\left\{-4\left[\left(n+\frac{1}{2}\right)^2+\left(m+\frac{1}{2}\right)^2+\left(p+\frac{1}{2}\right)^2\right]\pi^2\frac{Dt}{L^2}\right\}}{\left(n+\frac{1}{2}\right)^2\left(m+\frac{1}{2}\right)^2\left(p+\frac{1}{2}\right)^2}\right)\end{aligned}$$

For the fractional uptake ($M_t=C_0L^3$):

$$F = \frac{M(t)}{M_t} = 1-\frac{8}{\pi^6}\sum_{n=0}^{\infty}\sum_{m=0}^{\infty}\sum_{p=0}^{\infty}\frac{\exp\left\{-4\left[\left(n+\frac{1}{2}\right)^2+\left(m+\frac{1}{2}\right)^2+\left(p+\frac{1}{2}\right)^2\right]\pi^2\frac{Dt}{L^2}\right\}}{\left(n+\frac{1}{2}\right)^2\left(m+\frac{1}{2}\right)^2\left(p+\frac{1}{2}\right)^2}$$

Appendix G

MATLAB Algorithms

G.1 Fractional Uptake for Cubic Crystals

G.2 CH_4/CO_2 Vacuum Pressure Swing Adsorption

G.3 Adsorption Kinetics with Langmuir-Freundlich Isotherm

G.1 Fractional Uptake for Cubic Crystals

```
%+++++++++++++++++++++++++++++++++++++++++++++++++++++++++++++++++++++++++++++++
%              PROGRAM NAME: SAPO8 (MatLab version 7.0)
%              FRACTIONAL UPTAKE FOR CUBIC CRYSTALS
%
%              Written by M. E. Rivera
%               Department of Chemical Engineering
%               University of Puerto Rico, Mayaguez, PR
%
%+++++++++++++++++++++++++++++++++++++++++++++++++++++++++++++++++++++++++++++++
%              This is the basic problem of solving the problem of adsorption
%              kinetics in a cubic crystal.
%+++++++++++++++++++++++++++++++++++++++++++++++++++++++++++++++++++++++++++++++

D=0.0025

for t=1:100;

   sum=0;
   sum2=0;
   sum3=0;

   for n=1:50;

      sum=0;
      sum2=0;

      for m=1:50;

         sum=0;


         for p=1:50;

            f(n,m,p)=(exp(-4*(((n-.5)^2)+((m-.5)^2)+((p-.5)^2))*(pi^2)*(t-1+0)*D))/(((n-.5)^2)*((m-
               .5)^2)*((p-.5)^2));

            sum=sum+f(n,m,p);

         end

      sum2=sum2+sum;

      end

   sum3=sum3+sum2;

   end

   F=1-(8/(pi^6))*(sum3);
   disp (F)
   F1(t)= F; t1(t)=t;

end

% THIS IS THE END OF THIS PROGRAM
```

G.2 CH_4/CO_2 Vacuum Pressure Swing Adsorption

```
%+++++++++++++++++++++++++++++++++++++++++++++++++++++++++++++++++++++++++++++++
%       PROGRAM NAME: Main_SAPsim (MatLab version 7.0)
%       CH4/CO2 VACCUUM PRESSURE SWING ADSORBTION FOR Na, Ag and Sr SAPO-34
%
%   Written by M. E. Rivera and G. J. Ruiz
%               Department of Chemical Engineering
%               University of Puerto Rico, Mayaguez, PR
%
%+++++++++++++++++++++++++++++++++++++++++++++++++++++++++++++++++++++++++++++++
%               This is the basic problem of solving the problem of CO2 in CH4 mixture.
%+++++++++++++++++++++++++++++++++++++++++++++++++++++++++++++++++++++++++++++++


function main_SAPsim

clear all
clc;
format long;
%Order components:[CO2;CH4]
nc=2;
T=298;                              %[=]K
P0=101325;                          %[=]Pa, initial pressure for each batch
Rg=8.314;                           %[=]J/(mol*K)
dentP=1.06e3;                       %[=]kg/m^3
epsilon=0.348;                      %bed void
b=[0.498815;0.224964]/101325;       %[=]Pa^-1               Sr-SAPO-34
n=[2.8392;1.8927];                  %heterogeneity factor   Sr-SAPO-34
q_sat=[6.7071;2.203382];            %[=]mol/kg              Sr-SAPO-34
%b=[2.989396;0.412294]/101325;      %[=]Pa^-1               Na-SAPO-34
%n=[1.8171;1.0000];                 %heterogeneity factor   Na-SAPO-34
%q_sat=[5.263648;2.126816];         %[=]mol/kg              Na-SAPO-34
%b=[2.950939;0.660200]/101325;      %[=]Pa^-1               Ag-SAPO-34
%n=[1.3844;1.1043];                 %heterogeneity factor   Ag-SAPO-34
%q_sat=[4.879246;1.654500];         %[=]mol/kg              Ag-SAPO-34

MW=[44;16];                         %[=]kg/mol
WM_CH4=16;                          %[=]kg/mol
WM_CO2=44;                          %[=]kg/mol
Dv_CH4=25.14;                       %diffusion volume
Dv_CO2=26.7;                        %diffusion volume
D_pore=4e-10;                       %[=]m
ep_particle=0.38;                   %particle porosity
t_particle=4.5;                     %particle tortuosity
R=0.6e-6;                           %[m]
Do=[0.005643;0.021594];             %diffusion time constant @ 0 coverage [1/s]     Sr-SAPO-34
%Do=[0.006544;0.021451];            %diffusion time constant @ 0 coverage [1/s]     Na-SAPO-34
%Do=[0.007773;0.027414];            %diffusion time constant @ 0 coverage [1/s]     Ag-SAPO-34
landa=[10.6;18.8];                  %ratio of rate constant                         Sr-SAPO-34
%landa=[13.8;22.9];                 %ratio of rate constant                         Na-SAPO-34
%landa=[18.9;17.3];                 %ratio of rate constant                         Ag-SAPO-34

save constant_SAP.mat nc T Rg dentP epsilon b n q_sat MW WM_CH4 WM_CO2 Dv_CH4 Dv_CO2
        D_pore ep_particle t_particle R Do landa
```

```
%%%%%%%%%%%%%%%%%%%%%%%%%%%%%%%%%%%%%%%%%%%%%%%%%%%%
%%%%INITIAL CONDITIONS
x0=[P0;0.05;0.95;0.0;0.0];              % @ t=0: P=1 atm, y_CO2=0.2, y CH4=0.8
tspan=[0 1];                             % t0 to t_end

count=0;
total_time=0;
while x0(3)<=0.999999;
[t,x]=ode45(@ODESAP,tspan,x0);

%x0=x(end,

solution=x;
rowcol=size(solution);
sindya=0;
for k=1:rowcol(1)
    prueva(k)=isreal(solution(k,1));
    if prueva(k)==1
        sindya=sindya+1;
    end
end
Mnew=solution(1:sindya,:);
P(1,1)=Mnew(end,1);
P(2,1)=P0;
Vol=100;                         %[=]m^3
n_tot=P*Vol/(Rg*T);                 %[=]mol
n_fin=diff(n_tot);
n_CH4add=n_fin*x0(3);
y_CH4new=(n_tot(1)+n_CH4add)/n_tot(2);
y_CO2new=1-y_CH4new;
x0=[P0;y_CO2new;y_CH4new;Mnew(end,2+nc:end)'];
count=count+1
total_time=t(sindya)+total_time
end
x0
f=x0(4)/x0(5)


%%%%%%%%%%%%%%%%%%%%%%%%%%%%%%%%%%%%%%%%%%%%%%%%%%%%
%%%%ODESAP FUNCTION

function DxDt=ODESAP(t,x)

load constant_SAP       %nc,T,Rg,dentP,epsilon,b,n,q_sat & F_uptake from main_SAPsim.m file

P=x(1);
y=x(2:nc+1);
P_part=y*P;
q=x(nc+2:2*nc+1);

%DK=48.5*D_pore*(T./MW);

DK=((Do.*R^2).*(1-(q./q_sat)+(landa./2).*(q./q_sat).*(2-(q./q_sat))+(1-landa).*(1-
                landa).*(landa/2).*(q./q_sat).^2)./(1-(q./q_sat)+landa.*(q./q_sat)/2).^2);
```

```
DM=((100)*T^1.75*((WM_CH4+WM_CO2)/(WM_CH4*WM_CO2))^(1/2))/(P*(Dv_CH4^(1/3)+Dv_CO
        2^(1/3))^2);
De=(ep_particle/t_particle)*DK*DM./(DK+DM);

qE=q_sat.*((b.*P_part).^(1./n))./(1+sum((b.*P_part).^(1./n)));

%%%%%%%%%%%%%%%%%%%%%%%%%%%%%%%%%%%%%%%%%%%%%%%%%%%%%%%%%%%%%%%%%%%%%%%

%%%%ODE SYSTEM

DxDt(1)=-dentP*Rg*T*((1-epsilon)/epsilon)*sum(15*(De./R^2).*(qE-q));
DxDt(2:nc+1,1)=-dentP*Rg*T*((1-epsilon)/epsilon)/P*((15*(De./R^2).*(qE-q))-
        y.*sum(15*(De./R^2).*(qE-q)));
DxDt(nc+2:2*nc+1)=15*(De./R^2).*(qE-q);

%
% THIS IS THE END OF THIS PROGRAM
```

G.3 Adsorption Kinetics with Langmuir-Freundlich Isotherm

```
%+++++++++++++++++++++++++++++++++++++++++++++++++++++++++++++++++++++++++++++++

%           PROGRAM NAME: ADSORB1C_LF.M (MatLab version 5.2)
%           SINGLE COMPONENT ADSORPTION KINETICS IN A SINGLE CRYSTAL
%           WITH LANGMUIR-FREUNDLICH ISOTHERM
%           Written by    D. D. Do
%                                       Department of Chemical Engineering
%                                       University of Queensland, St. Lucia, Qld 4072, Australia
%  Revised by M. E. Rivera
%           Department of Chemical Engineering
%           University of Puerto Rico, Mayaguez, PR
%
%+++++++++++++++++++++++++++++++++++++++++++++++++++++++++++++++++++++++++++++++
%                                       This is the basic problem of solving the problem of adsorption
%                                       kinetics in a single Crystal with the LANGMUIR-
                                        FREUNDLICH isotherm.
%
%                                       Ref: D.D.Do, "Adsorption Analysis: Equilibria and Kinetics"
%                                                                                   Chapter 10, eqs.
          (10.2-38), Appendix 10.1
%
%               Date written: 2 October 1996
%               Date revised: 1 April 1998:         Conversion to MatLab 5.2
%               Date revised: 24 October 2008:      Conversion from LANGMUIR to LANGMUIR-
                                                    FRENDLICH isotherm
%+++++++++++++++++++++++++++++++++++++++++++++++++++++++++++++++++++++++++++++++
          +
% NOMENCLATURE:
%
%           A           : First derivative collocation matrix
%           al          : Parameter alpha for Jacobi polynomial
%           b           : 1/atm       : Affinity constant in the isotherm equation
%           B           : Second derivative collocation matrix
%           be          : Parameter beta for Jacobi polynomial
%           C           : Matrix defined as: 4*u(i)*b(i,j)+2*(s+1)*a(i,j)
%           cmu         : mmole/g     : Concentration of the adsorbed species
%           cmui        : mmole/g     : Initial adsorbed concentration in equilibrium with Pi
%           cmub        : mmole/g     : Final adsorbed concentration in equilibrium with Pb
%           cmus        : mmole/g     : Saturation adsorbed concentration
%           cmu_mean    : mmole/g     : mean adsorbed concentration
%           D0mu        : cm^2/sec    : Corrected diffusivity
%           fractional_uptake         : Fractional uptake
%           h                         : Heterogeneity Factor
%           lambdab     : Nondimensional affinity at bulk condition (= b*Pb)
%           lambdai     : Nondimensional affinity at initial condition (= b*Pi)
%           n           : Number of interior collocation points
%           n0          : = 1 if the point x=0 is counted; otherwise =0
%           n1          : = 1 if the point x=1 is counted; otherwise =0
%           nt          : n + n0 + n1
%           omega       : integration vector
%           omega0      : initial integration vector
%           Pb          : atm         : Bulk pressure
%           Pi          : atm         : Initial pressure
```

```
%           R           : cm          : Micro-particle radius for cyl. and sphere, half length for slab
%           s           : Particle shape factor (0 for slab, 1 for cylinder, 2 for sphere)
%           t, tout     : nondimensional time
%           time        : sec               : time
%           t_initial   : Nondimensional initial time (usually 0)
%           t_final     : Final nondimensional time
%           u           : Interpolation points = x^2
%           x           : Nondimensional distance (=r/R)
%           y           : Nondimensional concentration
%           ynp1        : Nondimensional concentration at surface (x=1)
%           w           : Radau quadrature weight
%
%+++++++++++++++++++++++++++++++++++++++++++++++++++++++++++++++++++++++
% USAGE:
%           Type ADSORB1C_LF
%+++++++++++++++++++++++++++++++++++++++++++++++++++++++++++++++++++++++
           clear all
           clc

% DECLARE SOME GLOBAL VARIABLES
           global n u A B C                          % Collocation vectors and matrices
           global R s                                % Particle characteristics
           global b cmus                             % Isotherm characteristics
           global Pb Pi                              % Pressures of free species
           global lambdab lambdai
           global cmub cmui                          % Concentrations of adsorbed species
           global D0mu                               % Diffusion characteristics

           half_time   = [0.19674 0.0631 0.03055];

%---------------------------------------------------------------------
% USER SUPPLY SECTION
           s                         = 0;            % micro-particle shape factor
           R                         = 2.6e-5;       % micro-particle radius (cm)
           Pi                        = 0;            % initial gas pressure (atm)
           Pb                        = 0.1;          % bulk gas pressure (atm)
           b                         = 2.989;        % adsorption affinity (1/atm)
           h          = 1.817;                        % heteroheneity factor
  cmus                   = 5.264;                    % maximum adsorption capacity (mmole/g)
           D0mu                      = 0.2e-10;                                    %
           corrected diffusivity (cm^2/sec)
           t_initial     = 0;              % initial time for integration
  t_final          = 10*half_time(s+1);    % You may set your own final time here!!
%---------------------------------------------------------------------

% COLLOCATION SECTION
           n                         = 5;
           n0                        = 0;
           n1                        = 1;
           al                        = 1;
           be                        = (s-1)/2;
            nt                       = n + n0 + n1;
           A                         = zeros(nt);
           B                         = zeros(nt);
           C                         = zeros(nt);
           [dif,u]                   = JCRoot(n,n0,n1,al,be);
```

```
            A                               = AB(n,n0,n1,1,dif,u);
            B                               = AB(n,n0,n1,2,dif,u);
            w                               = RDW(n,n0,n1,al-1,be,u,dif);
            for i=1:nt;
             C(i,:)         = 4.*u(i).*B(i,:)+2.*(s+1).*A(i,:);
            end

% CHECK FOR THE SYSTEM ADSORPTION AFFINITY
            lambdab                 = (b*Pb)^(1/h);
            lambdai                 = (b*Pi)^(1/h);
            if lambdab > 50 | lambdai > 50
                disp(['The adsorption affinity is too high.'  ...
                                'You might have problem with the convergence'])
            end

% CALCULATIONS OF PARAMETERS FROM INPUTS
            cmui                            = cmus*((b*Pi)^(1/h))/(1+((b*Pi)^(1/h)));
            cmub                            = cmus*((b*Pb)^(1/h))/(1+((b*Pb)^(1/h)));

% CALL ODE SOLVER
            omega0                          = zeros(n,1);
            options                         = odeset('Reltol', 1e-2, 'Abstol', 1e-5, 'bdf', 'off');
            [tout,omega] = ode15s('fads3',[t_initial t_final], omega0, options);

%-------------------------------------------------------
% SOLUTIONS: CONCENTRATION PROFILES & FRACTIONAL UPTAKE
%-------------------------------------------------------
            time                            = tout.*R.^2./D0mu
            ynp1                                    = ones(length(tout),1);
            y                                       = [omega ynp1];

            for i=1:length(tout)
                cmu(i,:)                                        = y(i,:)*(cmub - cmui) + cmui;
                cmu_mean(i)                                     = dot( w, cmu(i,:) );
                fractional_uptake(i)    = dot( w, y(i,:) )

  end

%----------
% PLOTTING
%----------
            figure(1)
            subplot(2,2,1)
            plot(time,y,'r-');
            xlabel('time (sec)');
            ylabel('y');
            grid;
            title('Dimensionless Adsorbed Conc. vs. time');
            hold on;

            subplot(2,2,2)
            plot(time,fractional_uptake,'b-');
            xlabel('time (sec)');
            ylabel('Fractional uptake');
            grid;
            title('Fractional Uptake vs. time');
```

```
subplot(2,2,3)
plot(time,1000*cmu_mean,'r-');
xlabel('time (sec)');
ylabel('Average Adsorbed Conc. (mmole/cc)');
grid;
title('Average Adsorbed Conc. vs. Time');

subplot(2,2,4)
dt = floor(length(tout)/10);
for i=1:dt:length(tout)
    plot(sqrt(u),y(i,:),'r-',sqrt(u),y(i,:),'bo');
    hold on
end
xlabel('Nondimensional distance');
ylabel('Nondimensional Adsorbed Conc.');
grid;
title('Dimensionless Adsorbed Conc. Profiles');


%
% THIS IS THE END OF THIS PROGRAM
```

Appendix H

UPRM-4 Characterization

The as-synthesized materials were characterized by X-ray powder diffraction (XRD), and thermo gravimetric analyzer (TGA). XRD patterns were obtained using a Rigaku Ultima3 Theta-Theta Goniometer with continuous scanning rate. TGA analyses were performed in a TA Q500 with air at 100 cc/min and a heating rate of 5 °C/min. Synchrotron X-ray powder diffraction experiments were performed at the beamline 11-BM of the Advanced Photon Source (APS) at Argonne National Laboratory. Sr-UPRM-4h equilibrium isotherms were obtained using a ultra-high vacuum static volumetric adsorption system (Micromeritics ASAP 2020).

H.1 XRD patterns of UPRM-4 materials

H.2 TGA data for UPRM-4b, UPRM-4c, and UPRM-4e

H.3 TGA data for UPRM-4f, and UPRM-4g

H.4 Adsorption isotherms on Sr-UPRM-4h

H.5 Adsorption isotherms on Sr-UPRM-4h

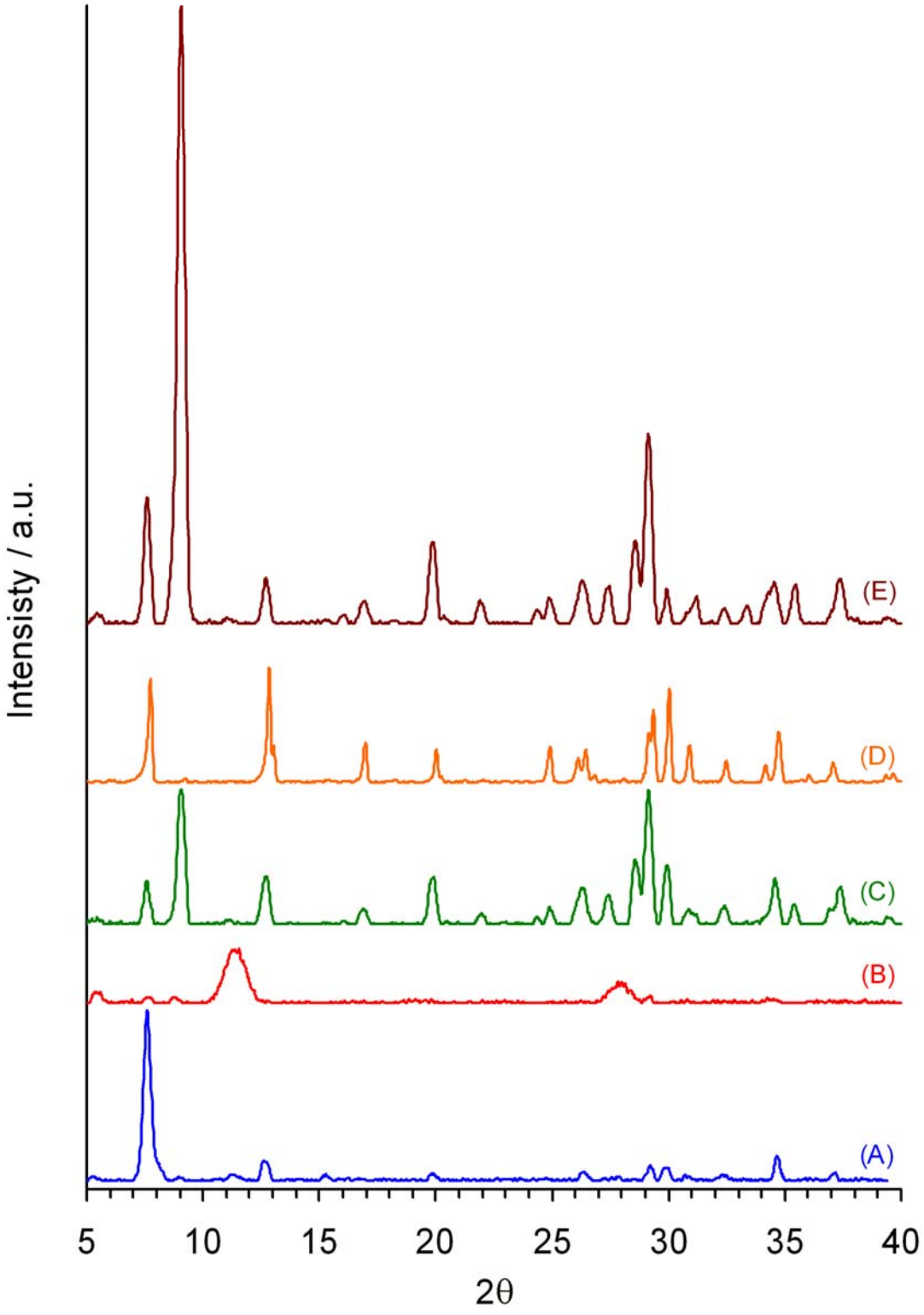

Figure H.1 XRD patterns of (A) UPRM-4b, (B) UPRM-4c, (C) UPRM-4e, (D)UPRM-4k,and (E)UPRM-4f.

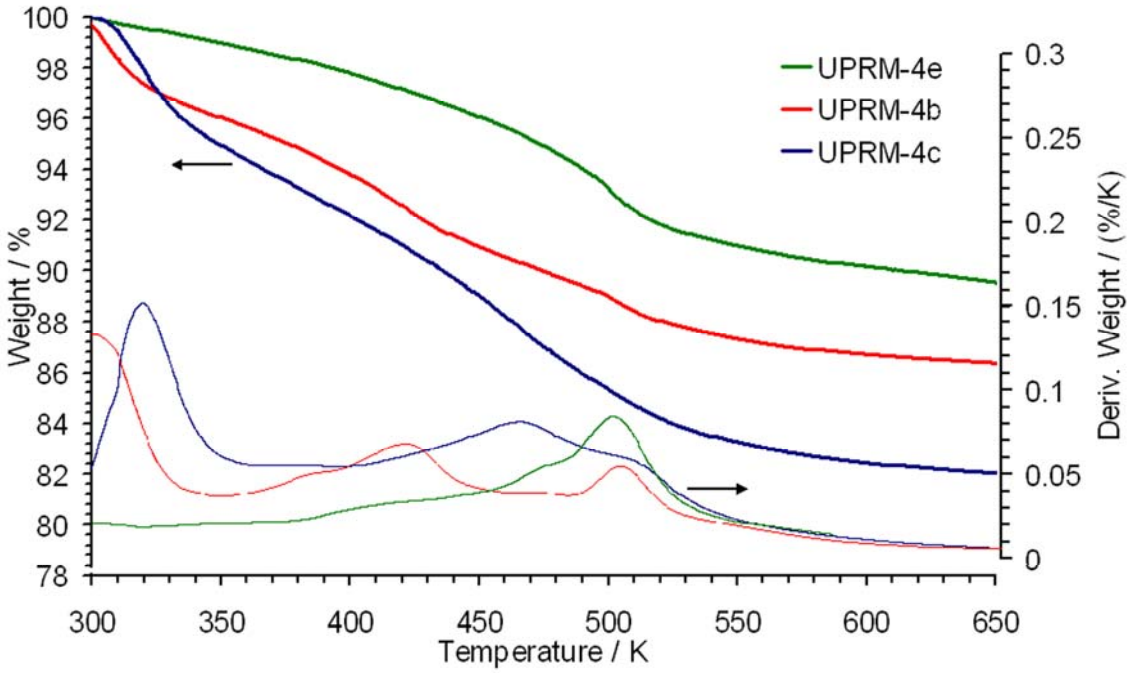

Figure H.2 TGA data for UPRM-4b, UPRM-4c, and UPRM-4e.

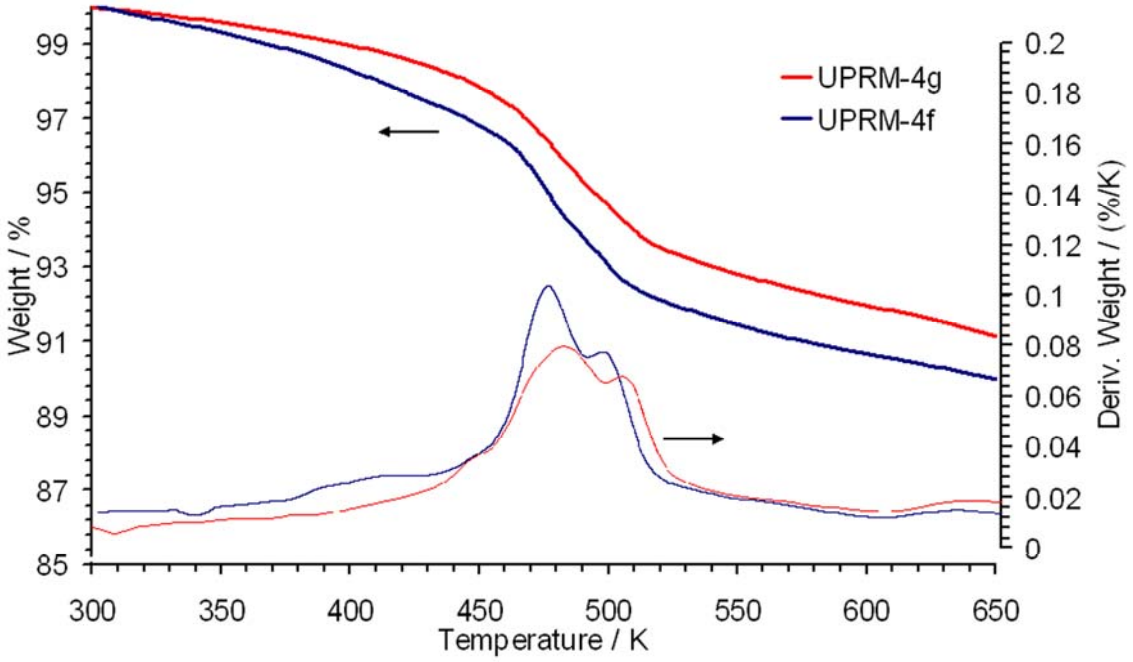

Figure H.3 TGA data for UPRM-4f, and UPRM-4g.

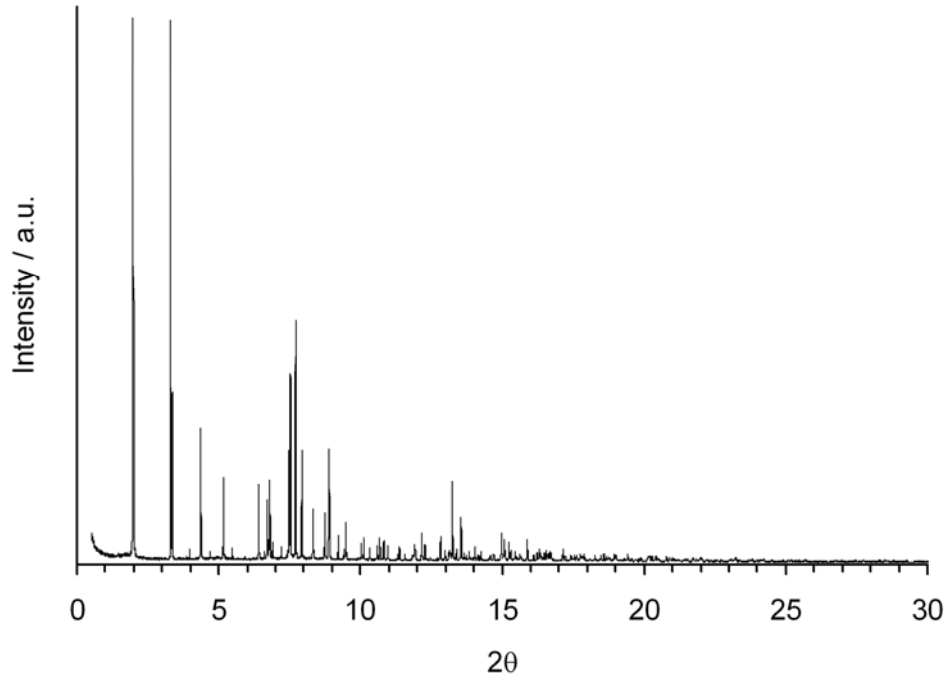

Figure H.4 Synchrotron XRD patterns of as-synthesized TEA-UPRM-4h.

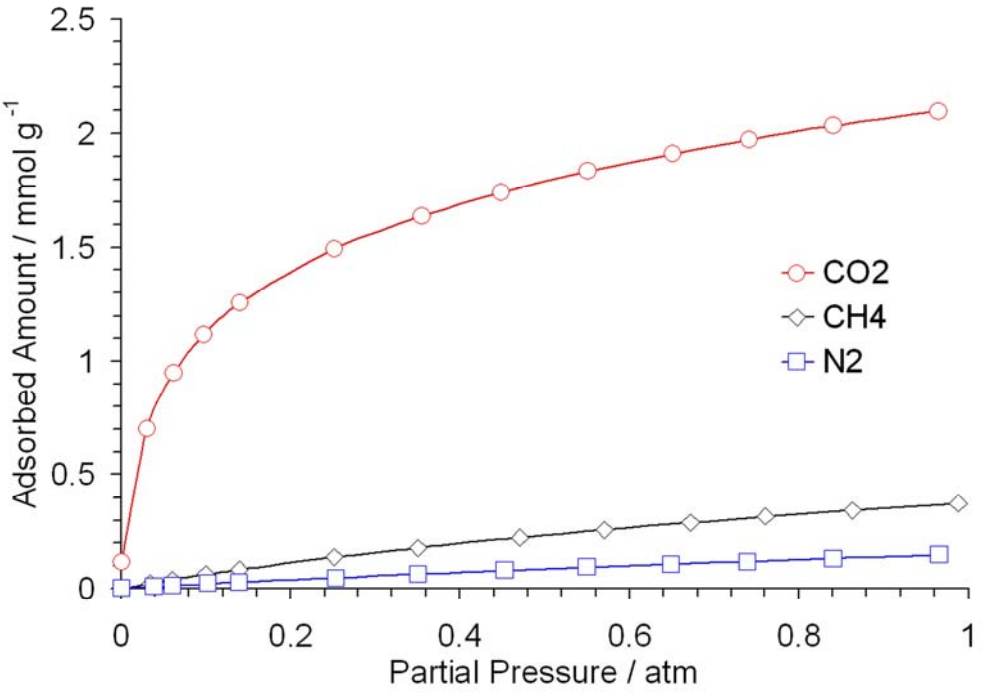

Figure H.5 Adsorption isotherms at 298 K for CO_2, CH_4, and N_2 on Sr-UPRM-4h pre-treated at 363 K.